Study of SAPS-like flows with the King Salmon SuperDARN radar

A Thesis Submitted to the

College of Graduate Studies and Research

in Partial Fulfillment of the Requirements

for the degree of Master of Science

in the Department of Physics and Engineering Physics

University of Saskatchewan

Saskatoon

By

Robyn Drayton

Permission to Use

In presenting this thesis in partial fulfilment of the requirements for a Post-graduate degree from the University of Saskatchewan, I agree that the Libraries of this University may make it freely available for inspection. I further agree that permission for copying of this thesis in any manner, in whole or in part, for scholarly purposes may be granted by the professor or professors who supervised my thesis work or, in their absence, by the Head of the Department or the Dean of the College in which my thesis work was done. It is understood that any copying or publication or use of this thesis or parts thereof for financial gain shall not be allowed without my written permission. It is also understood that due recognition shall be given to me and to the University of Saskatchewan in any scholarly use which may be made of any material in my thesis.

Requests for permission to copy or to make other use of material in this thesis in whole or part should be addressed to:

Head of the Department of Physics and Engineering Physics
Physics Building
116 Science Place
University of Saskatchewan
Saskatoon, Saskatchewan
Canada
S7N 5E2

Abstract

This thesis has two focuses. The major focus is an investigation of the nature of high-velocity (∼2 km/s) ionospheric flows occasionally detected by the King Salmon SuperDARN radar at relatively low magnetic latitudes of 65^0. The second focus is a validation work on the quality of SuperDARN convection measurements. As an alternative convection-monitoring instrument, an ion drift meter onboard the DMSP satellite was chosen for comparison with SuperDARN. This study includes a broad range of velocities of up to ∼1.5 km/s. Consideration of very large velocities is fundamentally important for successful research on the major topic of the thesis.

The validation work is performed first. Two approaches are undertaken. The first approach considers data at the raw level. SuperDARN F region line-of-sight velocities are directly compared with DMSP cross-track ion drifts in approximately the same directions. More than 200 satellite passes over the fields of view of five Northern Hemisphere and four Southern Hemisphere radars are considered. It is shown that all radars exhibit overall consistency with DMSP measurements and a linear fit line to the data has a slope of 0.8 with a tendency for SuperDARN velocities to be smaller. Radar echo range effects and the role of spatial inhomogeneity and temporal variations of the convection pattern are investigated. SuperDARN convection maps were generated for select events for which SuperDARN l-o-s data agree almost ideally with DMSP measurements. Convection maps were obtained using all Northern Hemisphere SuperDARN radars. The full convection vectors were found to be in reasonable agreement with the DMSP ion drifts, although a small deterioration (∼10%) was noticed. The overall agreement between SuperDARN and DMSP measurements implies SuperDARN observations are reliable for velocity magnitudes of up to ∼1.5 km/s, and SuperDARN radars are suitable instruments for studying extremely fast ionospheric flows. These results also imply that radar measurements

can be merged with DMSP measurements into a common data set to provide more reliable convection maps.

For the main focus of the thesis, a statistical investigation of the King Salmon radar echoes was performed to determine typical echo characteristics and compare them with data from other SuperDARN radars. It is shown that King Salmon regularly observes high-velocity echoes in the dusk sector at ∼21:00 MLT and $\sim 65^0$ MLat. Individual events are presented with line-of-sight velocities (observed with the L-shell aligned beams) as high as 2 km/s. Statistically, the enhanced flows are the largest and cover the greatest area in the winter and are the smallest and cover the least area in the summer. Similar fast flows were discovered in the Unwin radar data (in the Southern Hemisphere, lowest magnetic latitude $\sim 57^0$) that became available near the completion time of this thesis. It is also shown that statistically, the Stokkseyri radar, which observes in the auroral zone and has a similar azimuthal orientation as King Salmon, does not observe similar high-velocity echoes. Geophysical conditions for the onset of high-velocity King Salmon flows in several individual events are then investigated. It is shown that fast flows are excited in close association with substorm progression near the King Salmon field of view. By comparing SuperDARN data with optical images obtained from the IMAGE satellite and particle data from the DMSP satellites it is shown that velocity enhancement begins at substorm onset and peaks 20-50 minutes later over a range of latitudes including the auroral and sub-auroral regions. During the substorm recovery phase, as bright aurora shifts poleward, exceptionally fast flows can be excited at the equatorial edge of the electron auroral oval and these flows can be classified as sub-auroral polarization stream (SAPS) flows. Variability of SAPS flows and their relationship to auroral oval processes are discussed. Finally, several suggestions for further research are presented.

Acknowledgements

I would like to thank my supervisor Dr. Sasha Koustov for his guidance and support throughout my graduate career. He is an excellent and dedicated teacher and has made my studies both rewarding and enjoyable.

I am very grateful for the abundance of help I received from members of the SuperDARN group at the University of Saskatchewan. Thank you to Dr. G.J. Sofko and Dr. J.-P. St.-Maurice for your helpful instruction. Thank you to D. André, J.D. Gorin, Dr. K.A. McWilliams, and E. Kulyk for the use of various programs, and for your programming advice. Thank you to my fellow graduate students, R.D. Schwab, R.G. Gillies, D.M. Gillies, L. Benkevitch, and J. Pfeifer for your constant support.

I would also like to acknowledge the groups who provided the data for my research. Thank you to all the national funding agencies which make possible the funding of the SuperDARN radars. Thanks to the Center for Space Sciences at the University of Texas at Dallas and the US Air Force for providing the DMSP data. Thank you to the people and institutions responsible for providing the LANL, ACE, IMAGE FUV, and magnetometer data used in this thesis.

Finally I would like to thank my parents, my sisters, my fiancé Patrick, and of course Webster for their love, support and understanding.

Contents

List of Tables

List of Figures

List of Abbreviations

ACE	Advanced Composition Explorer
ACF	Autocorrelation Function
AWFC	Auroral Westward Flow Channel
CANOPUS	Canadian Auroral Network for the Open Program Unified Study
CARISMA	Canadian Array for Realtime Investigations of Magnetic Activity
DNL	Distant Neutral Line
DMSP	Defense Meteorological Satellite Program
EISCAT	European Incoherent Scatter
FUV	Far Ultraviolet Imaging
GIMA	Geophysical Institude Magnetometer Array
HF	High Frequency
IDM	Ion Drift Meter
IGRF	International Geomagnetic Reference Field
IMAGE	Imager for Magnetopause-to-Aurora Global Exploration
IMF	Interplanetary Magnetic Field
ISR	Incoherent Scatter Radar
LANL	Los-Alamos National Laboratory
l-o-s	Line-of-Sight
MLat	Magnetic Latitude
MLT	Magnetic Local Time
MQI	Macquarie Island
NENL	Near Earth Neutral Line
R1	Region 1
R2	Region 2
R_E	Earth Radius
RPA	Retarding Potential Analyzer
SAEF	Sub-Auroral Electric Field
SAID	Sub-Auroral Ion Drift
SAPS	Sub-Auroral Polarization Stream
SOPA	Synchronous Orbit Particle Analyzer
SSIES	Sensors-Ions, Electron, and Scintillation
STARE	Scandinavian Twin Auroral Radar Experiment
SuperDARN	Super Dual Auroral Radar Network
SWEPAM	Solar Wind Electron, Proton Alpha Monitor
TIGER	Tasman International Geospace Environment Radar
UHF	Ultra High Frequency
UT	Universal Time
VHF	Very High Frequency
WIC	Wideband Imaging Camera

Chapter 1

Introduction

Interaction between the solar wind and the ionized portion of the Earth environment forms a highly dynamic region surrounding the Earth called the magnetosphere. The magnetosphere is filled with various populations of charged particles, or simply plasma, whose motion is strongly controlled by a magnetic field. Under certain conditions, magnetospheric particles penetrate into the Earth's upper atmosphere, exciting neutral atoms and creating awesome displays of light called the aurora borealis and auroral australis in the high-latitude regions of the Northern and Southern Hemispheres, respectively.

Charged particles penetrating from the magnetosphere into the Earth's neutral atmosphere cause the ionization of neutral particles. Another, and more significant, source of charged particles is photoionization by Sunlight. As a result, at altitudes above ∼80 km the upper atmosphere has a significant amount of free electrons and ions. This part of the near Earth space is known as the ionosphere. The ionosphere is electrically connected to the magnetosphere by highly conducting magnetic field lines. Coupling between the magnetosphere and ionosphere allows space physicists to monitor the magnetosphere by observing phenomena in the ionosphere. In particular, studying plasma flows in the ionosphere greatly improves the general knowledge of magnetospheric dynamics. Plasma circulation in the magnetosphere is key to the understanding of the solar wind interaction with the Earth.

The processes in the near Earth space have been discussed in detail in numerous book and articles. In the following sections we provide a short description of the solar wind, magnetosphere, and ionosphere following the works by *Hargreaves* (1992), *Kivelson and Russell* (1995), and *Baumjohann and Treumann* (1997).

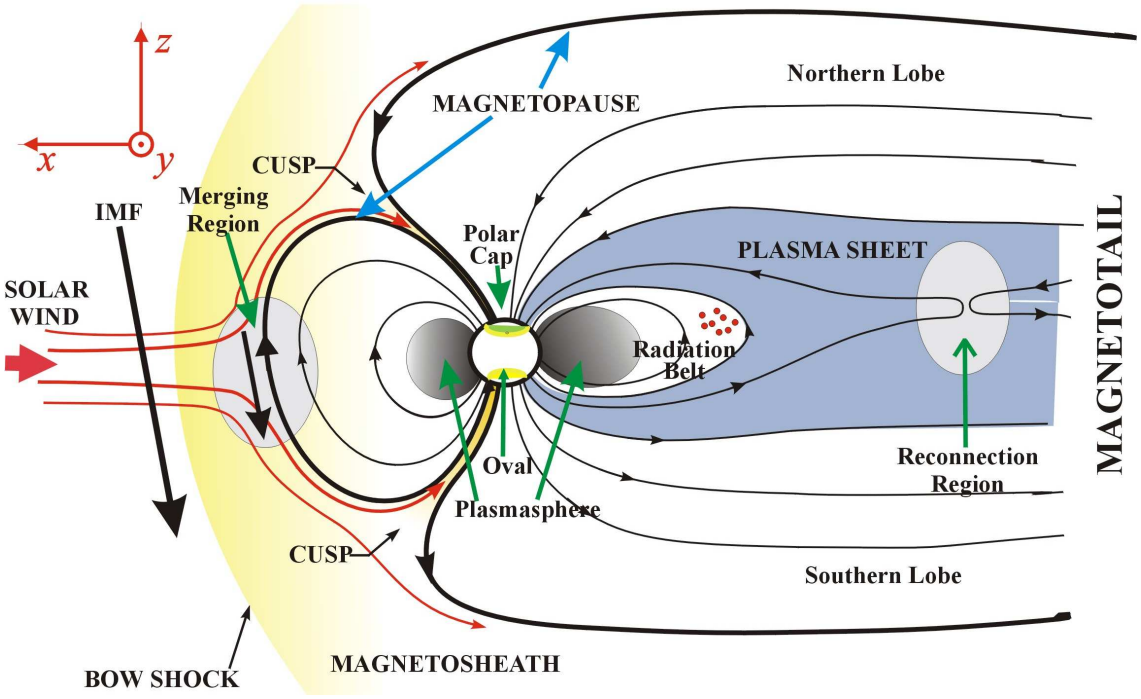

Figure 1.1: Magnetospheric cross-section in the north-south plane with the solar-magnetospheric coordinate system overplotted (adapted from original drawing by K. McWilliams).

1.1 Solar wind and magnetosphere

The Sun continuously ejects a stream of highly conducting plasma known as the solar wind. As the solar wind drifts radially outward from the Sun, the solar magnetic field (B) lines associated with the plasma are dragged along, creating the interplanetary magnetic field (IMF). Typical IMF values are 1-10 nT and solar wind particle density and speeds are $\sim$5 cm^{-3} and 200-800 km/s, respectively. It is customary to use the solar-magnetospheric coordinate system to describe the IMF; for this system, the x axis points toward the Sun, the z axis is parallel to the Earth's magnetic dipole, and the y axis complements the $x-y$ axis to complete a right-handed coordinate system.

Figure 1.1 schematically depicts the magnetosphere and surrounding environment for IMF $B_z < 0$. The Earth's dipole-like magnetic field is distorted by the solar wind. The front-side magnetosphere has a rounded shape and extends to about 10

Earth radii (R_E) on the dayside, whereas the magnetotail is elongated and extends to 50-100 R_E on the night-side. Both the front-side magnetosphere and the magnetotail are roughly aligned along the Earth-Sun line. As the supersonic solar wind drifts toward the Earth, the magnetosphere blocks its path and a shock wave, or bow shock, is established 2-3 R_E sunward of the outer region of the magnetosphere, called the magnetopause. The solar wind is slowed down to subsonic speeds by dissipating the kinetic energy of its particles at the bow shock. The solar wind then enters the magnetosheath, which is the region between the bow shock and the magnetopause. Magnetosheath plasma moves around the magnetosphere and does not easily penetrate the magnetopause. When solar wind particles encounter the magnetic field of the front-side magnetosphere, electrons are shifted dawnward and ions are shifted duskward along the magnetopause. The relative motion of charged particles generates the magnetopause current.

1.1.1 Plasma circulation in the magnetosphere

The solar wind interacts with the magnetosphere by two different processes as illustrated by Figure 1.2. One process is quasi-viscous interaction, Figure 1.2a, and the other is merging and reconnection, Figure 1.2b. For quasi-viscous interaction, solar wind flows around the egg-shaped magnetosphere dragging along the IMF. Energy and momentum are transferred from the solar wind to the outer magnetosphere causing anti-sunward flow in the boundary layer of the enclosed plasma. Because the system is closed, the flow reverses in the magnetotail causing plasma to move toward and around the inner magnetosphere. Sunward motion is transferred to the outer edges of the inner magnetosphere. The flow reverses in the front-side magnetosphere, causing anti-sunward flow over the polar cap. As a result, a two-cell circulation pattern is established in the ionosphere over both the Northern and Southern Earth hemispheres.

For merging and reconnection, a southward ($B_z < 0$) oriented IMF approaches the northward ($B_z > 0$) oriented field lines in the Earth's magnetic field. When the anti-parallel lines meet, the net field goes to zero and the lines interconnect or merge

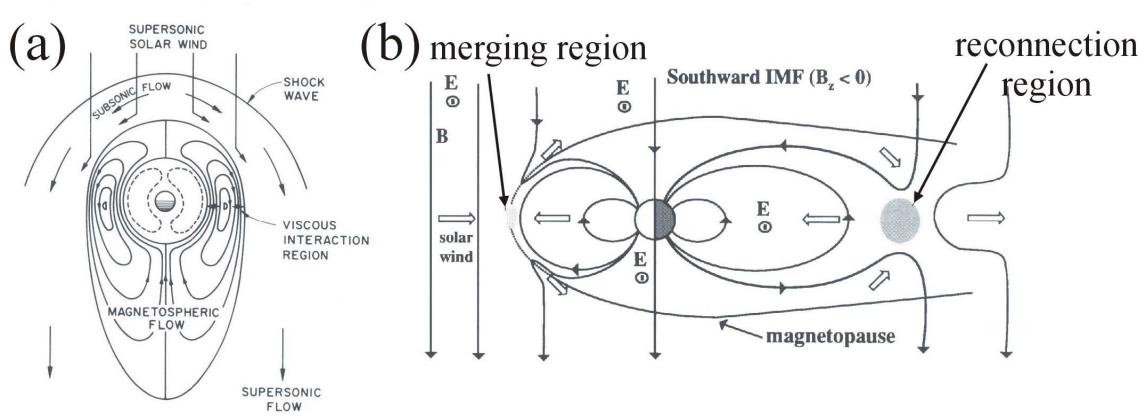

Figure 1.2: Solar wind-magnetosphere interaction processes: (a) quasi-viscous interaction (*Kelley*, 1989) and (b) reconnection. Shaded regions indicate where merging (frontside) and reconnection (magnetotail) takes place (*Cravens*, 1997).

to form "open" field lines with one end in the solar wind and the other in the Earth. The newly formed open field lines are carried by the solar wind into the magnetotail. Here the lines reconnect into their original configuration consisting of a closed field line attached to the Earth and a separate IMF line traveling away from the Earth. After reconnection, dipolarization of the stretched field lines causes particles in the outer magnetotail to be accelerated Earthward.

1.1.2 Other magnetospheric regions

The outer magnetosphere is traditionally divided into different regions based on average plasma density and particle energy (Figure 1.1). The outermost region of the magnetotail, called the plasma mantle (not shown), is populated by particles with energies of 30-150 eV and has a density of 0.1-10 cm^{-3}. The mantle surrounds the sparsely populated (<0.1 cm^{-3}) tail lobes. Both the plasma mantle and tail lobes lie on open field lines as shown.

The magnetotail is separated into Northern and Southern regions by the plasma sheet boundary layer, which surrounds the plasma sheet. The plasma sheet is centered near the equatorial plane with its inner edge at approximately 7 R_E at midnight. Particle density in the plasma sheet is about .1-1 cm^{-3}, and it is comprised mostly of H^+ ions and electrons. Typical particle energies lie between 0.1 keV and

10 keV. The plasma sheet has a thickness of 1-5 R_E and extends between dawn and dusk. Periods of increased convection cause inward motion of the plasma sheet toward the Earth. A current, called the neutral sheet current, flows from dawn-to-dusk through the plasma sheet in the equatorial plane across the magnetotail.

1.1.3 Radiation belts and the ring current

As energetic particles move toward the Earth from the plasma sheet, they enter a region where their motion is subject to electric and magnetic fields and to the density gradients of the background plasma. As a result, some particles become trapped in magnetic field-aligned regions called radiation belts extending from ∼1000 km above the Earth's surface to a distance of ∼6 R_E. Within the radiation belts, curvature-gradient drift (Section 1.3.2) causes ions to move westward toward dusk and electrons to move eastward toward dawn. The relative motion of charged particles forms a westward flowing ring current at a radial distance of 4-6 R_E. Ring current particles are of high energy (keV-MeV). During periods of intense magnetic activity or storms, the ring current intensifies due to an increase of injected particles thereby causing a depression in the Earth's magnetic field, which can be detected by ground based magnetometers located near the equator.

1.1.4 Plasmasphere

The plasmasphere contains a cold (1 eV), dense (10^3 cm^{-3}) particle population which extends out to ∼4 R_E. Within the plasmasphere, the magnetic field can be approximated as a dipole field, and plasma roughly co-rotates with the Earth. The outer boundary of the plasmasphere, the plasmapause, is typically located between 3 and 5 R_E. This location depends on the relative strengths of plasma co-rotating with the Earth and of plasma convecting Earthward from the magnetotail. During periods of high magnetic activity the convection contribution to particle motion increases and the plasmapause boundary moves Earthward. This forces particles

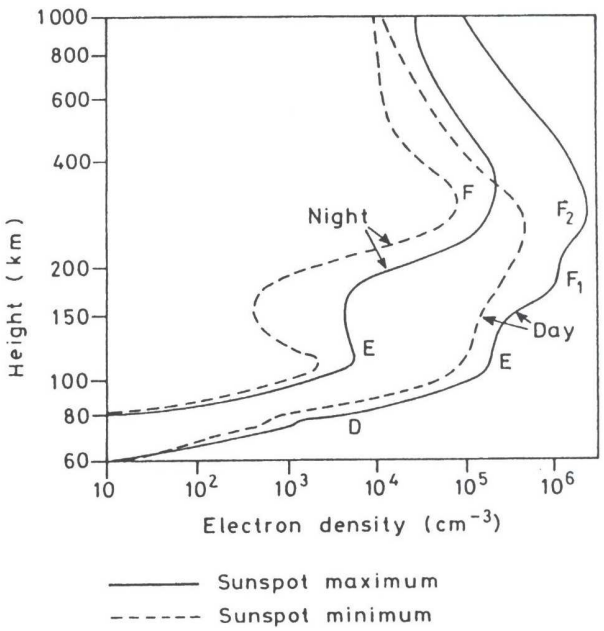

Figure 1.3: Ionospheric electron density profiles at mid-latitudes for day and night at sunspot maximum and minimum (*Hargreaves*, 1992).

previously located in the plasmasphere to be stripped away and move sunward with the convection plasma.

1.2 Ionosphere

In the ionosphere, charged particles are organized into distinct layers based on the vertical electron density profile, Figure 1.3. The D region is the lowest and peaks at an altitude of ∼90 km, with an electron density of $\sim 10^4\ cm^{-3}$. The E region peaks at ∼130 km and has an electron density peak of $\sim 10^5\ cm^{-3}$. At approximately 250 km, the F region peaks with an electron density of $\sim 10^6\ cm^{-3}$. During the day the F region peaks at ∼170 km (F1 region) and ∼300 km (F2 region).

The E region is formed by a balance of photoionization and recombination reactions. Photoionization of N_2, which is abundant at E region altitudes, leads to an accumulation of NO^+ through an interchange reaction involving O. At night, a lack of photons significantly reduces ion production, and the E region disappears as ions are removed through recombination reactions. At F-region altitudes, O dominates

over N_2. Photoionization reactions will therefore cause a build up of O^+, forming another distinct layer. Although ion densities also decrease at night, the F region does not disappear like the E region.

Plasma in the F region is strongly controlled by electric ($\mathbf{E}$) and magnetic ($\mathbf{B}$) fields. To illustrate this, consider the general equation of motion for ions and electrons (*Kelley*, 1989)

$$m_\alpha \frac{d\mathbf{v}_\alpha}{dt} = q_\alpha \left[\mathbf{E} + \mathbf{v}_\alpha \times \mathbf{B}\right] - m_\alpha \nu_{\alpha n} \left(\mathbf{v}_\alpha - \mathbf{U}_n\right) \pm m_e \nu_{ei} \left(\mathbf{v}_e - \mathbf{v}_i\right) - \frac{\nabla \left(n_\alpha T_\alpha\right)}{n_\alpha}, \quad (1.1)$$

where α=i,e represents either ions or electrons, m_α is the particle mass, $\mathbf{v}_\alpha$ is the fluid velocity, q_α is the charge, $\nu_{\alpha n}$ is the collision frequency with neutrals, ν_{ei} is the electron-ion collision frequency, $\mathbf{U}_n$ is the neutral wind velocity, T_α is the temperature (in units of energy), and n_α is the particle density. In the third term on the right hand side, the positive sign applies to ions and the negative sign applies to electrons. If one considers the cold approximation (T_α=0 eV) for the bottom of the F region ($\nu_{\alpha n} \gg \nu_{ei}$) and neglects the effects of the neutral wind ($\mathbf{U}_n$=0 m/s), equation (1.1) becomes:

$$m_\alpha \frac{d\mathbf{v}_\alpha}{dt} = q_\alpha \left[\mathbf{E} + \mathbf{v}_\alpha \times \mathbf{B}\right] - m_\alpha \nu_{\alpha n} \mathbf{v}_\alpha. \quad (1.2)$$

For stationary conditions ($\frac{d}{dt} = 0$), the fluid velocity $\mathbf{v}_\alpha$ is given by

$$\mathbf{v}_\alpha = \frac{\Omega_\alpha^2}{\Omega_\alpha^2 + \nu_{\alpha n}^2} \mathrm{v}_E \frac{\mathbf{E}_\perp \times \mathbf{B}}{|\,\mathbf{E}_\perp \times \mathbf{B}\,|} + \frac{\Omega_\alpha \nu_{\alpha n}}{\Omega_\alpha^2 + \nu_{\alpha n}^2} \mathrm{v}_E \frac{\mathbf{E}_\perp}{|\,\mathbf{E}_\perp\,|} + \frac{\Omega_\alpha}{\nu_{\alpha n}} \frac{E_{||}}{B} \frac{\mathbf{E}_{||}}{|\,\mathbf{E}_{||}\,|}, \quad (1.3)$$

where Ω_α is the particle gyrofrequency defined by $\Omega_\alpha = \frac{q_\alpha B}{m_\alpha}$. In the F region, electron and ion gyrofrequencies are of the order of 10^7 and 10^2 s^{-1}, respectively. In equation (1.3), the electric field can have components perpendicular ($\mathbf{E}_\perp$) and parallel ($\mathbf{E}_{||}$) to the magnetic field. Speed v_E is the magnitude of the drift experienced by the particles of a collisionless plasma in the presence of constant, crossed electric and magnetic fields. It is defined as

$$\mathbf{v}_E = \frac{\mathbf{E}_\perp \times \mathbf{B}}{B^2}, \quad \text{where} \quad \mathrm{v}_E = \frac{E_\perp}{B}. \quad (1.4)$$

Note that v_E is independent of charge. In the F region $\nu_{\alpha n} \ll \Omega_\alpha$ and equation (1.3) can be reduced to

$$\mathbf{v}_\alpha = v_E \frac{\mathbf{E}_\perp \times \mathbf{B}}{|\,\mathbf{E}_\perp \times \mathbf{B}\,|} + \frac{\nu_{\alpha n}}{\Omega_\alpha} v_E \frac{\mathbf{E}_\perp}{|\,\mathbf{E}_\perp\,|} + \frac{\Omega_\alpha}{\nu_{\alpha n}} \frac{E_{||}}{B} \frac{\mathbf{E}_{||}}{|\,\mathbf{E}_{||}\,|}. \quad (1.5)$$

According to the first term, F region ions and electrons move in the same direction, or convect in the $\mathbf{E}\times\mathbf{B}$ direction. This motion is faster than particle motion along the electric field. In contrast, ions and electrons move in opposite directions along the electric and magnetic fields. There is a relative velocity between ions and electrons along the electric field and along the magnetic field; ions move faster than electrons along the electric field, and electrons move faster than ions along the magnetic field.

1.2.1 Ohm's law for ionospheric plasma

The relative drift between ions and electrons in the ionosphere results in the flow of current having a current density of

$$\mathbf{j} = en\mathbf{v}_d, \tag{1.6}$$

where $\mathbf{v}_d = \mathbf{v}_i - \mathbf{v}_e$ is the relative drift between ions and electrons, $n = n_e = n_i$ is the electron and ion particle density, and $\mathbf{j}$ has units of A/m^2. The current density can be represented by components using equation (1.3) and then written in a simplified form known as Ohm's law

$$\mathbf{j} = \bar{\bar{\sigma}} \cdot \mathbf{E}, \tag{1.7}$$

where $\bar{\bar{\sigma}}$ is the 3×3 conductivity tensor given by

$$\bar{\bar{\sigma}} = \begin{pmatrix} \sigma_P & \sigma_H & 0 \\ -\sigma_H & \sigma_P & 0 \\ 0 & 0 & \sigma_{||} \end{pmatrix}, \quad \text{where} \tag{1.8}$$

$$\sigma_P = \frac{en}{B}\left(\frac{\mid \Omega_i \mid \nu_{in}}{\Omega_i^2 + \nu_{in}^2} + \frac{\mid \Omega_e \mid \nu_{en}}{\Omega_e^2 + \nu_{en}^2}\right), \tag{1.9}$$

$$\sigma_H = \frac{en}{B}\left(\frac{-\Omega_i^2}{\Omega_i^2 + \nu_{in}^2} + \frac{\Omega_e^2}{\Omega_e^2 + \nu_{en}^2}\right), \quad \text{and} \tag{1.10}$$

$$\sigma_{||} = e^2 n\left(\frac{1}{m_i \nu_{in}} + \frac{1}{m_e \nu_{en}}\right). \tag{1.11}$$

The various components of the conductivity tensor describe currents in the ionosphere. The Pedersen (σ_P) and Hall (σ_H) conductivities describe the currents in

the $\mathbf{E}_\perp$ and $\mathbf{E}_\perp \times \mathbf{B}$ directions, respectively, whereas the parallel conductivity ($\sigma_{||}$) describes the current along the magnetic field.

It should be noted that equation (1.7) is only appicable for the bottom of the F region where $\nu_{\alpha n} \gg \nu_{ei}$. The conductivity tensor components given by equations (1.9)-(1.11) are more complicated for the more general case (*Liang*, 2004). It is generally accepted that contributions from additional terms in the high altitude F region are not significant, and equations (1.9)-(1.11) are widely used.

In the high latitude ionosphere ($> 60^0$ magnetic latitude) the magnetic field lines are almost vertical and $\mathbf{E}_\perp$ is height independent (to a first approximation). One can introduce the height-integrated Pedersen and Hall conductances

$$\Sigma_P = \int \sigma_P dz, \quad \text{and} \tag{1.12}$$

$$\Sigma_H = \int \sigma_H dz \tag{1.13}$$

to represent the two dimensional horizontal sheet of current perpendicular to the magnet field in the form

$$\mathbf{J}_\perp = \int \mathbf{j}_\perp dz = \bar{\bar{\Sigma}} \cdot \mathbf{E}_\perp, \tag{1.14}$$

where $\bar{\bar{\Sigma}}$ is the 2×2 conductance tensor given by

$$\bar{\bar{\Sigma}} = \begin{pmatrix} \Sigma_P & \Sigma_H \\ -\Sigma_H & \Sigma_P \end{pmatrix}. \tag{1.15}$$

Equation (1.14) may also be written as

$$\mathbf{J}_\perp = \Sigma_P \mathbf{E}_\perp - \Sigma_H \frac{(\mathbf{E}_\perp \times \mathbf{B})}{B}. \tag{1.16}$$

1.2.2 Ionospheric convection pattern

The global pattern of plasma convection in the ionosphere is consistent with plasma motion in the near Earth environment. For a southward IMF, as newly reconnected magnetic flux lines travel anti-sunward across the polar cap, the electric field $\mathbf{E}_{pc}$ points from dawn-to-dusk over the polar cap. Because magnetic flux lines are equipotential to a first approximation, $\mathbf{E}_{pc}$ is mapped down to the polar

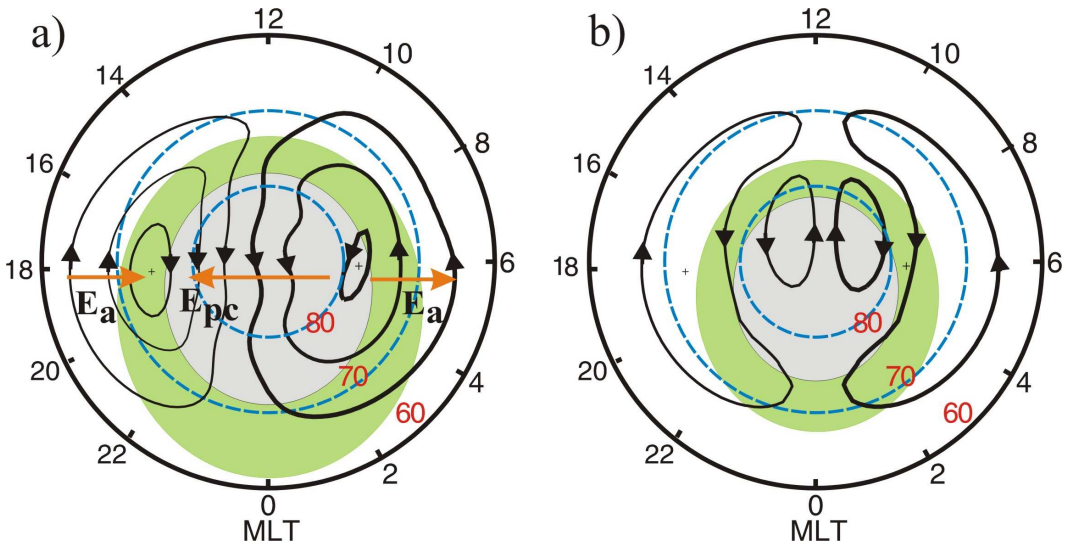

Figure 1.4: (a)Ionospheric electric fields and typical two-cell convection pattern for the high latitude ionosphere for a southward IMF and B_y=0. (b)Four-cell convection pattern for a strongly northward IMF and B_y=0. The green and grey shading in both diagrams indicate the auroral oval and polar cap, respectively.

ionosphere, causing anti-sunward plasma flow in the central polar cap. In the tail, as plasma flows sunward toward and around the Earth (after tail reconnection), the corresponding electric fields, $\mathbf{E}_a$, in the magnetosphere are mapped to lower latitudes, $\sim 65^0$ magnetic latitude (MLat), and drive plasma back toward the Sun. Electric fields $\mathbf{E}_a$ and $\mathbf{E}_{pc}$ create a two-cell convection pattern for southward IMF, Figure 1.4a. When the IMF B_y component is small (close to 0), the convection cells are symmetric with respect to the noon-midnight magnetic meridian. Variations in B_y alter the symmetry of this pattern; if B_y is positive, the dusk cell dominates, and for B_y negative, the morning cell dominates. We should note that quasi-viscous interaction, which is important when the IMF is around zero, also produces a two-cell pattern that adds to the reconnection-driven pattern. The convection pattern has two cells about 75% of the time (*Heppner*, 1977; *Ruohoniemi and Greenwald*, 1996).

When the IMF is oriented northward ($B_z > 0$), there is no chance for it to couple with the geomagnetic field in the front-side magnetosphere. However, as the flux lines travel around and over the magnetopause, they encounter southward oriented field lines in the magnetospheric lobes causing reconnection there. The corresponding pattern of convection consists of several cells (*Reiff and Burch*, 1985). Figure

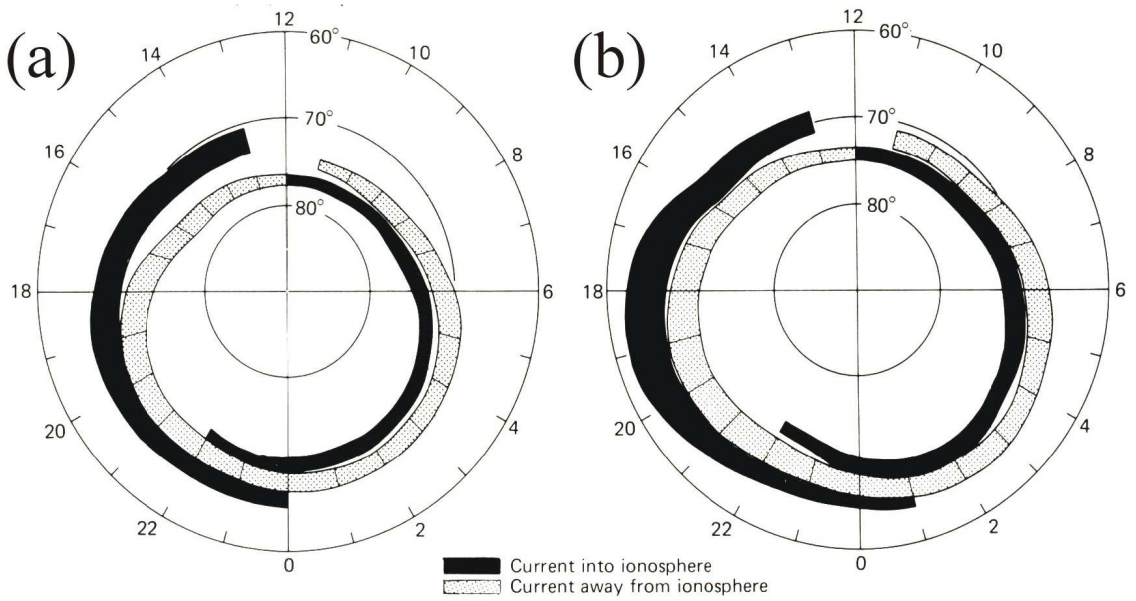

Figure 1.5: Distribution of field aligned currents for (a) quiet and (b) active magnetic periods (*Iijima and Potemra*, 1978).

1.4b indicates a four-cell convection pattern hypothesized for a strongly northward B_z and B_y=0. When B_y is positive, the inner morning cell dominates and when B_y is negative the inner dusk cell dominates. When B_z is only weakly dominant, the inner cells merge into one large cell with westward flowing plasma for a positive B_y and eastward flowing plasma for a negative B_y.

1.2.3 Field-aligned currents

Coupling between the magnetosphere and the ionosphere is achieved by the flow of field-aligned currents (FACs) along magnetic field lines. Such flows were first detected by studying variations in the east-west component of the Earth's magnetic field from a spacecraft at high latitudes. Figure 1.5a illustrates the distribution of the currents in the Northern Hemisphere. Typical FAC current densities are a few $\mu A/m^2$. The inner region of current is called the region 1 (R1) FAC; R1 currents flow into the ionosphere on the dawnside and out of the ionosphere on the duskside. In contrast, the currents in the outer region, region 2 (R2) FACs, flow into the ionosphere on the duskside and out of the ionosphere on the dawnside. There is

an additional FAC near the Harang discontinuity where the currents overlap on the nightside and near the cusp.

The R1 current system is located near the poleward edge of the auroral oval. In fact, the entire current system has close ties with the auroral oval as it expands and moves equatorward on the nightside during periods of high magnetic activity, Figure 1.5b.

1.3 Particle motion in the radiation belts

It is clear that the distribution of electric fields and FACs at high latitudes is controlled by the interaction between the solar wind IMF and the electric and magnetic fields in the near Earth space. However, recent observations indicate the electric field distribution at sub-auroral latitudes can be significantly affected by the redistribution of particles within the magnetosphere. In this section we review the basics of particle motion in the radiation belts and plasmasphere as these regions affect the electric field distribution.

1.3.1 Particle gyration and bounce motion due to a magnetic field

Particles trapped in the radiation belts gyrate about magnetic field lines as shown in Figure 1.6. The gyrofrequency and gyroradius of the circular motion are given by

$$\Omega_\alpha = \frac{q_\alpha B}{m_\alpha}, \quad \text{and} \tag{1.17}$$

$$r_\alpha = \frac{m_\alpha v_\perp}{\mid q_\alpha \mid B}, \tag{1.18}$$

where α represents either ions or electrons, and $v_\perp$ is the component of the particle's velocity perpendicular to the magnetic field line. Gyrofrequency is dependent on charge, and electrons and ions orbit in opposite directions. For particles with $W_\perp$=1 keV, typical magnitudes of gyroradii, gyrofrequency, and gyroperiod for B=140 nT

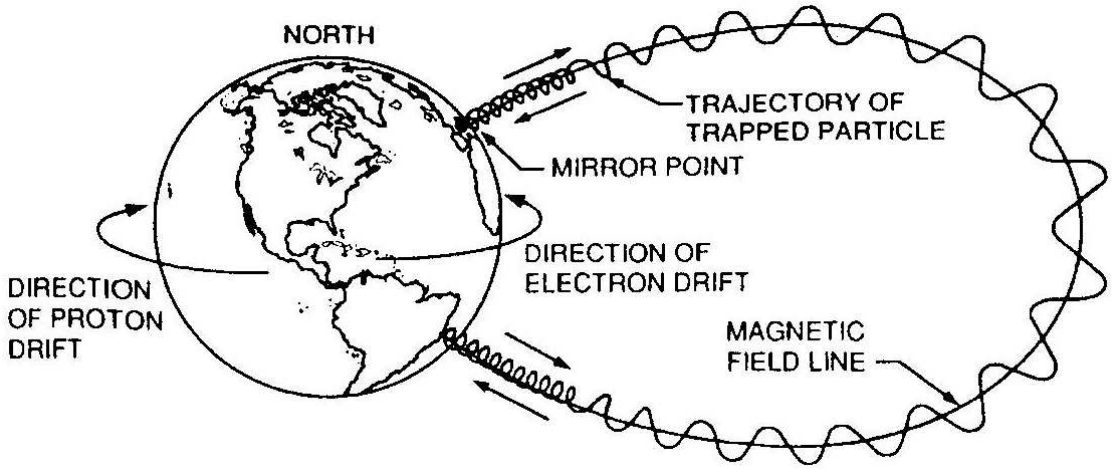

Figure 1.6: Motion of trapped particles gyrating and bouncing along closed field lines and experiencing curvature-gradient drift. (*Walt*, 1994)

are r_e=0.76 km, Ω_e=25 $(ks)^{-1}$, and $\tau_{g,e}$=0.25 ms for electrons and r_i=32 km, Ω_i=13.5 s^{-1}, and $\tau_{g,i}$= 470 ms for ions (*Kivelson and Russell*, 1995). Since particles are usually injected at an angle with respect to the magnetic field lines (called the pitch angle), they also move parallel to the field lines. The combination of the particle gyration and parallel motion causes the particle to move in a helical path along the magnetic field line. It is convenient to represent the pitch angle of a particle as

$$\alpha_p = \tan^{-1} \frac{v_\perp}{v_{||}}. \tag{1.19}$$

As a particle gyrates toward lower altitudes, the magnetic field lines converge, the magnetic field magnitude becomes stronger and the gradient in the magnetic field increases. This leads to an additional force acting on the particle, the mirror force, given by

$$\mathbf{F}_\nabla = -\mu \nabla B, \tag{1.20}$$

where μ represents the magnitude of the particle magnetic moment

$$\mu = IA = \frac{q_\alpha v_\perp}{2\pi r_\alpha} \pi r_\alpha^2 = \frac{m v_\perp^2}{2B} = \frac{W_\perp}{B}. \tag{1.21}$$

Here $W_\perp$ is the component of the particle kinetic energy perpendicular to the magnetic field. Since the gradient force acts parallel to the magnetic field, and $\mathbf{F}$=m$\mathbf{a}$,

Equation (1.20) can be re-written as

$$a_{||} = -\frac{W_{\perp}}{mB}\nabla B, \tag{1.22}$$

where $a_{||}$ represents the component of the particle acceleration parallel to the magnetic field lines. Therefore, as the particle travels along an increasing magnetic field gradient, the parallel velocity decreases and eventually reverses. The points of reversal are called mirror points. The field line on which a particle bounces between hemispheres is described by an L-shell, where L is the ratio of the radial distance of the field line measured at the equator to the radius of the Earth. Typical bounce periods for particles with $W_{\perp}$=1 keV at an L-shell of 6 and $\alpha_p = 30^0$ are $\tau_{b,e}$=8.4 s for electrons and $\tau_{b,i}$=360 s for protons (*Baumjohann and Treumann*, 1997). Particles can be lost to the ionosphere at the mirror points if they penetrate too deeply (∼100 km in altitude).

1.3.2 Particle drifts due to electric and magnetic fields

Particles accelerated Earthward from the magnetotail experience drifts due to curvature and gradient forces. The geomagnetic field increases as particles moving perpendicularly to the magnetic field lines approach the Earth. Therefore, particles moving toward the Earth feel a gradient force due to the magnetic field, as described by equation (1.20). In addition, curvature of the field lines causes the particles to experience a centrifugal force.

The drift due to curvature and gradient forces can be expressed as (*Baumjohann and Treumann*, 1997):

$$\mathbf{v}_{cg} = \left(\frac{v_{\perp}^2}{2} + v_{||}^2\right)\frac{\mathbf{B}\times\nabla B}{\Omega_{\alpha}B^2}. \tag{1.23}$$

The curvature-gradient drift described by equation (1.23) causes particles to drift perpendicularly to magnetic field lines and around the Earth. Protons drift westward toward dusk and electrons drift eastward toward dawn. The relative motion of charges due to curvature-gradient drift results in the ring current discussed in Section 1.1.3. Typical drift periods for particles with $W_{\perp}$=1 keV at an L-shell of 6 and

$\alpha_p = 30^0$ are to the order of τ_d=100 hours for ions and electrons (*Baumjohann and Treumann*, 1997).

Electrons and ions gyrating, bouncing and drifting around the Earth become trapped in the radiation belt regions and should obey certain laws known as adiabatic invariants.

1.3.3 Adiabatic invariants

Adiabatic invariants describe constants of motion associated with trapped radiation belt particles slowly varying magnetic and electric fields. The first adiabatic invariant is associated with particle gyration. It states that if the magnetic field does not change appreciably during a gyroperiod, then the magnetic flux enclosed by the loop formed by the path of the gyrating particle is constant. Using equation (1.18), the flux can be expressed as

$$\Phi_m = \int \mathbf{B} \cdot d\mathbf{A} = B\pi r_\alpha^2 = B\pi \frac{m_\alpha^2 v_\perp^2}{q_\alpha^2 B^2} = \frac{2\pi m_\alpha}{q_\alpha^2} \frac{KE_\perp}{B}. \tag{1.24}$$

Since Φ_m is constant, $KE_\perp$/B is constant, and the magnetic moment given by equation (1.21) is also constant. Conservation of magnetic moment can be used to determine the magnetic field where a particle will mirror. By equating the magnetic moments of a bouncing particle at a specific point along the bounce trajectory and at its mirror point, the particle pitch angle (see equation 1.19) can be described as

$$\sin^2 \alpha_p = \frac{B}{B_m}, \tag{1.25}$$

where B and B_m represent the magnetic field at the particle location and mirror point, respectively.

The second invariant (J) is with respect to the parallel momentum integrated over one oscillation of a particle moving between mirror points:

$$J = \oint m v_{||} ds, \tag{1.26}$$

where m is the mass of the particle, and $v_{||}$ is the velocity of the particle along the magnetic field line.

The third adiabatic invariant refers to the total geomagnetic flux enclosed by the azimuthal (around the Earth) precession of a bouncing particle. It states that

$$\Phi = \oint \mathbf{B} \cdot d\mathbf{A} \tag{1.27}$$

is conserved provided the drift period is less than the period of change in the magnetic and electric field (τ). Because it takes many hours for a particle to complete one full orbit around the Earth, and τ is typically lower, the third adiabatic invariant is most easily violated causing particles to radially diffuse across magnetic field lines and precipitate into the ionosphere.

It should be noted that even when the adiabatic invariants are conserved, particles can be lost from the trapping region. Specifically, particles mirroring too closely to the Earth will be lost to the atmosphere due to collisions with neutral particles. Consider a point in a bouncing particle's trajectory located in the equatorial plane where B is given by B_{eq}. Equation (1.25) can be used to determine the equatorial loss cone described by α_l, where

$$\sin^2 \alpha_l = \frac{B_{eq}}{B_m}, \tag{1.28}$$

and B_m is the magnetic field at the mirror point. Any particle having an equatorial pitch angle less than α_l will be lost to the atmosphere at its next mirror point. The equatorial loss cone is generally small and decreases for increasing L-shells. For example, a particle trapped at L=6 has $\alpha_l = 3^0$ (*Baumjohann and Treumann*, 1997). Wave-particle interactions involving a high-frequency wave may cause particles to be scattered into the loss cone where they will be lost to the atmosphere. This process is called pitch angle scattering.

In addition to pitch angle scattering and radial diffusion, particles may be lost due to charge-exchange reactions. High energy (>keV) magnetospheric ions can lose their positive charge to low energy ($\sim$0.1 eV) neutrals at ionospheric altitudes. The reaction forms a high energy neutral particle which either escapes from the magnetosphere or returns to the Earth's atmosphere, and a low energy ion that becomes a part of the plasmasphere. Particle fluxes into and out of the trapped region must balance. During periods of high magnetic activity particles flood into

the ring current and radiation belts which later recover due to the loss processes mentioned above.

1.4 Auroral oval and auroral electrojets

Particles lost from the trapping region can precipitate into the ionosphere. Energetic precipitating electrons collide with neutral particles in the atmosphere. The result is an ionization reaction in which a particle may be excited to higher energies and emit a photon as it decays to the ground state. Particles may also become excited in the collision without being ionized. A combination of these reactions cause spectacular auroral light displays visible to the naked eye. The auroral green line of atomic oxygen at 557.7 nm and an altitude of 100-200 km is a commonly observed auroral color.

The aurora is often organized into discrete forms. Notable of these are auroral arcs, which are thin band-like structures stretched in the east-west direction. Auroral arcs are most frequently located about both the Northern and Southern Hemispheres within the auroral oval. The green shading in Figure 1.4 indicates the typical location of the auroral oval around the magnetic pole for periods of southward IMF (Figure 1.4a) and northward IMF (Figure 1.4b). The oval is offset from the pole and is located more equatorward on the nightside and poleward on the dayside. The definition of the auroral oval as the most probable areas of auroral arc occurrence was introduced from the analysis of ground-based all-sky camera observations. Subsequent satellite observations confirmed the existence of oval luminosity over the Northern and Southern Hemispheres.

During disturbed magnetic periods the aurora becomes very active and the auroral oval shifts equatorward. The region poleward of the auroral oval is called the polar cap. It is widely believed that the equatorward edge of the polar cap coincides with the open/closed boundary of the magnetic field lines so that the lines within the polar cap are connected to the magnetotail lobes.

Particle precipitation enhances conductivity in the auroral oval and forms the auroral electrojet currents. Eastward and westward electrojets flow in the dusk and dawn sectors, respectively. The electrojets flow at an approximate altitude of 100 km and create significant magnetic disturbances on the ground.

1.5 Storms, D_{st} and Kp magnetic indices

Internal processes within the Sun drive continuous, often sporadic changes of the solar wind and IMF parameters. These changes cause a chain of events in the near space environment that are not well understood. Magnetic storms and substorms are the two prominent signatures of changing conditions in the near Earth space.

When solar wind particles bombard the Earth during a period of increased activity, the front-side magnetosphere becomes compressed and the magnetopause current increases. This causes an enhancement in the H-component (magnetic north-south component) of the Earth's magnetic field at equatorial latitudes over a period of a few hours. As the storm progresses, particles in the magnetotail are injected into the inner magnetosphere at an increased rate causing the ring current to increase. The magnetic field due to the ring current opposes the H-component of the Earth's magnetic field at equatorial latitudes. Therefore, there will be a depression of the Earth's magnetic field at low latitudes.

The active, or expansion, phase of a magnetic storm ends when injection and loss processes balance in the radiation belts. Since reconnection during a period of southward IMF is the prominent mechanism in particle transport during storms (*Gonzalez et al.*, 1994 and references therein), the balance between injection and loss processes usually occurs when the southward IMF weakens or becomes northward. Loss processes are enhanced in the radiation belt until the ring current magnetic field is returned to normal. This process is called the recovery phase. The growth phase typically lasts several hours during a period of prolonged northward IMF. A change in polarity of the IMF usually triggers the storm expansion phase, which lasts about a day. Storm recovery is the longest storm phase and can last several days.

Storm strength is characterized by the D_{st} index. To create the D_{st} index, hourly averages of the H-component of the Earth's magnetic field are calculated from several low-latitude ($20^0 - 30^0$ MLat) magnetometers. Quiet-time observations are subtracted to normalize the index to zero. The D_{st} index shows a gradual increase during the growth phase of a storm, followed by a steeper decrease until the end of the expansion phase when it begins a slow recovery. Weak storms have depressions of <30 nT whereas strong and severe storms are >100 nT.

To characterize global magnetic activity that includes all potential sources, as opposed to perturbations caused purely by magnetopause and ring currents, the Kp magnetic index is used. The Kp index characterizes magnetic perturbations at 13 different magnetic observatories located between 44^0 and 66^0 geographic latitude (11 in the Northern Hemisphere and 2 in the Southern Hemisphere). For each station the maximum fluctuation of the magnetic disturbance, relative to quiet diurnal and seasonal levels, is measured in eight three-hour intervals. This measurement is converted to a quasi-logarithmic scale using a data table specific to each location. The resultant Kp measurements run on a scale from 0 to 9 broken into thirds. For example, Kp=3-, 3o, and 3+ simply mean 3-$\frac{1}{3}$, 3, and 3+$\frac{1}{3}$, respectively. It is a general consensus that Kp<2-3 corresponds to quiet conditions, Kp=2-5 corresponds to moderately disturbed conditions and Kp>5 corresponds to strong magnetic activity.

1.6 Substorms

Magnetic substorms have time scales of several hours and are very localized compared to magnetic storms. Substorm evolution can be broken into similar phases as storm evolution.

1.6.1 Substorm evolution

Under quiet conditions, the average merging rate in the front-side magnetosphere equals the average reconnection rate in the magnetotail. However, it often happens that the tail reconnection rate is slightly slower than the front-side recon-

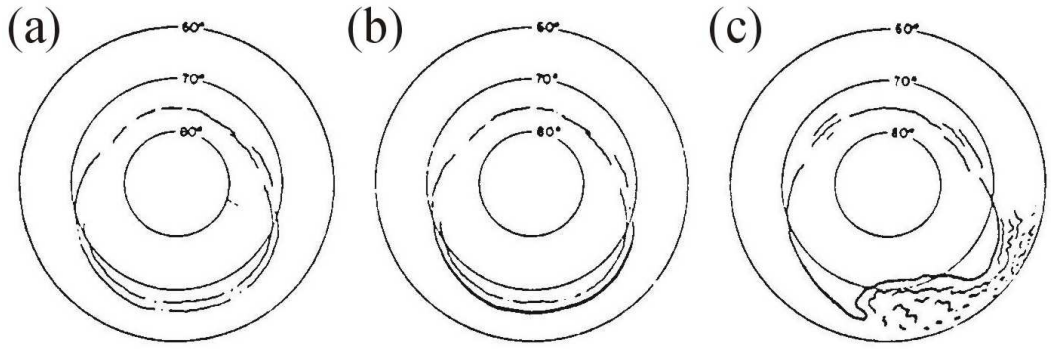

Figure 1.7: Schematic illustration of an auroral substorm (a) during the growth phase, (b) at onset, and (c) during the expansion phase (adapted from *Akasofu*, 1964).

nection rate; in this case, magnetic field lines and the plasma associated with them are added to and stored in the magnetotail, increasing the magnetic flux density and energy in the tail. As a result, the neutral sheet current increases, causing the dipole-like magnetic field lines of the tail to become stretched. This configuration is not stable; eventually, the energy stored in the tail and the stress on the magnetic field lines is suddenly released, leading to a chain of phenomena described as an auroral substorm. At substorm onset, magnetic flux lines in the tail snap back toward the Earth and return to a dipole-like configuration. When this happens, the sudden release of energy accelerates particles in the plasma sheet toward the Earth where they can precipitate into the ionosphere causing bursts of extremely bright and dynamic aurora. Substorm evolution is often broken into three phases based on characteristics of the magnetosphere and the behavior of the aurora.

(a) Growth phase

Prior to substorm onset the auroral oval is relatively inactive, Figure 1.7a. The growth phase of a substorm, Figure 1.8a, begins when an enhanced merging rate, usually due to a southward turning of the IMF B_z, causes the excessive movement of magnetic field lines and magnetospheric plasma from the front-side magnetosphere to the magnetotail. Merging processes change the location of the open/closed field line boundary, causing the polar cap area to increase. As a result, auroral arcs and the

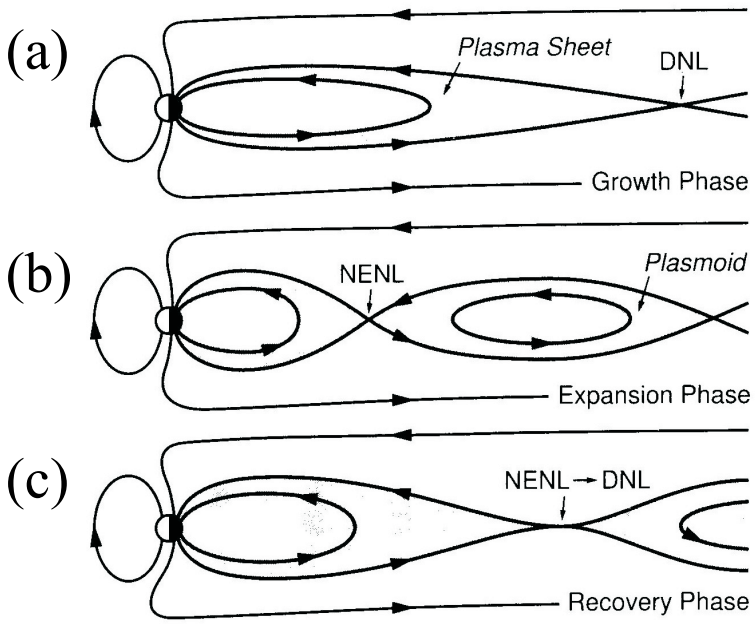

Figure 1.8: Behavior of the plasma sheet during substorm (a) growth, (b) expansion, and (c) recovery phases (*Baumjohann and Treumann*, 1997).

background oval luminosity tend to drift equatorward. After magnetotail reconnection at the distant neutral line (DNL), the magnetic field lines are transported back to the front-side magnetosphere, increasing sunward convection in the magnetotail, or are stored in the magnetotail. Growth in the magnetotail causes the magnetic field lines to stretch and the plasma sheet to thin as the neutral sheet current flowing across the magnetotail from dawn to dusk (in the equatorial plane) grows. The substorm growth phase can be identified by an increase in the H-component of magnetometers near the region where the substorm will appear at substorm onset.

(b) Onset and expansion phase

Eventually, at substorm onset, the energy stored in the magnetosphere is released. The exact mechanism responsible for triggering the substorm onset in the magnetotail is unclear. *Hsu and McPherron* (2003) found that approximately 60% of substorms are triggered by a northward turning of the IMF, a reduction in the magnitude of the B_y component of the IMF, or a sudden change in the solar wind dynamic pressure. At substorm onset the magnetotail snaps back to a more dipolar

shape, Figure 1.8b, the plasma sheet thickens, and reconnection occurs at the Near Earth Neutral Line (NENL) at about 30 R_E behind the Earth. The region of plasma between the two neutral lines, called a plasmoid, consists of closed magnetic field lines that are not attached to the Earth or the solar wind. The substorm onset can be recognized as a sudden brightening of the most equatorward auroral arc near midnight, Figure 1.7b. New arcs are formed poleward of the initial arc, and a dynamic bright bulge of auroral activity rapidly spreads both westward and poleward, Figure 1.7c. The westward motion of the auroral forms is called a westward travelling surge. The substorm expansion phase is over once the auroral activity stops its poleward expansion. Substorm onset can be identified by a sudden decrease in the magnetic field H-component of a magnetometer near the substorm bulge. The decrease maximizes at the end of the expansion phase and then begins to recover.

The substorm is also associated with the establishment of low frequency (2-25 mHz) irregular pulsations, Pi2 pulsations (*Kivelson and Russell*, 1995), on flux lines having footprints near the substorm arcs.

(c) Recovery phase

During the substorm recovery phase the magnetotail is restored to its pre-substorm configuration, Figure 1.8c. Magnetotail magnetic field lines stretch out from being dipole-like in the expansion phase, the NENL moves away from the Earth, and the plasmoid is ejected away from the Earth. The aurora visibly fades, and the magnetic field H-component of magnetometers monitoring the substorm slowly returns to pre-substorm levels. If the magnetosphere is particularly active, the recovery phase of one substorm may be interrupted by the growth and expansion phases of the next.

1.6.2 Substorm-related currents

Substorm behavior in the magnetosphere is linked to the ionosphere through field-aligned currents which drive a substorm electrojet. To describe the substorm current system at high latitudes, we must begin by discussing current and conductiv-

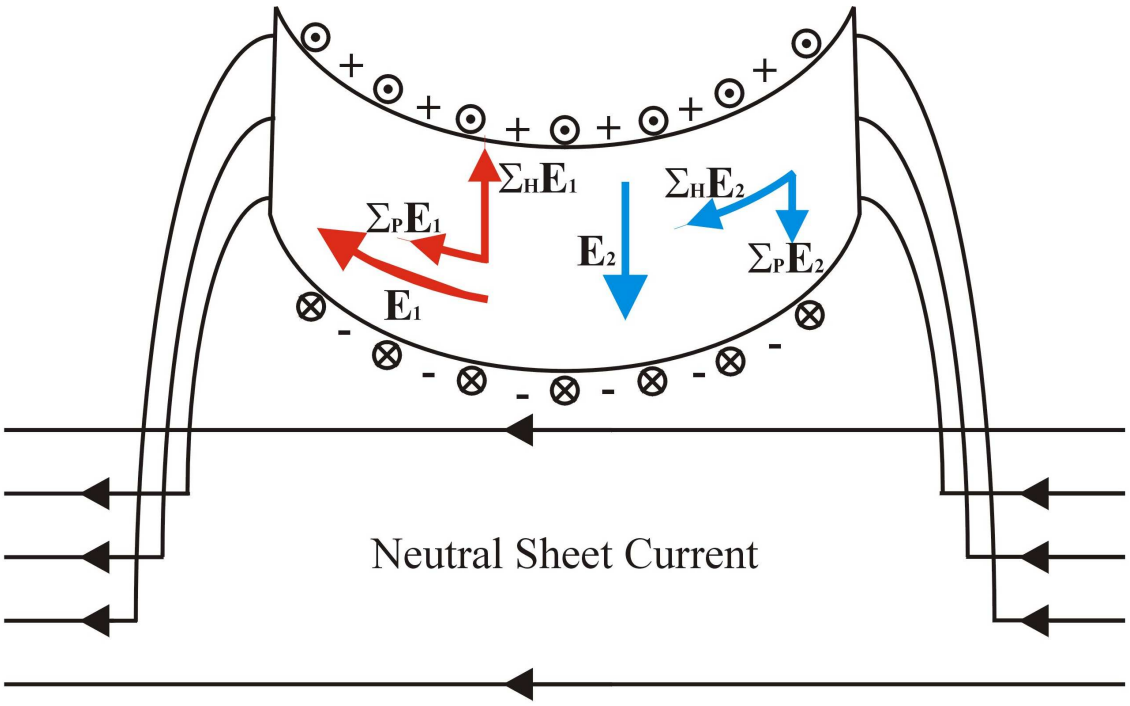

Figure 1.9: Scheme ilustrating the magnetospheric substorm current wedge and ionospheric substorm electrojet near midnight.

ity using Ohm's law as described by equation (1.16). Recall that during the growth phase of a substorm the neutral sheet current is enhanced in the magnetotail. When the NENL forms, the neutral sheet current is reduced and redirected into the highly conducting region of the ionosphere near midnight over the auroral bulge, Figure 1.9. This currents system between the magnetosphere and ionosphere is called the substorm current wedge.

Figure 1.9 illustrates the development of the substorm electrojet as discussed in *Baumjohann and Treumann* (1997). FACs are attached to the outer boundaries of the electrojet. The east and west FACs are part of the substorm current wedge. FACs on the north and south boundaries are due to the R1 and R2 currents systems for disturbed conditions (Figure 1.5b). At midnight, the electric field has a strong westward component, E_1 in Figure 1.9. According to equation (1.16), E_1 drives both westward ($\Sigma_P E_1$) and northward ($\Sigma_H E_1$) currents. FACs on the north and south boundaries close some, but not all, of the northward current. Positive and negative charges build up on the northern and southern boundaries, respectively,

driving a southward polarization electric field, E_2. This drives westward ($\Sigma_H E_2$) and southward ($\Sigma_P E_2$) currents. The southward current acts to balance the remaining northward current driven by E_1. The remaining westward currents, driven by both E_1 and E_2, form an intense westward current in the substorm electrojet given by

$$J_{westward} = \Sigma_P E_1 + \Sigma_H E_2. \tag{1.29}$$

It should be noted that despite the presence of a strong westward current, the auroral bulge will not always expand westward. *Liou and Ruohoniemi* (2006) showed that the bulge can spread eastward, and that the direction of motion is dependent on the position of the bulge with respect to the ionospheric convection pattern. During periods of strong IMF $B_y > 0$, the dusk convection cell dominates (see Section 1.2.2) and the bulge is more likely to expand westward. For periods of strong IMF $B_y < 0$, if the dominating dawnside convection flow is strong enough, the bulge will expand eastward.

1.6.3 Relationship between substorms and storms

Substorms and storms are somewhat related. At substorm onset, the sudden release of stored energy accelerates particles along the plasma sheet toward the Earth, where the particles can either be deposited into the ionosphere or trapped in the radiation belts. Because the magnetosphere is disturbed during substorms, particles are not likely to complete drift paths around the Earth and form a partial ring current system. FACs close the partial ring current across the ionosphere. If continuous particle injections occur due to multiple substorms, particles may accumulate in the radiation belts, thereby increasing the ring current and classifying the magnetic activity as a storm (*Gonzalez et al.*, 1994).

1.7 Plasma convection in the ionosphere during magnetically disturbed periods

Although it is accepted that convection in the ionosphere is directly related to conditions in the IMF and solar wind, exact details are less clear. Often, triggers in the solar wind, such as pressure pulses or changes in the IMF, lead to short-lived global-scale variations of the convection. Studying the global convection pattern in response to external drivers is an active area of research. It is of particular interest to know how plasma convection changes due to substorm-related processes.

1.7.1 General features of substorm-related convection patterns

Recent research focuses on changes in the convection pattern associated with substorm development. There are several factors limiting a complete understanding of how substorm processes affect the convection pattern. First, substorms are fast acting processes having significant variation controlled by numerous electrodynamic parameters such as FAC, conductance, intensity of magnetospheric sources, and the properties of the media through which magnetospheric electric fields are mapped into the high-latitude ionosphere. The level of variation from one substorm to the next makes observing general trends in the convection pattern difficult. Finally, and most importantly, current instrumentation is not suitable for studying the dynamical processes which occur during a substorm. Incoherent scatter radars have only recently reached a temporal resolution of 1-2 min, compared to a standard of 5 min in the past. In addition, incoherent scatter radars have a poor spatial coverage. For example, the European Incoherent Scatter (EISCAT) radar in Northern Europe only considers a small area over Tromso, compared to the global convection pattern that needs studying. Coherent scatter radars such as the Scandinavian Twin Auroral Radar Experiment (STARE) radar (*Greenwald et al.*, 1995) have better temporal and spatial resolutions, but are not suitable for global coverage either.

In this respect, the Super Dual Auroral Radar Network (SuperDARN) radars are best suited for substorm convection studies (*Greenwald et al.*, 1995). However, in practice, SuperDARN radars often have significant data gaps due to increased radio wave absorption during periods of enhanced particle precipitation.

We will briefly summarize what is known about changes of convection throughout a substorm.

(a) Growth phase

It is a generally perceived that substorms start to develop after the IMF B_z component turns southward. At this time, the intensity of the convective flows within the magnetosphere increases. These effects are documented in *Provan et al.* (2004), who showed that the commencement of the substorm growth phase coincides with an increase in the anti-sunward component of the plasma velocity flowing over the dawnside of the polar cap. *Bristow et al.* (2001, 2003) made observations regarding the direction or pattern of the convection. They showed that the classical 2-cell convection pattern for a southward IMF develops a flow shear in the midnight sector, and that the dusk cell extends into the morning sector, forming the Harang Discontinuity. The strongest shears are observed near substorm onset and they disappear after onset. The authors claimed this as a fairly consistent feature in the convection although *Hughes and Bristow* (2003) were not able to identify these features for substorms occurring near periods of steady magnetospheric convection.

(b) Onset and expansion phase

Recent SuperDARN observations identified significant changes in convection 5-10 min prior to a substorm. These were claimed to be associated with substorm triggering because they occur just prior to the auroral brightening, but may be associated with the end of the growth phase. *Voronkov et al.* (1999) discovered that the azimuthal flow on the late duskside can significantly increase (by up to a factor of 2) 10-20 min prior to a substorm. This phenomenon was also seen, for individual events, by others (*Saka et al.*, 2001; *Bristow et al.*, 2001). The existence

of this effect is clear in observations made by *Provan et al.* (2004) who considered 64 individual substorms and made averaged convection maps (by epoch analysis) for various periods prior to and after the onset. Another noticeable feature in the convection magnitude is a burst of anti-sunward (meridional) flow in the midnight sector (*Watanabe et al.*, 1998) also occurring 10-20 min prior to onset.

Another effect of substorm related processes in convection is the formation of vortex-like flows near the onset time (*Lewis et al.*, 1997; *Yeoman et al.*, 2000; *Grocott et al.*, 2002; *Liang et al.*, 2004). *Grocott et al.* (2002) presented data for an isolated substorm and clearly showed the development of a CW vortex in the pre-midnight sector and a CCW vortex in the postmidnight sector. The vortices were seen centered slightly poleward of the auroral bulge, near its western and eastern borders. *Yeoman et al.* (2000) emphasized the role of meridional flows associated with these vortices while *Liang et al.* (2006) presented data consistent with the development of meridional flows within the bulge area powered by a couple of vortices as predicted by *Kamide and Kokubun* (1996).

A number of studies identified changes in convection after substorm breakups. These changes include a convection decrease within the bulge area during periods of enhanced precipitation, and enhanced flow around the expanding bulge of precipitation, especially at its poleward edge (e.g., *Morelli et al.*, 1995; *Yeoman et al.*, 2000; *Provan et al.*, 2004)

Jayachandran et al. (2003) investigated substorms that occur under the condition of a very stable and strongly negative B_z. They found a gradual prolonged decrease of the dayside/polar cap convection during the growth phase, with a sudden slowing of the flow near the onset and subsequent recovery to the initial convection intensity during the recovery phase. These results are in agreement with observations by *Lyons et al.* (2003) who concluded, based on a limited data set, that the convection experiences a sudden decrease a few minutes prior to the substorm onset on the dayside, in the area where plasma enters the polar cap. It should be noted that this effect was not always obvious, and *Bristow and Parris* (2006) presented data that do not support *Lyons et al.* (2003).

(c) Recovery phase

It is expected that convection would return to its original state, both in terms of its magnitude and overall pattern once the substorm is over. *Bristow et al.* (2003) and *Jayachandran et al.* (2003) emphasized this effect. However, data presented by *Provan et al.* (2004) show that plasma convection can experience an increase in magnitude ∼15-30 min after onset.

1.7.2 Sub-auroral polarization streams

Plasma convection observations made by satellites crossing the auroral oval in the evening sector showed the occasional occurrence of narrow westward plasma streams of unusually large magnitudes (up to 2-3 km/s) near the equatorward edge of the auroral oval (e.g.,*Galperin et al.*, 1974, 2002; *Spiro et al.*, 1979; *Anderson et al.*, 1991, 1993, 2001). Different terms have been in use to label these events: *Galperin et al.* (1974) called them 'polarization jets' while *Spiro et al.* (1979) and *Anderson et al.* (1991, 1993, 2001) called them 'sub-auroral ion drifts (SAIDs)'. Over the years, events of various intensities have been investigated and the criteria for classifying the events varied from one research team to another. For example, *Anderson et al.* (2001) specified the westward flow as being greater than 1000 m/s. *Karlsson et al.* (1998) defined the poleward directed sub-auroral electric field or SAEF associated with SAPS as "a poleward electric field exceeding 30 mV/m (ion drifts more than 600 m/s) with a latitudinal extension between 0.1^0 and 1^0 or magnetic latitude located between 50^0 and 65^0 corrected geomagnetic latitude." Analysis of ground based incoherent scatter radar data showed the occurrence of similar regions of fast flow under strongly disturbed conditions, but the observed flows were broader in latitude (*Yeh et al.*, 1991). At a March 2002 workshop at the Haystack observatory at the Massachusetts Institute of Technology, the single term sub-auroral polarization stream (SAPS) was adopted to describe polarization jets, SAIDs, SAEFs, and the more widespread events observed by radars (*Foster and Burke*, 2002).

Although the sub-auroral location of SAPS is generally accepted, the exact location in terms of magnetic latitude and magnetic local time (MLT) and the exact size of SAPS are less clear. Using a wide database of events, *Foster and Vo* (2002) and *Karlsson et al.* (1998) observed most events at approximately 60^0 MLat. SAPS generally occur in the evening sector, but may also extend into the morning sector (*Foster and Vo*, 2002). *Yeh et al.* (1991) reports SAPS events between 16:00 and 22:00 MLT. *Karlsson et al.* (1998) report events of varying strength between 18:00 and 03:00 MLT with the strongest events near 22:00 MLT while *Anderson et al.* (2001) report events between 16:00 and 24:00 MLT. Data from the Millstone Hill incoherent scatter radar estimate SAPS widths of $3^0 - 5^0$ (*Foster and Vo*, 2002). According to observations of consecutive satellite passes by *Anderson et al.* (1991) this width decreases throughout the lifetime of the event which lies between 30 minutes and three hours.

SAPS seem to be associated with the substorm processes (*Anderson et al.*, 1993). The majority of the SAEF events observed by *Karlsson et al.* (1998) occurred between 0 and 90 min from the start of the substorm recovery phase, with stronger events observed at shorter delays. *Galperin* (2002) reported the average delay from substorm onset as 30 min for events at 24 MLT and 1-2 hours for events in the pre-midnight evening sector. *Anderson et al.* (1993) agrees with this delay, adding that SAPS always occur during the recovery phase of a magnetic storm. SAPS locations in terms of latitude seem to be associated with the strength of magnetic activity, shifting equatorward along with the auroral oval as the Kp index increases (*Karlsson et al.*, 1998; *Foster and Vo*, 2002).

There are a number of views on the nature of SAPS. One of these has been formulated by their discoverer, Dr. Yuri Galperin. According to *Galperin* (2002), the inner edge of the ring current and radiation belts move Earthward due to the acceleration of energetic particles toward the Earth at substorm onset. Ions penetrate closer to the Earth than electrons. Different penetration depths mean the positive and negative charges are separated. Charge separation results in a polarization electric field directed radially outward, enhancing the westward motion of ions from

the nightside to the dayside due to curvature-gradient drift. The radially outward directed magnetic field is mapped to the high-latitude ionosphere as a northward directed electric field. This field is located between the equatorward boundaries of ion and electron precipitation and enhances the westward flow of ionospheric particles.

Previous observations of SAPS indicate that this phenomenon requires appropriate observational instrumentation. Although satellites are useful because of their good temporal resolution, the trajectory and orbital period ($\sim$ 100 min) of the satellite mean only localized regions may be studied at specific time intervals. It would be impossible to identify the beginning or end of an enhancement or to relate flow characteristics with substorm activity with such limited information, so a complete investigation of low latitude duskside flow enhancements would prove difficult.

Clearly, continuous observations with ground-based incoherent radars would allow for a more encompassing study. However, radars like the Millstone Hill incoherent scatter radar operate in a campaign mode. In this respect, a network of coherent high frequency (HF) radars is a very useful addition to the existing array of instruments capable of monitoring SAPS. Recently, the APL JHU Laboratory proposed an extension of the existing SuperDARN radars to mid-latitudes (*Greenwald*, 2004). This project has been successfully started with the launching of the Wallops Island mid-latitude radar (*Greenwald et al.*, 2006).

1.8 Objectives of the undertaken research

The major objective of this thesis is to investigate the possibility of studying SAPS with the Super Dual Auroral Radar Network (SuperDARN) HF radars. We specifically consider the King Salmon radar in Alaska. When this work began, previous attempts had been made to study SAPS with the Tasman International Geospace Environment Radar (TIGER) SuperDARN radar at Bruny Island in the Southern Hemisphere. Bruny Island radar observations showed great potential for contributions to SAPS studies even though the radar was designed to study high-latitude

phenomena. Unfortunately, observations of fast flows from the Bruny Island radar are not direct. An assumption was made that SAPS flows are L-shell aligned, and measurements in beams having L-shell angles of 45^0 were projected onto the L-shell direction to estimate the total velocity. This procedure may not always be justified, but is a reasonable first step toward resolving SAPS velocities. Observations from the Millstone Hill incoherent scatter radar (cited above) are made under the same assumption. We consider observations from the King Salmon radar which makes direct measurements in the L-shell direction due to the azimuthal orientation of its field-of-view.

Parkinson et al. (2005), while discussing Bruny Island radar observations of SAPS, report two events for which high-velocity echoes were detected by the King Salmon radar, indicating its potential for SAPS studies. It should be noted that an assessment of the King Salmon radar performance has never been published since the radar was commissioned in 2001. We expect to observe enhanced velocities in the dusk sector of the auroral and sub-auroral ionosphere, but whether other echo parameters would show other SAPS-like characteristics is unclear. For example, are these flows consistent with those measured by the Bruny Island radar, and are the flows statistically significant in terms of echo occurrence rate? Our goals for examining fast flows with the King Salmon radar are:

1. To statistically investigate King Salmon radar echo characteristics and compare them with observations from other SuperDARN radars.

2. To determine whether the high-velocity echoes observed by the King Salmon radar in the evening sector can be classified as SAPS in terms of their morphology and their occurrence with respect to the auroral oval, and whether the flows are detached from, or overlap with the auroral oval.

3. To explore the relationship between King Salmon high-velocity echoes and substorms.

The second objective of this thesis is a validation work of the quality of SuperDARN measurements/estimates of plasma convection. This work was performed

prior to the SAPS part of the thesis and was very useful because at that time a concern had been expressed that SuperDARN radars underestimate the convection velocity for fast flows >1 km/s. This effect is vital for SAPS studies with SuperDARN because these flows are expected to have velocities of up to 2-3 km/s. Concern regarding the quality of SuperDARN measurements was based on previous comparisons of SuperDARN convection and measurements by other instruments such as incoherent scatter radars, drift meters onboard satellites, and ionosondes. It is expected that inconsistencies in observation from various instruments are mostly due to different spatial and temporal resolutions of the instruments. Accordingly, our goals for the second objective of this thesis are:

1. To assess radar convection estimates at the raw data level through comparison with the Defense Meteorological Satellite Program (DMSP) satellites with special attention to high convection magnitudes.

2. To assess radar convection estimates after processing the raw data into global convection maps through comparison with DMSP.

1.9 Thesis outline

The rest of the thesis is organized as follows. Chapter 2 begins by describing the various ground based and satellite instruments used to accomplish the objectives of this thesis. Particular attention is given to describing the hardware, principles of operation, and data processing techniques for the SuperDARN coherent HF radars, and the drift meters onboard the DMSP satellites. Chapter 3 presents a comparison of SuperDARN radar velocities with ion drifts measured by DMSP satellites. Statistics are presented for SuperDARN measurements at the raw data level, which are then processed into global convection maps. Both raw and processed data are compared with DMSP observations. Chapter 4 concentrates on the second objective of this thesis and discusses observations of high-velocity echoes using the King Salmon radar. The radar performance is assessed by comparing King Salmon echo characteristics with other radars. The fast flows observed by King Salmon are fully

examined in terms of their location, magnitude, and relationship with substorms. In the final Chapter, a brief summary is presented, and suggestions for future research are discussed.

Chapter 2

Instruments

This thesis makes use of data from various ground-based and satellite instruments. Ground-based instruments include coherent HF radars and magnetometers, and satellite instruments include optical emission sensors, particle and electric/magnetic field sensors. In this Chapter we describe instrument hardware, principles of operation, and data processing techniques.

2.1 SuperDARN HF radars

SuperDARN is a system of coherent HF radars designed to continuously monitor high-latitude ionospheric plasma convection (*Greenwald et al.*, 1995). A coherent radar transmits radio waves into the ionosphere and examines the return signal or echo scattered off physical structures, such as wave-like perturbations in the electron density called irregularities. Such irregularities exist in the ionosphere in a broad range of scales allowing experimentation at various radio frequencies. The irregularities are formed whenever plasma instabilities amplify random density fluctuations above the level of background thermal fluctuations. The SuperDARN HF radars are sensitive to irregularities elongated in the magnetic field direction. For effective backscatter, the radio wave fronts should propagate perpendicularly to the magnetic field.

The SuperDARN radars were chosen to operate in the HF band (8-20 MHz). At these frequencies, radio waves experience significant refraction in the ionosphere and can meet the orthogonality condition at a broad range of heights, from 90 to 500 km. For HF backscatter to occur, the ionospheric irregularity should be of a

Table 2.1: SuperDARN radar locations and boresight directions.

Radar Station	Geog. Lat. (^{0}N)	Geog. Long. (^{0}E)	AACGM Lat. (^{0}N)	AACGM Long. (^{0}E)	Boresight Direction (^{0})
King Salmon	58.68	-156.65	57.43	-100.51	-20.0
Kodiak	57.61	-152.19	57.17	-96.28	30.0
Prince George	53.98	-122.59	59.88	-65.67	-5.0
Saskatoon	52.16	-106.53	61.34	-45.26	23.1
Kapuskasing	49.39	-82.32	60.06	-9.22	-12.0
Goose Bay	53.32	-60.46	61.94	23.02	5.0
Stokkseyri	63.86	-22.02	65.04	67.33	-59.0
Pykkvibaer	63.77	-20.54	64.48	68.48	30.0
Rankin Inlet	62.82	93.11	72.96	-28.17	5.71
Hankasalmi	62.32	26.61	59.78	105.53	-12.0
Wallops Island	37.93	-75.47	30.93	75.52	26.14
Halley	-75.52	-26.63	-61.68	28.92	165.0
Sanae	-71.68	-2.85	-61.52	43.18	173.2
Syowa South	-69.00	39.58	-55.25	23.00	165.0
Syowa East	-69.01	39.61	-55.25	22.98	106.5
Kerguelen	-49.35	70.26	-58.73	122.14	168.0
Bruny Island	-43.38	147.23	-55.31	-133.36	180.0
Unwin	-46.51	-168.38	-55.15	-106.54	227.9

specific size: $\lambda_{irr} = \lambda_{radar}/2$ (*Fejer and Kelley*, 1980). Since the radars operate at 8-20 MHz, they can see scatter from irregularities with 8-19 m wavelengths.

In the common mode of operation, each SuperDARN radar sequentially scans through 16 beam positions over 2 min with a dwell time of 7 s for each beam position. There is also a fast common mode, with a scan time of 1 min and a dwelling time of 3 s. Each beam position is separated by 3.24^0 and the azimuthal range of the combined beams is $\sim 52^0$. Observations are made in 75 radar cells, 45 km apart, starting from a range of 180 km in each beam.

There are currently 18 SuperDARN radars in operation, 11 in the Northern Hemisphere and 7 in the Southern Hemisphere. The name, location, and boresight of the SuperDARN radars are listed in Table 2.1, and the radar locations are shown in Figure 2.1.

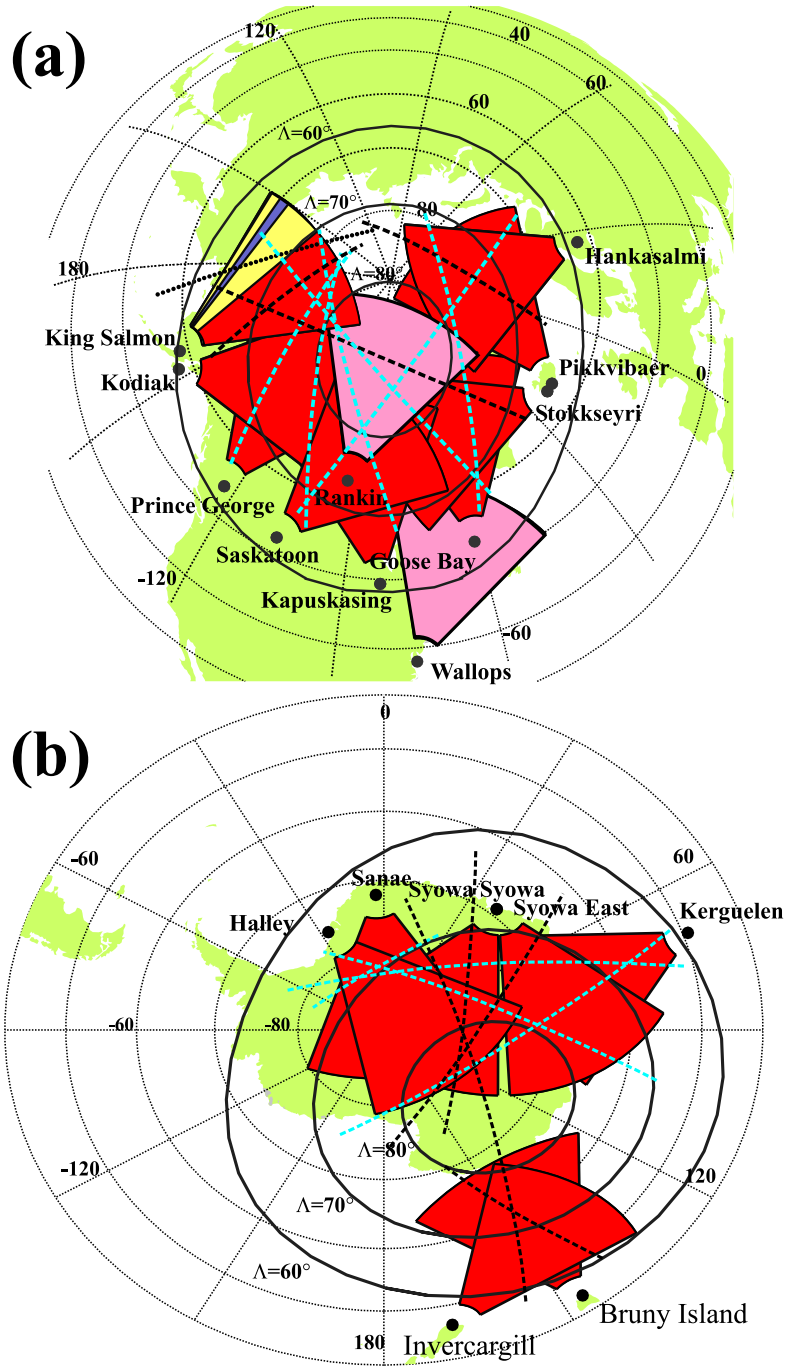

Figure 2.1: (a) Fields of view of the Northern Hemisphere SuperDARN radars for ranges of 400-2800 km, with King Salmon beams 0-5 highlighted and beam one indicated by dark shading. Light shading indicates radars not yet available for study when this research was performed. (b) Fields of view of the Southern Hemisphere SuperDARN radars. In both panels, typical footprints of DMSP satellite F12 (dashed lines) and F15 (dotted line) are overplotted. Blue lines indicate trajectories from which data were used for the comparison in Chapter 3.

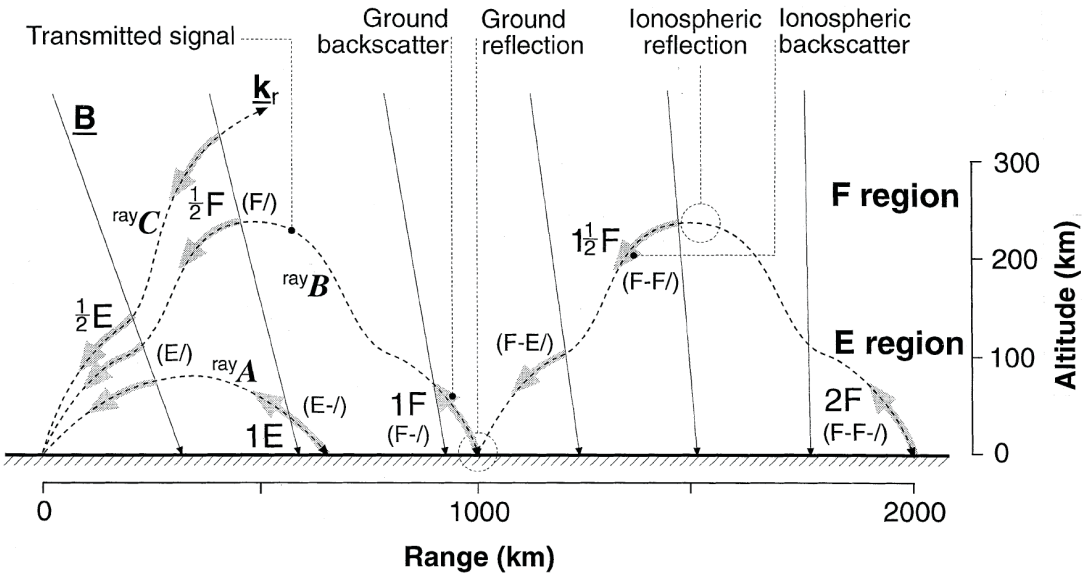

Figure 2.2: Possible propagation modes for radio wave backscatter with two types of nomenclature given (Milan, 1997).

We should note that SuperDARN is a continuously enlarging network. Several new radars are under construction both in the Northern and Southern Hemispheres, including a recently installed radar at Wallops Island. This radar is located at middle latitudes and overlooks territories in the Eastern United States and Canada, southern Greenland and the western Atlantic ocean. The Wallops Island radar is special as it is capable of detecting echoes at magnetic latitudes as low as $\sim 50^0$ and is therefore useful for studying the sub-auroral ionosphere.

2.1.1 Propagation modes

HF radio waves may follow several different propagation paths in the ionosphere, Figure 2.2. Whole hop propagation occurs when a radio wave is transmitted, reflected from the ionosphere to the ground and back to the receiver. This is denoted, for example, as 1E, 1F, 2F propagation where the integer describes the number of complete hops and the letter describes the ionospheric region from which the wave is reflected before scattering off the ground. This kind of scatter is called ground scatter and is characterized by a near zero Doppler shift (the ground does not move!) and a small spectral width. Ionospheric scatter occurs when radio waves are reflected

from the ionosphere, possibly after being reflected off the ground, and back along the same path. Such scatter is labeled, for example, as $\frac{1}{2}$E, $\frac{1}{2}$F, $1\frac{1}{2}$ E, $1\frac{1}{2}$ F, where the fraction indicates the number of hops made, and the letter indicates where the ionospheric backscatter occurred.

In addition to whole and half hop propagation, radio waves may also propagate between the E and F regions before being reflected. We denote this scatter by using letters to indicate the ionospheric region, a dash to indicate ground reflection, and a slash to indicate when the propagation ends and the radio wave returns to the receiver. For example, a radio wave propagating from the radar to the F region, to the E region and back along the same path to the radar is denoted by FE/.

2.1.2 FITACF approach to data analysis

SuperDARN radars emit a series of radio wave pulses to determine the Doppler velocity, power spectrum, and spectral width of echoes. This is accomplished by digitizing and processing the return signal of a specific sequence of pulses into an autocorrelation function (ACF). The current pulse sequence, Figure 2.3, consists of a series of 8 pulses of 300 μs length emitted at multiples of 14, 8, 2, 3, 4, 11, and 1 units of lag time t, where t =1.5 ms. A radar cannot transmit and receive at the same time, so some lags are not available to allow the radar to transmit a signal. The result is a pulse sequence with 29 good lags (including the zero lag) and 15 bad lags. The pulse sequence is repeated $\sim$70 times and averaged into the ACF.

The FITACF approach is used to examine the ACFs. Figure 2.4 plots an example of how the ACF is analyzed (*Villain et al.*, 1987). Figure 2.4a plots the real and imaginary components of the ACF against lag number. The signal decay is assumed to follow either a Gaussian (σ) or an exponential (λ) distribution. The rate of change of the phase angle is plotted in Figure 2.4c. The slope of the best-fit line to this plot is the Doppler frequency, ω_D, and is used to determine the Doppler velocity of the irregularity:

$$v_{Doppler} = \frac{c\omega_D}{4\pi f_{radar}}, \tag{2.1}$$

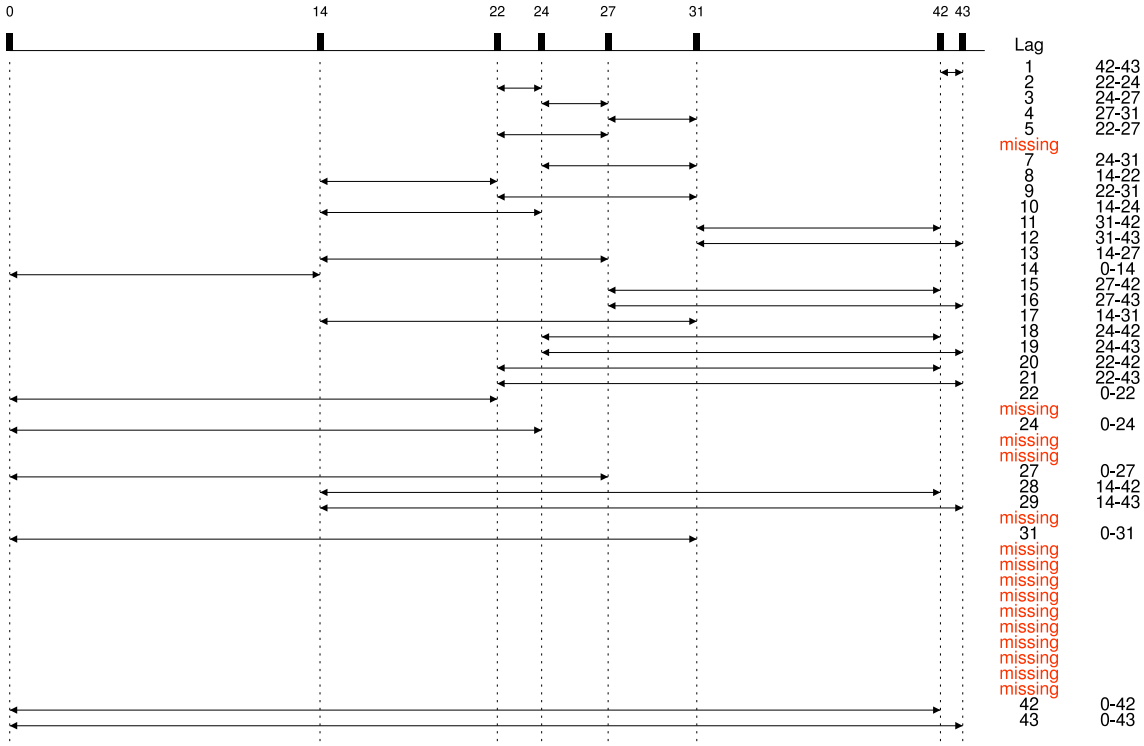

Figure 2.3: The 8-pulse or "katscan" sequence currently used in SuperDARN observations.

where c is the speed of light in a vacuum. Power and spectral width are determined by modeling the decay of the ACF. Figure 2.4d plots the signal power decay fitted with both exponential and Gaussian approximations. In this thesis we use an exponential distribution of the form:

$$P(\tau) = P_\lambda e^{-\lambda\tau}, \tag{2.2}$$

where P_λ is the maximum backscattered power. The constant λ is determined using a least-square fit, and used to calculate the width of the spectrum from

$$width = \frac{c\lambda}{2\pi f_{radar}}. \tag{2.3}$$

Figure 2.4b graphs the magnitude of the fast Fourier transform (FFT) of the ACF shown in Figure 2.4a. The vertical and horizontal lines indicate the velocity and spectral width calculated by equations (2.1) and (2.3) using the exponential approximation.

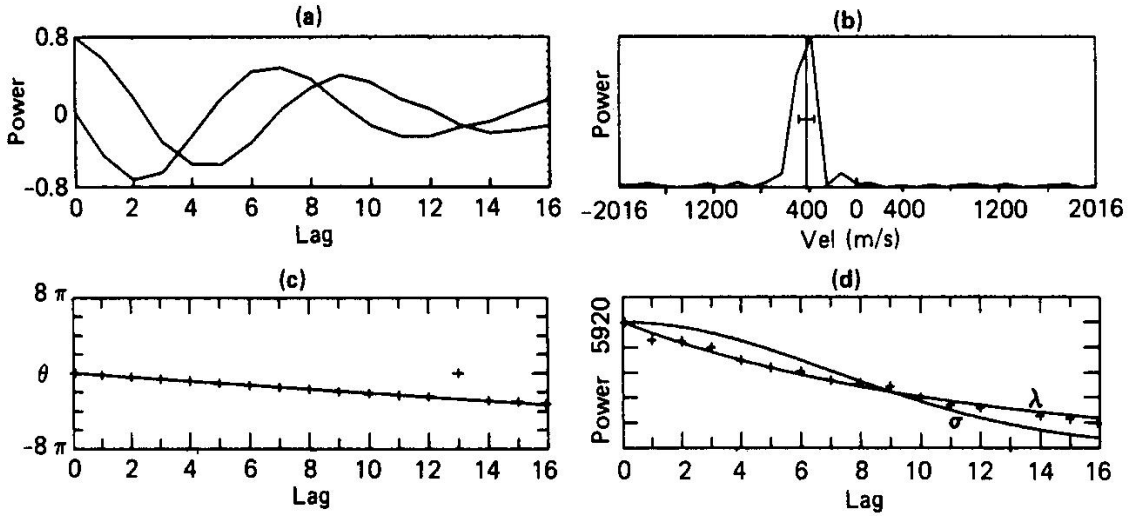

Figure 2.4: (a) Real and imaginary part of the ACF. (b)magnitude of the FFT of the ACF with velocity (vertical line) and spectral width (horizontal line) obtained using FITACF overplotted. (c) Rate of change of the phase angle. (d) ACF power decay for exponential (λ) and Gaussian (σ) least-square fits (*Villain et al.*, 1987).

2.1.3 Two-dimensional convection mapping

In this study, examining plasma flow on a global scale is accomplished by processing SuperDARN l-o-s velocities from multiple radars using the technique developed by *Ruohoniemi and Baker* (1998) using a 6 harmonics approximation. In a single scan, each radar has a data set of 16×75 cells. Observations in cells classified as ground scatter and in cells having velocity error estimates >200 m/s are discarded. For each cell of interest, c_i, occurring at scan t_i, a data set is generated including observations from the 3×3 region of cells centered on c_i for the three scans centered at scan t_i. The data set is then median-filtered. The uncertainty in each velocity is determined by calculating the standard deviation of the data set used for median filtering, discarding any points more than 2 standard deviations from the mean of the data set and re-calculating the standard deviation. Velocity is determined in each radar cell for all radars and organized into bins of 1^0 of magnetic latitude. To determine the global convection pattern, an electrostatic potential from the empirical model is fitted to these filtered velocities and then used to generate separate convection velocity vectors. In this research we will consider both the raw l-o-s

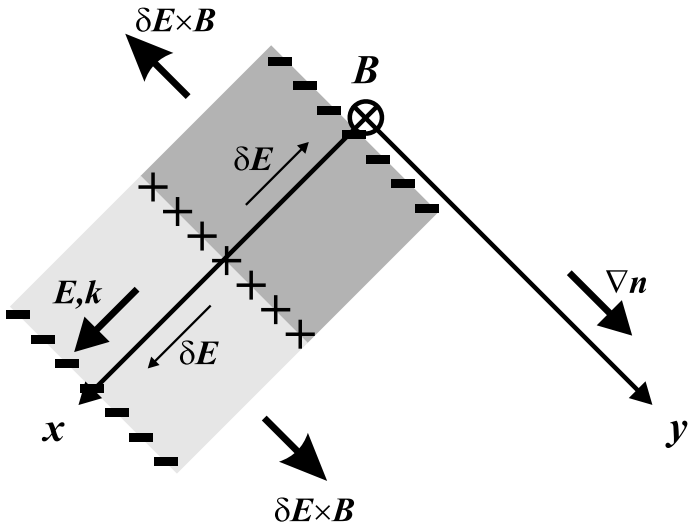

Figure 2.5: Ionospheric configuration for the gradient drift instability in the F region. Dark shading indicates density enhancement and light shading indicates density depletion.

velocities from individual radars and global convection data obtained from multiple radars.

2.1.4 Plasma irregularities at F region heights and mechanisms of their production

Since the SuperDARN radar network is the major instrument for this thesis, we now make a short review of the linear theory of ionospheric irregularity formation.

It is a general consensus that the gradient-drift plasma instability is the most likely mechanism of decameter irregularity production in the high-latitude F region. We must first explain why the thermal plasma fluctuations can become intensified and therefore detectable by a radar.

Consider an F region plasma with a downward directed magnetic field, an electric field in the x-direction, an increasing plasma density in the y-direction, and assume a sinusoidal perturbation in the electron density is established parallel to the electric field, so that the wave vector, $\boldsymbol{k}$, points along the electric field, Figure 2.5. In Figure 2.5 the dark shading indicates a density enhancement in the perturbation, and the light shading indicates a density depletion. Analysis of equation (1.5) for

an F region plasma indicates there is a charge separation along the direction of the electric field due to the different electron and ion Pedersen drifts. As a result, charges build up on wave fronts. The resultant charge separation causes polarization electric fields, $\delta\mathbf{E}$, to form along the x-direction as shown. In the presence of the electric field $\delta\mathbf{E}$ and the magnetic field $\mathbf{B}$, regions of enhanced plasma $\delta\mathbf{E}\times\delta\mathbf{B}$ drift into low-density regions, and regions of depleted plasma $\delta\mathbf{E}\times\delta\mathbf{B}$ drift into high-density regions. Redistributing the plasma in this way enhances the contrast between the background density and the density in the perturbation, implying irregularity growth.

To describe the instability quantitatively, consider a more general case where $\boldsymbol{k}$ is directed at an angle θ from the y-axis. The frequency and growth rate of the perturbation can be determined as follows. First consider the simplified equation of motion in the cold approximation neglecting the effects of particle inertia, ion-electron collisions and the neutral wind (equation 1.2). (For a complete derivation, including ion-electron collision and temperature effects, see *Xu* (2003)).

Also consider the continuity equation for ions and electrons

$$\frac{\partial n_\alpha}{\partial t} + \nabla\left(n_\alpha \mathrm{v}_\alpha\right) = 0. \tag{2.4}$$

Assume a sinusoidal perturbation in n_α, $\mathbf{E}$, and $\mathbf{v}_\alpha$

$$\delta n_\alpha, \delta\mathbf{E}, \delta\mathbf{v}_\alpha \propto e^{-i\omega t + i\mathbf{k}\cdot\mathbf{r}}, \tag{2.5}$$

such that $\delta n_\alpha \ll n_\alpha$, $\delta E \ll E$, and $\delta \mathrm{v}_\alpha \ll \mathrm{v}_\alpha$, and derive expressions for the particle velocity in terms of $\delta\mathbf{E}$. The velocity $\delta\mathbf{v}_\alpha$ is given by equation (1.5) with $\mathbf{v}_E \rightarrow \delta\mathbf{v}_E$ and $\mathbf{E}_\perp \rightarrow \delta\mathbf{E}$. Next, assume quasi-neutrality ($\delta n_i = \delta n_e = \delta n$) and that the perturbation in the electric field can be replaced by the gradient of the electrostatic potential ($\mathbf{E} = -\nabla\Phi$). By isolating the perturbed quantities from the background, the simplified equation of motion (1.2) and the continuity equation (2.4) can be worked into the following dispersion equation:

$$(-i\omega + i\mathbf{k}\cdot\mathbf{v}_e)\left[k^2 - \frac{1}{L}\left(ik_x\frac{\Omega_i}{\nu_{in}} + ik_y\right)\right] - \beta(-i\omega + i\mathbf{k}\cdot\mathbf{v}_i)\left[k^2 - \frac{1}{L}\left(ik_x\frac{\Omega_e}{\nu_{en}} + ik_y\right)\right] = 0, \tag{2.6}$$

$$\text{where} \qquad \beta = \frac{\nu_{en}\Omega_e}{\nu_{in}\Omega_i}\frac{\Omega_i^2 + \nu_{in}^2}{\Omega_e^2 + \nu_{en}^2}, \tag{2.7}$$

and L describes the plasma gradient and is given by

$$\frac{1}{L} = \frac{\nabla n}{n}. \tag{2.8}$$

We assume $\omega = \omega_r + i\gamma$, where ω_r and γ are the frequency and growth rate of the perturbation, respectively. Equation (2.6) can be solved for both ω_r and γ by assuming $\gamma \ll \omega_r$ to obtain

$$\omega_r = k\mathrm{v}_E \cos\theta, \qquad \text{and} \tag{2.9}$$

$$\gamma = \frac{\mathrm{v}_E}{L}. \tag{2.10}$$

Equation (2.9) gives an expression for the irregularity phase velocity

$$v = \frac{\omega}{k} = \mathrm{v}_E \cos\theta. \tag{2.11}$$

According to Equation (2.10), a large $\mathbf{E}\times\mathbf{B}$ drift and a large plasma gradient result in a faster irregularity growth rate. These are preferable conditions for the onset of irregularities and HF radar echo detection.

Equation (2.11) indicates that to a first approximation, irregularities move at a velocity equal to the component of the $\mathbf{E}\times\mathbf{B}$ drift along the direction of propagation. This justifies the assumption used in the SuperDARN radar method.

The above description is over simplified. The full theory should include temperature effects, chemistry, and non-linear effects. The linear theory has been considered for a more general case elsewhere (e.g. *Xu*, 2003) while the non-linear study of the instability has been performed, for example, by *Guzdar et al.* (1998). It is important to note that the the gradient-drift plasma instability in the F region can only directly generate irregularities with a scale-size of 10s of meters. The 10 m scale-size irregularities observed by SuperDARN radars are obtained through the non-linear cascading of energy from large to small scale-sizes (*Tsunoda*, 1988).

2.2 DMSP drift meter and particle precipitation detector

The Defense Meteorological Satellite Program (DMSP) (*Greenspan et al.*, 1986; *Rich and Hairston*, 1994) consists of a series of weather satellites in circular orbit about the Earth at an approximate altitude of 840 km at a 98.7^0 inclination. Each polar orbiting satellite moves at ∼7.5 km/s with an orbital period of ∼100 minutes. The satellite's orbital precession is such that the satellite is locked to a specific local time throughout the year. Of the instrument complement, only the plasma convection meters and the particle sensor are used for this research.

2.2.1 Measurements of flow velocity using SSIES

Plasma measurements are performed onboard each spacecraft with a thermal plasma detector array called Sensors-Ions, Electron, and Scintillation (SSIES). The SSIES instrument has four sensors, of which two are of interest: the Ion Drift Meter (IDM) and the Retarding Potential Analyzer (RPA). Both the IDM and RPA are mounted in a common ground plane facing the direction of motion of the satellite. The aperture to each instrument is covered by a series of fine wire grids, which are charged to repel electrons and allow ions to pass through without disturbing the original flow direction. Both instruments measure the current from the incoming plasma to the collector surfaces.

The RPA measures the along-track component of the ion drift, ion temperature, ion density, and the proportion of H^+, He^+, and O^+ in the plasma. In the analysis, a plot of the derivative of the ion current to the RPA collector surface with respect to the retarding potential is made. Typically, the graph consists of several minima corresponding to the different ion species. The relative location of the peaks depends on the ambient ion velocity normal to the collector surface. By performing a non-linear least-squares fit, the bulk velocity of the ions with respect to the spacecraft and other parameters are determined.

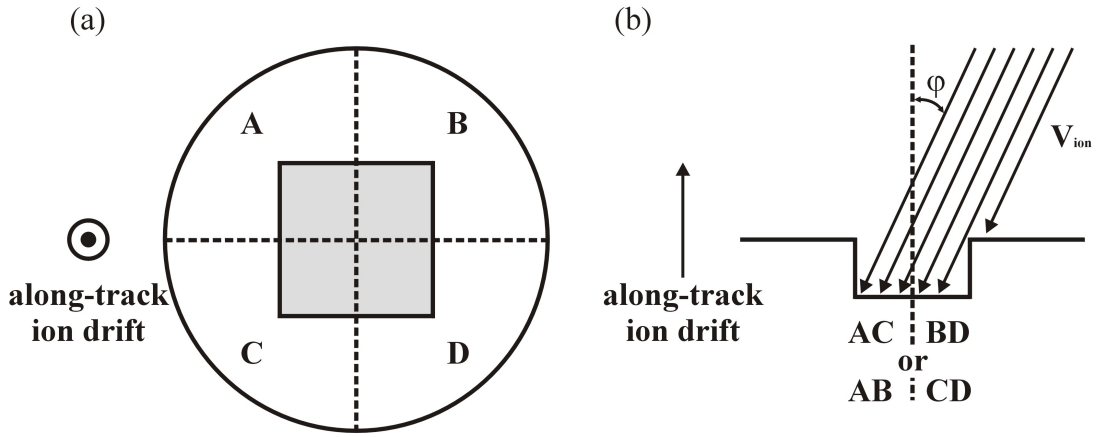

Figure 2.6: (a) Front view of the DMSP IDM aperture (square) and collector plate (segmented circle), with the satellite motion pointing out of the page. (b) Collection of ions onto the collector plate under the influence of a cross-track ion drift.

The IDM is used to determine the cross-track component of the ion velocity with respect to the Earth. This is done by measuring the angle of arrival of the O^+ ions. Consider the front-view of the collector illustrated in Figure 2.6a. Ions flow into the square aperture of the detector onto a circular collector plate, which is divided into four quadrants. The aperture and collector plate face the direction of motion and the cross-track direction is in the plane of the page. The currents to both the top and bottom and left and right halves of the collector plate are measured. Now consider the side-view of the collector plate shown in Figure 2.6b. If the ion drift has a cross-track component, the geometry of the instrument will cause more ions to fall on one half of the collector plate than the other, and there will be a current difference between halves. The difference in the logarithms of the two currents is directly proportional to the tangent of the angle of arrival of the ions, given by ϕ in Figure 2.6b. Through simple geometry, the cross-track component of the ion drift can be determined if the along-track component is known. The along-track component of the ion drift with respect to the Earth is the sum of the ambient ion velocity normal to the collector surface and the spacecraft velocity ($\sim$7.5 km/s). If the RPA data do not provide the ambient ion velocity with respect to the satellite, then the along-track velocity with respect to the Earth is assigned the velocity of the spacecraft. In this case, the IDM measurements can have an error of up to 10%

(*Rich and Hairston*, 1994; *Greenspan et al.*, 1986). The IDM procedure also assumes that the major ion is O^+; it is desirable for the percentage of O^+ ions to be greater than 85%.

2.2.2 Quality determination

Limitations to DMSP data processing techniques make categorizing the accuracy and quality of the data set necessary. The instruments require a plasma density of 10^3 cm^{-3} to provide ion currents large enough to be measured by the three ion sensors, and plasma densities greater than 10^6 cm^{-3} cause saturation of the instrument electronics. Due to these limitations, as well as those discussed in the previous section, each 4-s averaged IDM and RPA data point is assigned a quality tag of 1 (measurement is reliable), 2 (measurement is questionable, use with caution), 3 (measurement is poor), or 4 (measurement quality is undetermined). Quality tag assignment is based on the presence of data within a 4 s interval, plasma density, and the proportion of O^+ in the plasma. It should be noted that whenever the along-track component of the ion drift from the RPA is not directly measured, the corresponding IDM measurement is automatically assigned an undetermined quality tag. Data points assigned a poor quality tag were discarded in this analysis.

2.2.3 Particle precipitation detector

Along with plasma flow speed, the DMSP satellite is also able to measure particle fluxes. The SSJ/4 detector measures the flux of incoming electrons and ions in 20 energy channels in the range of 30 eV to 30 keV, at a resolution of one complete spectrum of measurements per second. The instrument sensors are oriented so they point radially outward from the Earth. In this study we use the SSJ/4 observations to determine the ion and electron auroral boundaries. This is done by examining a log energy versus universal time (UT) plot of flux intensity. The satellite location in terms of latitude and longitude can be determined for every instant of UT. Both ion and electron flux plots are generally characterized by a region of high flux intensity

in all channels bounded by a region of lower flux intensity, particularly in high energy beams. The high and low-latitude transitions between high and low flux intensity correspond to the poleward and equatorward boundaries of the electron and ion auroral precipitation. The region of intense electron precipitation characterizes the auroral oval. In this study, the SSJ/4 detector is used to locate the equatorward edge of the auroral oval for comparison with the position of flow features identified in the cross-track ion drift measured by the IDM.

2.3 IMAGE optical camera

The Imager for Magnetopause-to-Aurora Global Exploration (IMAGE) mission uses a satellite to image the Earth's magnetosphere (*Burch*, 2000). The satellite orbits the Earth at a 90^0 inclination at an altitude of 1000 km (perigee) to 7 R_E (apogee). Among the instrument complement is a series of three far ultraviolet imaging (FUV) instruments which monitor the size, intensity, and location of the auroral oval. We are particularly interested in the wideband imaging camera (WIC) (*Mende et al.*, 2000). WIC images the LBH N2 band of the aurora at 140-190 nm wavelengths. As the satellite orbits, WIC has a complete view of the auroral oval whenever the satellite has an altitude greater than 4-5 R_E. For example, at apogee the field of view subtends at least 16^0, and the auroral oval subtends 8^0. The FUV WIC looks radially outward from the satellite which spins on an axis perpendicular to the orbital plane at a rate of one spin every two minutes. As the satellite spins, each auroral feature viewed by WIC remains in the field of view for 10 s. The instrument takes approximately 300 pictures of the auroral region during this time and superimposes them into one image by offsetting the pictures according to the satellite rotation.

One valuable use for the IMAGE FUV WIC is substorm observation. Not only may we observe substorm particle injections with WIC, but we may track the substorm evolution by monitoring the westward and poleward expansion of the auroral oval.

2.4 Other instruments

In the course of this research, other instruments have been used to monitor various geophysical parameters. Solar wind monitoring was achieved with the Advanced Composition Explorer (ACE) satellite (*Stone et al.*, 1998). ACE orbits the Earth at the Sun-Earth libration point, about 240 R_E sunward of the Earth. Its position makes it ideal for measuring the IMF and solar wind properties before the solar wind impacts the Earth's magnetosphere. This study makes use of two triaxial flux-gate magnetometers mounted facing the Sun to measure the three dimensional IMF. The solar wind electron, proton and alpha monitor (SWEPAM) is also used to measure the characteristics of the solar wind, such as velocity, to determine the solar wind propagation time from the satellite to the Earth so the magnetometer data may be delayed accordingly. ACE has a time resolution of about one minute and transmits in real time. In addition to the IMF, the Earth's magnetic field was examined using Alaskan fluxgate magnetometers. The H-component of the Earth's magnetic field was observed using Kaktovik and Gakona from the Geophysical Institute Magnetometer Array (GIMA) magnetometer chain, and Pi2 pulsations were determined using Dawson data from the Canadian Auroral Network for the OPEN Program Unified Study (CANOPUS) (now known as the Canadian Array for Realtime Investigations of Magnetic Activity (CARISMA)) magnetometer chain. Finally, the geostationary Los-Alamos National Laboratory (LANL) satellite was used to monitor the influx of energetic protons in the 50-400 keV range.

Chapter 3

Comparison of SuperDARN line-of-sight velocities and convection vectors with DMSP cross-track ion drifts

The SuperDARN project was originally intended to use scatter from F region irregularities because they were expected to propagate with a velocity close to the $\mathbf{E}\times\mathbf{B}$ drift of the bulk plasma (*Greenwald et al.*, 1995). In this way, ionospheric irregularity velocity saturation at the ion-acoustic speed for E region scatter (e.g., *Nielsen and Schlegel*, 1985) was not anticipated from the outset. Unfortunately, SuperDARN measurements do occasionally suffer from this problem when E region echoes with saturated velocities are received through multiple hop propagation at ranges where F region echoes are expected (*Milan et al.*, 1997; *Lacroix and Moorcroft*, 2001).

Problems are not anticipated in deriving SuperDARN convection from the l-o-s velocities of F region echoes. However, validation work is still necessary as convection measurements from other instruments, such as satellites and incoherent scatter radars (ISRs), are often combined to obtain a global ionospheric convection pattern. When combining data from multiple convection-monitoring instruments, one must be confident the data are compatible. Difficulties might arise over the different spatial and temporal resolutions of the instruments. Satellite and incoherent scatter radar measurements are localized in space and time. For example, ISRs measure F region plasma flow in areas of $\sim$10 km in diameter with a temporal

resolution of 1-5 min. In contrast, SuperDARN offers continuous measurements over extensive areas. SuperDARN radars measure velocities with spatial and temporal resolutions of 45 × 100 km (at typical F region ranges) and ∼(3) 7 s respectively. The raw data are merged into one block to produce a convection map under the assumption of a stable convection pattern over (1) 2 min. One expects differences between convection estimates from simultaneously operating instruments, even for observations having similar ionospheric locations.

In this Chapter we perform a comparative study between SuperDARN radar measurements of plasma drifts and DMSP satellite observations. Results presented in this Chapter were reported at various meetings and eventually published (*Drayton et al.*, 2005).

3.1 Review of previous comparisons

Baker et al. (1990) were the first authors who investigated the compatibility of Halley convection velocities and the bulk plasma flows as observed by the DMSP ion drift meter. They considered data for one satellite pass and showed that the radar velocities were close to the ion drifts, with a tendency for radar velocities to be smaller than satellite ion drifts for velocity magnitudes >600 m/s (their Figure 3). *Xu* (2003) examined 40 DMSP passes over the Saskatoon-Kapuskasing radar pair field of view. He showed that both the merge (*Greenwald et al.*, 1995) and map potential (*Ruohoniemi and Baker*, 1998) techniques give convection estimates in agreement with DMSP cross-track ion drifts but the SuperDARN velocities were somewhat smaller than concurrent DMSP ion drifts for large drift magnitudes.

In a series of papers, joint SuperDARN and ISR convection observations have been considered (*Milan et al.*, 1999; *Davies et al.*, 1999, 2000; *Xu et al.*, 2001; *Danskin*, 2003). These comparisons also showed overall consistency between data sets, but there was a noticeable data spread. For some events, almost perfect agreement was reported (*Davies et al.*, 1999; *Danskin*, 2003) while for others significant systematic differences were obvious (*Xu et al.*, 2001; *Danskin*, 2003). These findings

are in agreement with earlier ISR-HF radar comparisons by *Villain et al.* (1985) and *Ruohoniemi et al.* (1987).

Despite the overall positive outcome of validation work for the SuperDARN measurements of the convection velocity in the F region, the United States National Science Foundation Upper Atmosphere Review Committee on Facilities has recently (2004) outlined the continuation of such work as a priority. This request is indeed justified as various comparisons showed occasional cases of significant differences between the convection estimates of various instruments.

For this thesis, there is an additional reason to examine SuperDARN velocity measurements using another instrument. The major goal of this thesis is to investigate whether existing (as of 2004) Northern Hemisphere SuperDARN radars can monitor very fast flows at the equatorial edge of the auroral oval, SAPS (Section 1.7.2). Observations using satellites and incoherent scatter radars have shown exceptionally large dusk-side convection velocities up to 2-3 km/s (*Galperin et al.*, 1974; *Anderson et al.*, 1991, 2001; *Yeh et al.*, 1991; *Karlsson et al.*, 1998; *Foster and Vo*, 2002). Generally, these high velocities are seldom observed in SuperDARN measurements (e.g., *Lacroix and Moorcroft*, 2001).

3.2 Comparison of SuperDARN line-of-sight velocities and DMSP cross-track ion drifts

We considered joint SuperDARN and DMSP satellite measurements of the plasma convection. We chose the DMSP satellites for comparison due to data availability and the possibility of comparison at the raw data level. This way, SuperDARN reprocessing techniques that modify the original data are avoided. The DMSP satellites cross each of the SuperDARN radars' fields of view at a variety of ranges, so we were able to test various radars at various ranges. In this Section we first compare DMSP cross-track ion drifts and SuperDARN HF l-o-s velocities in approximately the same direction of observation. We perform a further analysis by comparing DMSP cross-track ion drifts and full SuperDARN convection vectors.

3.2.1 Approach to the l-o-s comparison and event selection

We considered routine SuperDARN l-o-s data gathered in the standard mode of operation at various locations in the Northern and Southern Hemispheres. Only measurements for which the echo power was more than 3 dB, the spectral width was less than 500 m/s, and the uncertainty in the velocity determination was less than 150 m/s were considered. An error in the velocity fit was accepted as the uncertainty of its determination. In addition, we discarded those radar echoes whose velocity magnitude was less than 50 m/s as low velocity echoes often show the presence of a ground scattered component. Such restrictions to the data set helped to eliminate many untypical echoes. We did not consider events where there was a transition in the polarity of the DMSP drift near the area of comparison, because for these cases velocity differences can be explained by the different spatial resolutions of the instruments.

We also considered the quality of the DMSP data. For several events, the DMSP measurements with undetermined quality flags were accepted if the spatial variation of the ion drift along the satellite track was smooth so these points seemed to be consistent with those of good quality.

Any given DMSP satellite crosses an individual SuperDARN radar field of view once every 100 min. Even though the radar operates continuously, there is always a time difference between the radar and satellite measurements. In the standard mode of operation, every SuperDARN radar scan starts at the beginning of each minute (1-min scan) or at the beginning of every two minute interval (2-min scan). We chose radar scans within 1-2 min of the time the satellite crossed the center of the radar field of view. This is consistent with the 1- (2-) min inherent resolution of SuperDARN observations. To achieve reasonable data statistics, observations over two-three years of radar operation (1999-2002) were considered by sequential search through the SuperDARN quick-look plots. Our goals were to select about twenty passes with reasonable quality, and to obtain about fifty points of comparison for each radar.

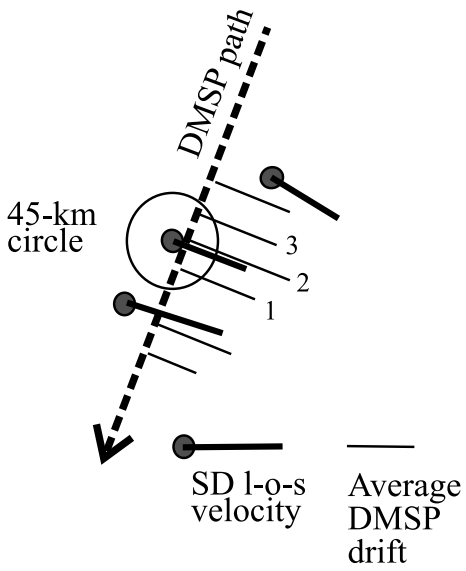

Figure 3.1: A scheme illustrating the averaging of DMSP cross-track ion drifts for comparison with SuperDARN (SD) line-of-sight velocities (*Koustov et al.*, 2005a).

To compare radar and satellite data, the following procedure was implemented, Figure 3.1. DMSP passes which almost perpendicularly cross several of an individual radar's beams were identified. The condition of orthogonality allows for a direct comparison between the SuperDARN and DMSP measurements. The DMSP ion drift data were assigned to corresponding footprints of the satellite mapped down from an orbital altitude of 840 km to 300 km, which is the assumed height of SuperDARN F region scatter. For mapping the satellite location along magnetic field lines, the International Geomagnetic Reference Field (IGRF) model was used. Mapping the DMSP ion drifts from 840 km to 300 km in altitude results in an average reduction of the velocity magnitude by 11%, as was recently estimated by *Sofko and Walker* (2006). The original comparison presented by *Drayton et al.* (2005) did not consider this effect and the findings were slightly different from what we report in this thesis. For every selected radar, the DMSP points separated from the center of the radar cell by not more than 45 km were identified and averaged to obtain the DMSP ion drift. Since the satellite moves at $\sim$7.5 km/s and has a time resolution of 4 s, at least 3 DMSP points were available for averaging. The standard deviation of measurement was considered as an estimate of the uncertainty of the DMSP ion drift. Only points with a standard deviation less than 150 m/s were considered in

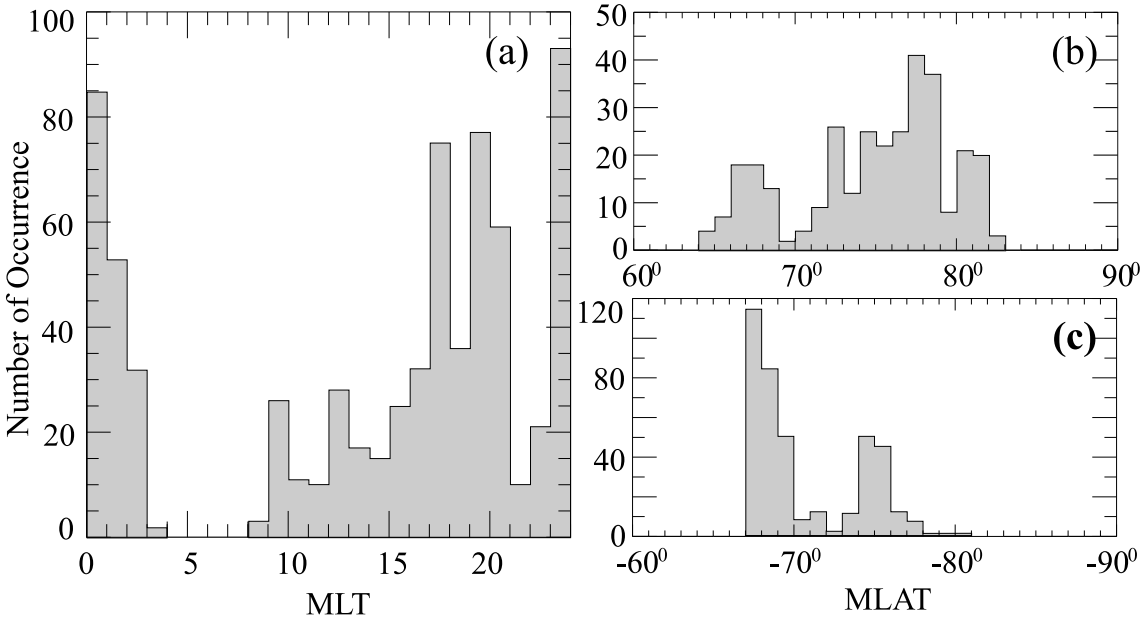

Figure 3.2: Histogram distributions of the (a) magnetic local times and AACGM magnetic latitudes for (b) the Northern and (c) the Southern Hemisphere for SuperDARN echoes selected for comparison with DMSP measurements.

the comparison. Originally, we allowed various degrees of misalignment between the DMSP cross-track direction and the SuperDARN radar beam, but the final statistics included only those measurements for which the difference was less than 5^0.

There was another factor significantly limiting the number of joint DMSP - SuperDARN events. Typically, the satellites do not cross the radars beams exactly perpendicularly. Figure 2.1 gives an example of several DMSP F12 tracks in both hemispheres (mapped down to 300 km) and the SuperDARN radars fields of view between ranges of 400 km and 2800 km (at a height of 300 km). Blue lines show passes potentially useful for comparison with radar observations.

In this study we consider 9 radars: Hankasalmi, Pykkvibaer, Stokkseyri, Saskatoon, and Kodiak in the Northern Hemisphere and Halley, Sanae, Syowa-South, and Syowa-East in the Southern Hemisphere. For the Kodiak radar, data were considered in two distinctly different range bands, at approximately 1100 km and 2300 km, to explore a potentially important range effect using a single radar.

Figures 3.2 and 3.3 provide statistical characteristics of radar echoes considered in this comparison. There were echoes in most MLT sectors (exception in the 04:00-

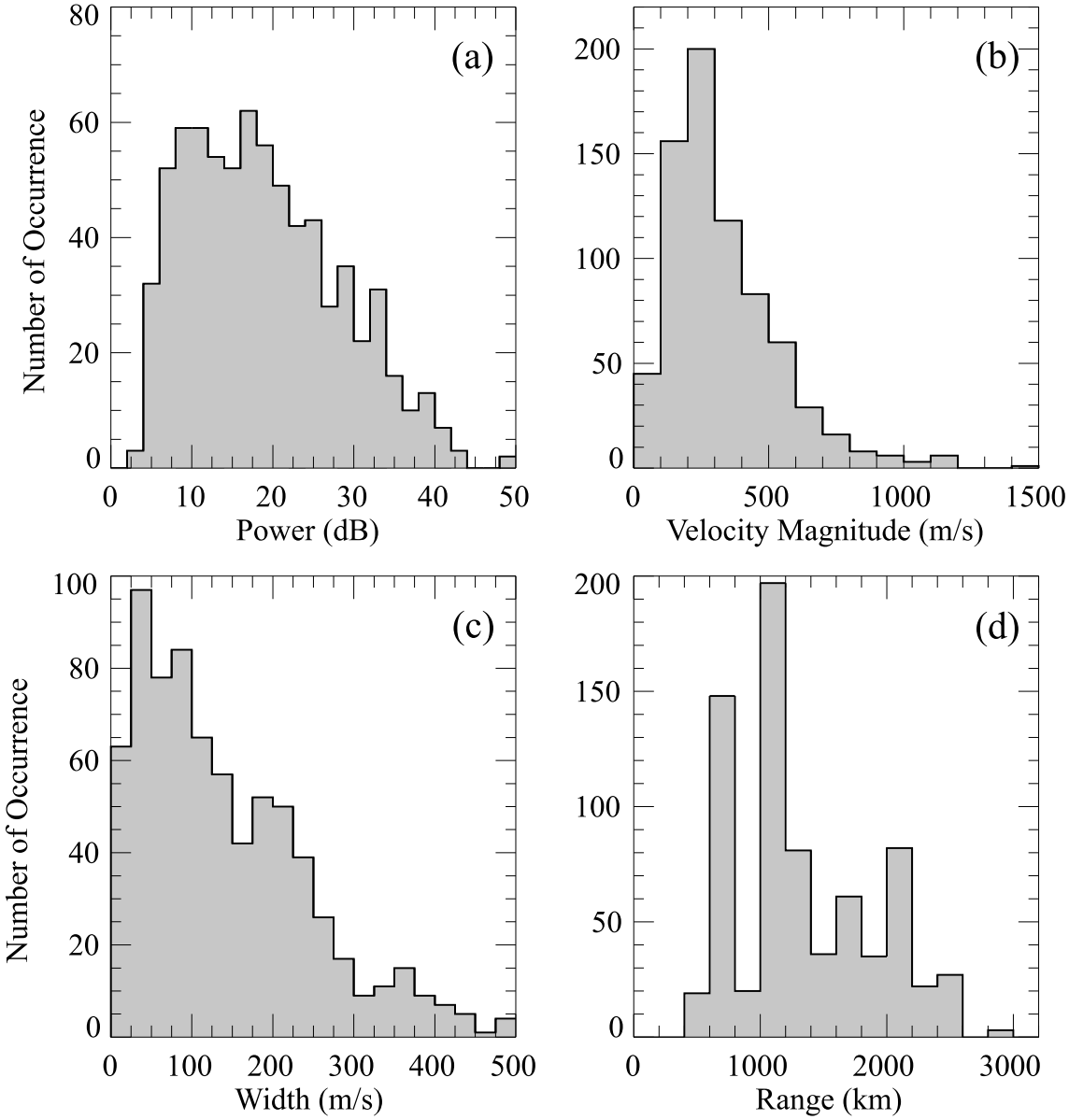

Figure 3.3: Histogram distributions of the SuperDARN radar (a) echo power, (b) velocity magnitude, (c) spectral width and (d) slant range for all events selected for comparison with DMSP.

08:00 MLT sector) and at magnetic latitudes of 64^0-83^0 in the Northern Hemisphere and 67^0-81^0 in the Southern Hemisphere, Figure 3.2. The average echo power was ∼19 dB S/N, Figure 3.3a. A velocity span of 0-1000 m/s was achieved with the mean velocity magnitude of ∼330 m/s, Figure 3.3b. The average spectral width was ∼140 m/s, Figure 3.3c, and echoes were observed between slant ranges of ∼400 km and 2600 km with an average slant range of 1330 km, Figure 3.3d. These values are typical for F region SuperDARN echoes (e.g., *Hamza et al.*, 2000; *Lacroix and Moorcroft*, 2001; *Villain et al.*, 2002; *Danskin*, 2003).

3.2.2 Line-of-sight comparison for the Stokkseyri radar

To show how the radar-satellite data compare for an individual radar, consider Stokkseyri-DMSP observations. Figure 3.4a shows a scatter plot of Stokkseyri l-o-s velocities versus DMSP cross-track ion drifts with their associated errors for 18 events and 53 points of comparison. The points are clustered around the bisector (dashed line) of perfect agreement. For two points, in the second quadrant, the velocity polarities are different. Similar points are present in other comparisons and likely correspond to localized areas with completely different plasma flows and are therefore not considered in the statistics presented in Figure 3.2 or Figure 3.3.

(a) Linear fitting

The SuperDARN and DMSP observations may be related by a linear approximation to determine the trend of the data. The linear relation is represented by

$$V_{SD} = mV_{DMSP} + b, \tag{3.1}$$

where V_{SD} is the SuperDARN l-o-s velocity, and V_{DMSP} is the DMSP cross-track ion drift. Equation (3.1) will be referred to as the best-fit line, where m and b represent the slope and y-intercept of the line, respectively.

We must first test the hypothesis that V_{SD} and V_{DMSP} can be represented by a linear approximation by examining the correlation coefficient between the data sets

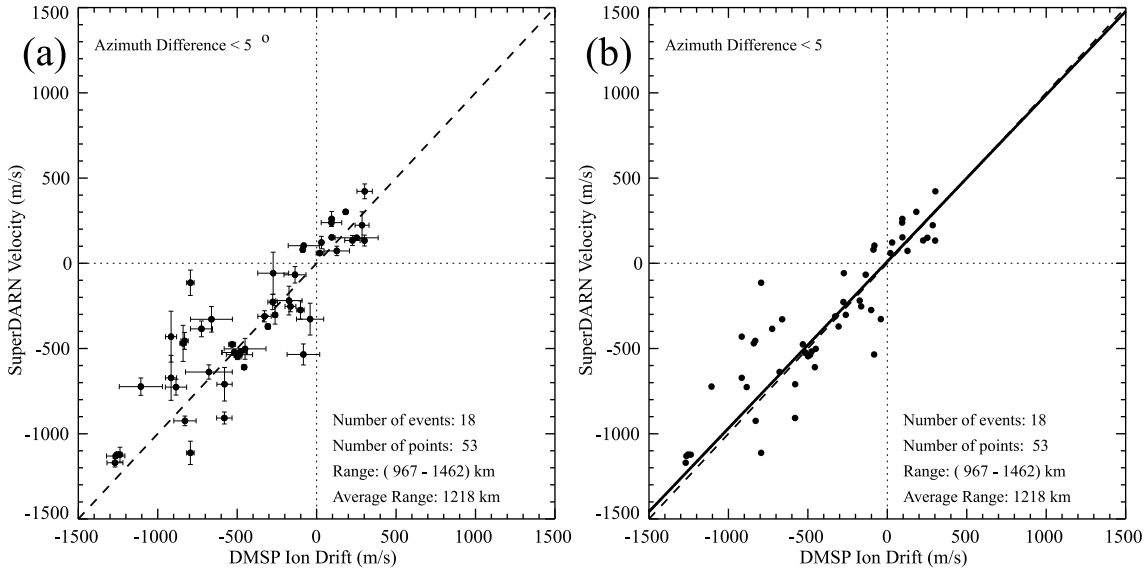

Figure 3.4: (a) A scatter plot of Stokkseyri l-o-s velocity versus DMSP cross-track ion drift with error for 18 joint events at radar ranges of ∼1000-1500 km. (b) The same as (a) without showing error for ease of viewing, and with the best-fit line overplotted.

and then considering the probability that a random data set could generate such a relationship. The correlation coefficient is given as follows (*Taylor*, 1997):

$$r = \frac{\sum_i (x_i - \bar{x})(y_i - \bar{y})}{\sqrt{\sum_i (x_i - \bar{x})^2 \sum_i (y_i - \bar{y})^2}}. \tag{3.2}$$

Here we will take x to be V_{DMSP}, and y to be V_{SD}. If all the points in our data set lie exactly on the line given by equation (3.1) then r will exactly equal +1 and V_{SD} and V_{DMSP} are completely correlated. However, if r=0, then V_{SD} and V_{DMSP} are completely uncorrelated. The next step is to determine how close to 1 the correlation coefficient must be to conclude the data are correlated. To accomplish this, we have to determine the probability that a random data set of the same size would have such an r-value.

For a data set of N points, the probability that a random data set would have an r-value greater than or equal to the calculated value r=r_o is given by (*Taylor*, 1997)

$$P_N(\mid r \mid \geq \mid r_o \mid) = \frac{2\Gamma[(N-1)/2]}{\sqrt{\pi}\,[\Gamma(N-2)/2]} \int_{|r_o|}^{1} \left(1 - r^2\right)^{\frac{N-4}{2}} dr, \tag{3.3}$$

where Γ is the gamma function given by (*Nagle et al.*, 2000)

$$\Gamma(t) = \int_0^\infty e^{-u} u^{t-1} du. \tag{3.4}$$

If the probability that a random data set has an equal or greater value than r_o is sufficiently small, then we consider it highly probable that the given data set is correlated. We will adopt the philosophy of *Taylor* (1997) and consider a 5% probability to indicate a significant correlation and a 1% probability to indicate a highly significant correlation.

For the Stokkseyri observations the correlation coefficient is r=0.90. The number of points is N=53, and the probability $P_N\,(\mid r \mid \geq 0.90)$ (according to equations (3.3) and (3.4)) is significantly less than 1%. Therefore, we can conclude that for the Stokkseyri comparison, it is reasonable to approximate the relationship between the SuperDARN l-o-s velocities and DMSP cross-track ion drifts with the line given by equation (3.1). Similar tests were performed for all other radars. Table 3.1 (see Section 3.2.3) lists the number of data points obtained for each radar, as well as for the entire data set. The last column indicates the calculated r-value for every radar comparison. For each set of points, $P_N\,(\mid r \mid \geq \mid r_o \mid)$ was calculated using equations (3.3) and (3.4) to be significantly less than 1%.

We may determine the constants m and b relating SuperDARN and DMSP measurements. The problem of determining m and b is solved using a least-squares fit. Let us denote each point of comparison by $(x_i\ ,\ y_i)$ where x refers to V_{DMSP} and y refers to V_{SD}. Each data point has uncertainty in both x and y, which can be denoted as $(\sigma_{xi},\ \sigma_{yi})$. Altogether, there are N data points, each having a different set of uncertainties. The determination of m and b is explained in Appendix A.

In this comparison, the value obtained for the slope of the best-fit line is meant to indicate the trend of the scattered data points. The exact value of the slope is useful in comparing the relative trend between data sets.

Figure 3.4b shows a scatter plot of the SuperDARN l-o-s velocities and DMSP cross-track ion drifts. In this diagram the error in the velocities have not been indicated for ease of viewing. The equation of the best-fit line is $V_{SD} = 0.98 V_{DMSP} +$

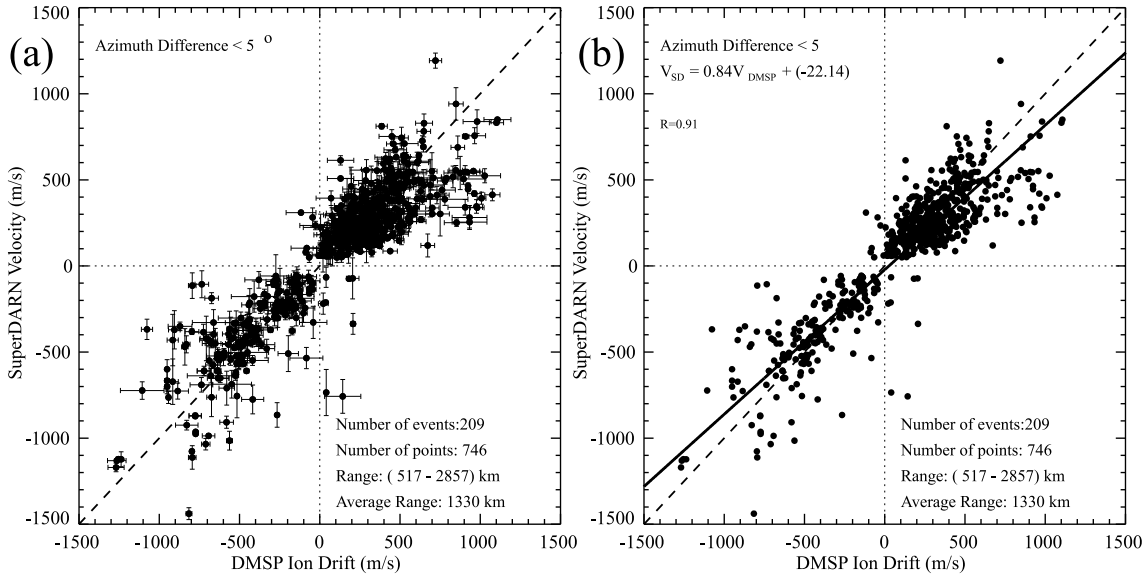

Figure 3.5: (a)The same as in Figure 3.4a, but for 9 radars: Hankasalmi, Pykkvibaer, Stokkseyri, Saskatoon, Kodiak, Halley, Sanae, Syowa-South, and Syowa-East and various radar ranges. (b) The same as (a) without showing error for ease of viewing, and with the best-fit line overplotted.

9.85 (m/s). The slope of the best-fit line (m=0.98) suggests excellent agreement between Stokkseyri l-o-s velocities and DMSP cross-track ion drifts.

3.2.3 Line-of-sight results for all considered radars

In Figure 3.5 we present statistics for all 9 radars by applying the same criteria as for the Stokkseyri comparison. Totals of 746 points in 209 events are available. Figure 3.5a is consistent with the Stokkseyri results in Figure 3.4a; there is reasonable agreement between measurements and the points are spread around the bisector. In Figure 3.5b, the heavy line indicates the best-fit line to the data set, and is given by $V_{SD} = 0.84V_{DMSP} - 22.14$ (m/s).

Other radars showed some variability in the slope of the best-fit line; Table 3.1 summarizes the findings. The radars are ordered from lowest to highest, according to average range. The best agreement with DMSP was found for the Stokkseyri radar. The worst agreement was found for the Halley radar, both in terms of the slope (m=0.39) and the correlation coefficient (r=0.53). Low slope of the best-fit

Table 3.1: Information on the number of events and points selected for the SuperDARN-DMSP comparison; typical ranges, slope, and correlation coefficient of the best-fit line to the data set.

Radar	Events	Points	Range(km)	m	r
Halley	32	168	517-742	0.39	0.53
Sanae	19	85	967-1147	0.52	0.79
Kodiak(Low)	20	62	832-1327	0.77	0.92
Syowa South	22	71	1012-1372	0.92	0.76
Stokkseyri	18	53	967-1462	0.98	0.90
Syowa East	21	87	967-2047	1.11	0.94
Pykkvibaer	21	64	1327-1957	0.63	0.88
Saskatoon	22	56	1732-2857	0.54	0.85
Hankasalmi	17	51	1672-2137	0.78	0.84
Kodiak (High)	17	49	1957-2542	0.88	0.83
All	209	746	517-2857	0.84	0.91

line was also found for the Sanae and Saskatoon radars. The comparisons for both Halley and Sanae were performed for relatively low ranges of <1200 km, whereas the Saskatoon comparison was performed at higher ranges. It is possible that ground scatter contaminates the data in both low and far ranges by direct hop propagation at low ranges and multiple hop propagation at far ranges (*Lacroix and Moorcroft*, 2001), despite our restriction of SuperDARN velocities <50 m/s to reduce ground scatter contamination. With the exception of Syowa East, each of the comparisons had slopes of <1, suggesting there is a tendency for SuperDARN l-o-s velocities to be less than DMSP cross-track ion drifts. For example, the average SuperDARN and DMSP velocities were 334 m/s and 380 m/s, respectively. This tendency seems to be more prominent for lower ranges and for larger DMSP velocities.

3.2.4 Range dependence

The range dependence on the agreement between SuperDARN and DMSP measurements is easily demonstrated for the Kodiak radar, which was assessed at two distinct range intervals. The Kodiak radar shows better agreement for high ranges of ∼2300 km with a slope of m=0.88 as compared to low ranges of ∼1100 km with a slope of m=0.77. An assessment of the dependency of the radar-satellite data agree-

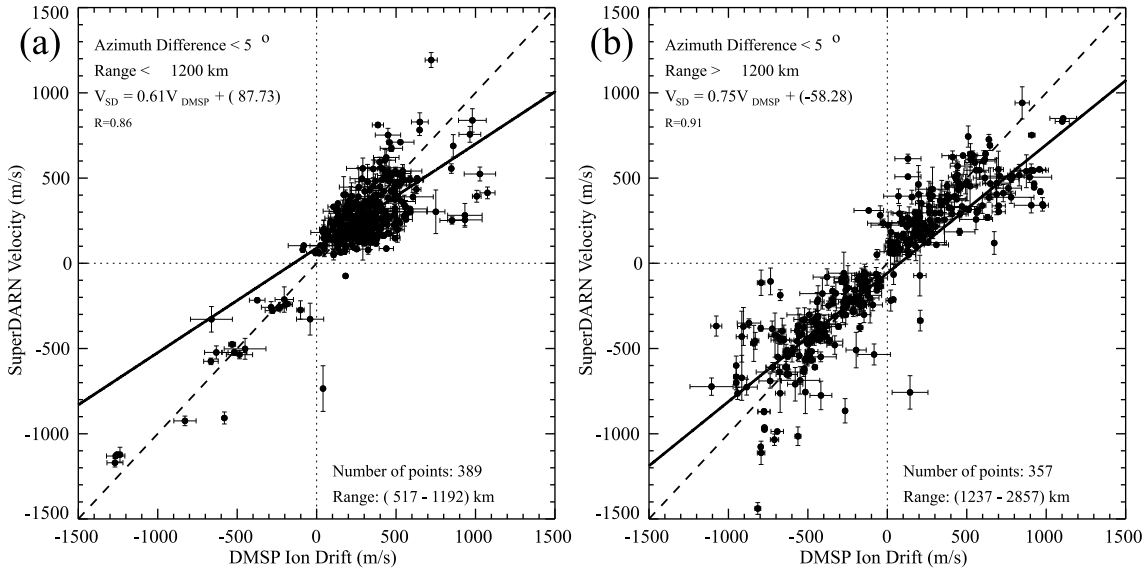

Figure 3.6: The same as in Figure 3.5 but for l-o-s velocities at a slant range of (a)< 1200 km, and (b)> 1200 km.

ment on range (for all SuperDARN radars involved) was performed by splitting the data set into observations for ranges <1200 km and >1200 km, see Figure 3.6a,b. The slopes of the best-fit lines are m=0.61 and m=0.75, respectively. The tendency for SuperDARN velocities to be less than DMSP ion drifts is more prominent for lower ranges. At large ranges, Figure 3.6b, the data are more evenly distributed within quadrants one and three both above and below the best-fit line. Range appears to play some role in the agreement of SuperDARN and DMSP observations.

3.3 Comparison of SuperDARN convection vectors with DMSP cross-track ion drifts

The result of the l-o-s comparison indicates good agreement between the data set at the raw data level. We now consider the effects of processing SuperDARN l-o-s velocities using the technique described in Section 2.1.2. We processed SuperDARN measurements using global convection mapping software (*Ruohoniemi and Baker*, 1998).

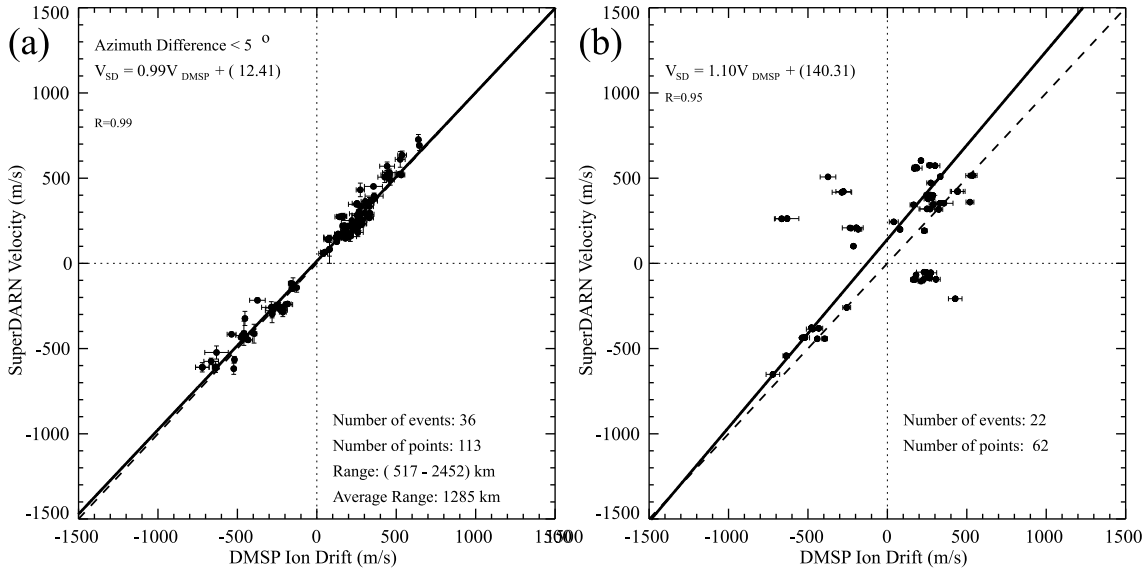

Figure 3.7: (a) A scatter plot of the most agreeable measurements of SuperDARN l-o-s velocity and DMSP cross-track ion drift from: Hankasalmi, Pykkvibaer, Saskatoon, Kodiak, Halley, Sanae, Syowa-South and Syowa-East. (b) Scatter plot of projected SuperDARN convection velocity versus DMSP cross-track ion drift for the events considered in (a).

3.3.1 Approach to the convection comparison

Thirty-six ideal DMSP passes were chosen from the 209 events in the l-o-s comparison data set and compared against SuperDARN convection. Passes were chosen from those events showing good correspondence between SuperDARN l-o-s velocities and DMSP cross-track ion drifts. The scatter plot of data for these events is shown in Figure 3.7a. There are a total of 113 points of comparison. The events were chosen from various radars in both the Northern and Southern Hemispheres with slant range varying between 500 and 2500 km. The slope of the best-fit line for the ideal events is m=0.99 and the correlation coefficient is r=0.99. The average SuperDARN and DMSP velocities are 270 m/s and 250 m/s, respectively. The average power was 17 dB and the typical spectral width was 80 m/s. These selected events are representative of F region SuperDARN echoes and are typical of the data set.

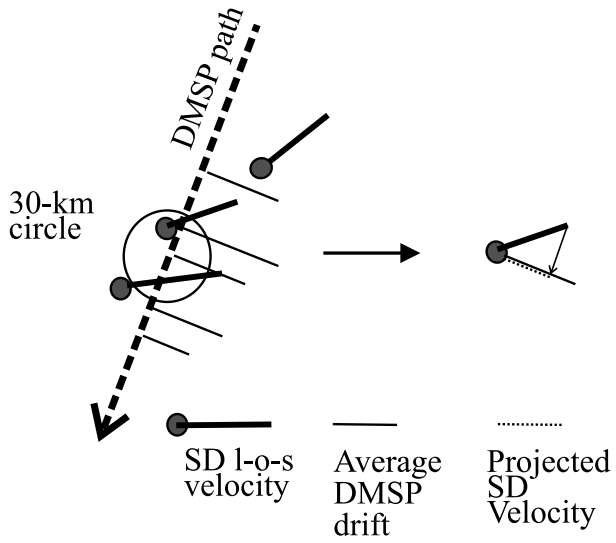

Figure 3.8: A scheme illustrating the velocity comparison between SuperDARN (SD) convection velocities and DMSP cross-track ion drifts.

The following procedure was used to compare the DMSP cross-track ion drifts with the full SuperDARN convection vectors. First a two-minute convection map was generated using observations from multiple radars. The averaged DMSP cross-track ion drifts and their corresponding standard deviations from the original l-o-s comparison were identified. The SuperDARN convection velocity vector closest to each DMSP vector within a 30-km radius was located. Typically, the closest SuperDARN vector was within 10 km of the DMSP vector. The SuperDARN convection vector was then projected onto the DMSP cross-track ion drift, Figure 3.8. To be consistent with the previous comparison, projected SuperDARN convection velocities less than 50 m/s were discarded. This procedure allowed us to compare the same DMSP cross-track ion drifts used in the l-o-s comparison to nearby SuperDARN convection vectors.

3.3.2 SuperDARN vector comparison for all radars

Figure 3.7b indicates the results of the comparison between DMSP cross-track ion drifts and SuperDARN convection vectors obtained by fitting the l-o-s velocities of multiple radars. There are 22 events and 62 points of comparison. The considerable reduction of data points is due to the exclusion of low velocity convection data.

The best-fit line has a slope of m=1.10 and the correlation coefficient is r=0.95. In comparison with the original data set, Figure 3.7a, the observations are more widespread and do not cluster about the line of ideal correspondence. In general, the projected SuperDARN l-o-s velocities become larger in quadrant 1 and smaller in quadrant 3 when they were processed. In addition, there are 22 points located in quadrants 2 and 4 indicating a difference in polarity between the SuperDARN and DMSP velocities. Such points were not present in the l-o-s comparison shown in Figure 3.7a, suggesting the SuperDARN reprocessing software reversed the direction of the plasma flow for some observations. This result implies that although processing SuperDARN l-o-s velocities to produce global convection patterns is useful, care should be taken when small-scale processes are being studied within the patterns.

3.4 Discussion

The SuperDARN/DMSP velocity comparisons presented in this study show, on a statistical basis, that in spite of the different methods of plasma flow measurements, in space and from the ground, the velocities are fairly consistent. The comparison performed in this study included various radars of the SuperDARN network; the radars use the same principles of measurement, but their hardware and on site observational conditions vary. The comparison was also performed for various radar ranges so that all possible modes of radio wave propagation were considered. Significant coverage of magnetic latitudes and magnetic local time sectors was achieved. All the above means that the DMSP and SuperDARN l-o-s velocities can be merged into one data set provided both instruments show reasonably smooth spatial and temporal variations.

When SuperDARN l-o-s velocities were processed into convection vectors and compared with corresponding DMSP ion drifts there was a deterioration of agreement between the data. This finding suggests the current standardized method of processing SuperDARN l-o-s velocities into a smooth convection pattern introduces some errors.

In the l-o-s velocity comparison we noticed a minor tendency for the SuperDARN l-o-s velocities to be smaller than the DMSP ion drifts. Similar conclusions were drawn from a comparison of SuperDARN data with incoherent scatter radar (*Xu et al.*, 2001) and CADI ionosonde (*Xu*, 2003) measurements. We now discuss potential reasons for this effect.

3.4.1 Effect of spatial and temporal variability of convection

The data spread in Figure 3.5 can be explained by the different spatial and temporal resolutions of the instruments. One would not expect a perfect match of the DMSP and radar measurements in terms of space. The DMSP satellite sampled every $\sim$ 7.5 km/s $\times$ 4 s=30 km while the size of a radar cell at a range of $\sim$1440 km from the radar,which is the average slant range for the l-o-s velocities considered in this comparison, is $\sim$45$\times$80 km.

Figure 3.9 shows two examples of joint radar-satellite measurements to illustrate the importance of the spatial variability of convection on radar and satellite observations. Here individual Stokkseyri l-o-s velocities (colored boxes with the color scheme presented to the right of Figure 3.9b) measured at various cells are plotted in geographic coordinates. A DMSP pass by satellite F13 is overplotted and black lines indicate the cross-track ion drifts. The time shown in each diagram indicates the beginning of the two-minute period of the SuperDARN scan. In both examples, the DMSP satellite crosses the radar's field of view at the approximate time of the scan. At 11:02 UT on December 12, 1999 the Doppler velocity varies relatively smoothly in the area of comparison, Figure 3.9a. The comparison plot shows agreement between velocity measurements as the points around the bisector of ideal agreement (dashed line), Figure 3.9c. For the event of February 8, 2000 at 10:40 UT, the velocity map is more variable, Figure 3.9b. Figure 3.9d indicates that the velocities measured by the radar and satellite are not as consistent; two points are in good agreement, two other points lie below the bisector and the last three points are located above the bisector. Clearly, small-scale spatial convection inhomogeneity can account for velocity discrepancies for some events.

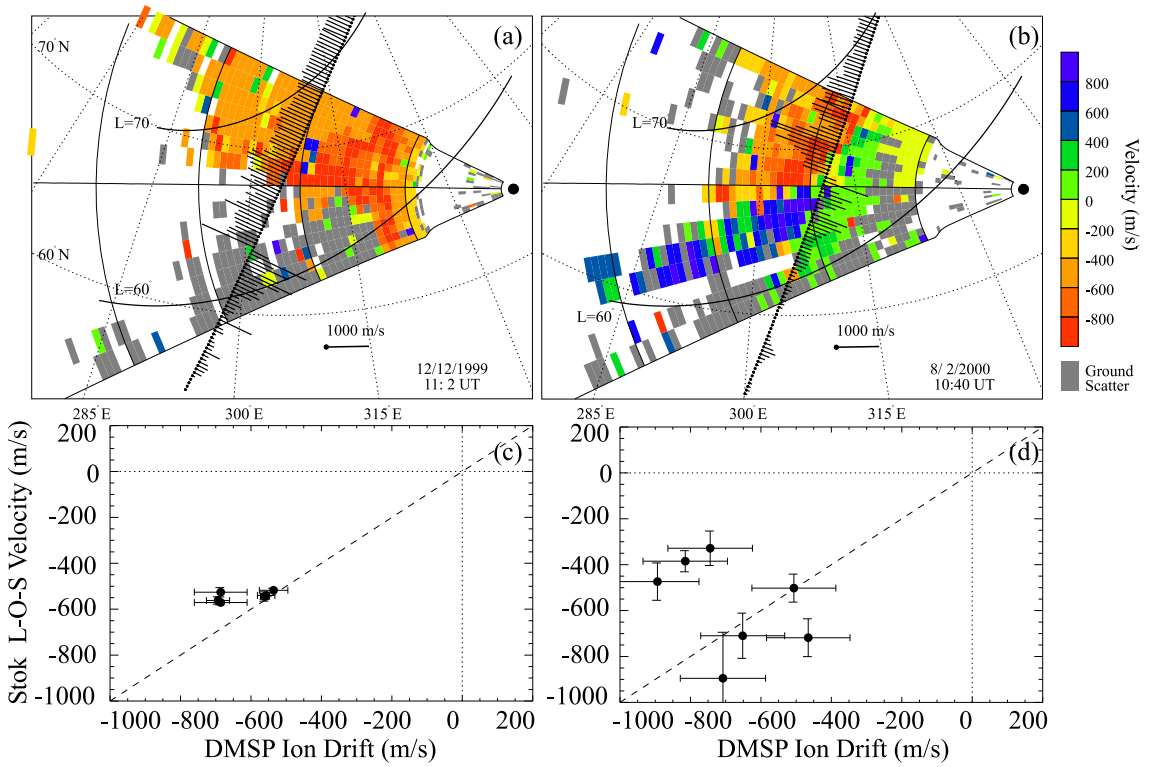

Figure 3.9: Two examples of a SuperDARN/DMSP velocity comparison. (a) A Stokkseyri l-o-s velocity map for 11:02 UT with over-plotted DMSP cross-track ion drifts for an event on December 12, 1999. (c) A scatter plot of the radar velocity versus the ion drift for the radar cells in panel (a) with the difference between the radar and satellite directions at less than 5^0 and the difference in time at less than 2 min. Panels (b) and (d) show the same, but for an event on February 8, 2002.

To illustrate the importance of the flow stability in terms of time, we present observations at Syowa East, on March 4, 2001, Figure 3.10. Figure 3.10a shows the l-o-s velocity map for a scan at 17:48 UT over-plotted with DMSP velocity vectors. This scan was 4 min earlier than the scan for which the comparison with the DMSP data was performed at 17:52 UT. The DMSP ion drifts were plotted on this panel and have been omitted in panels (b) and (c) for the convenience of viewing. Figure 3.10b and 3.10c show the Sanae data for scans at 17:52 and 17:54 UT. Notice that in the area of comparison the l-o-s velocities are >600 m/s at 17:48 UT, between 200 and 600 m/s at 17:52 UT, and at 200-600 m/s at 17:54 UT. There is a significant temporal variation in the velocity. Since the time difference between the radar and satellite measurements was to the order of 120 seconds and the actual comparison was

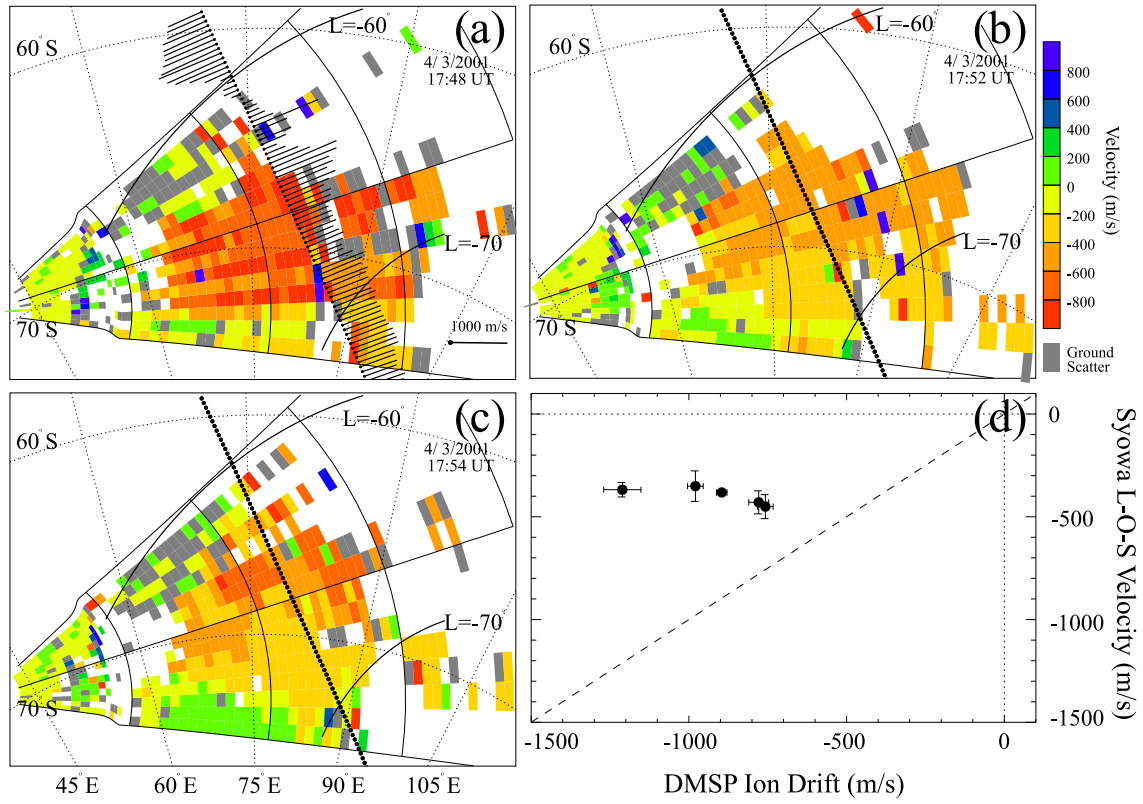

Figure 3.10: Syowa-East l-o-s velocity maps for (a) 17:48 UT, (b) 17:52 UT and (c) 17:54 UT and the DMSP cross-track ion drift observed between 17:49 UT and 17:53 UT for an event on March 4, 2001. Panel (d) is a scatter plot of the radar velocity versus DMSP ion drift for the points in panel (b) with the difference between the radar and satellite directions of less than 5^0 and the difference in time of less than 2 min.

taken at 17:52 UT, one would expect lower radar velocity than the DMSP velocities. The poor agreement of the radar and satellite data shown in Figure 3.10d is not a surprise.

3.4.2 Instrumental effects

It is possible that measurement discrepancies arise due to the quality of the observations. For some measurements, the quality of DMSP data was questionable, as the data quality flag changed along the path. It is possible that disagreement between DMSP ion drifts and SuperDARN l-o-s and convection velocities may be due to the use of DMSP data points having undetermined quality tags. For the

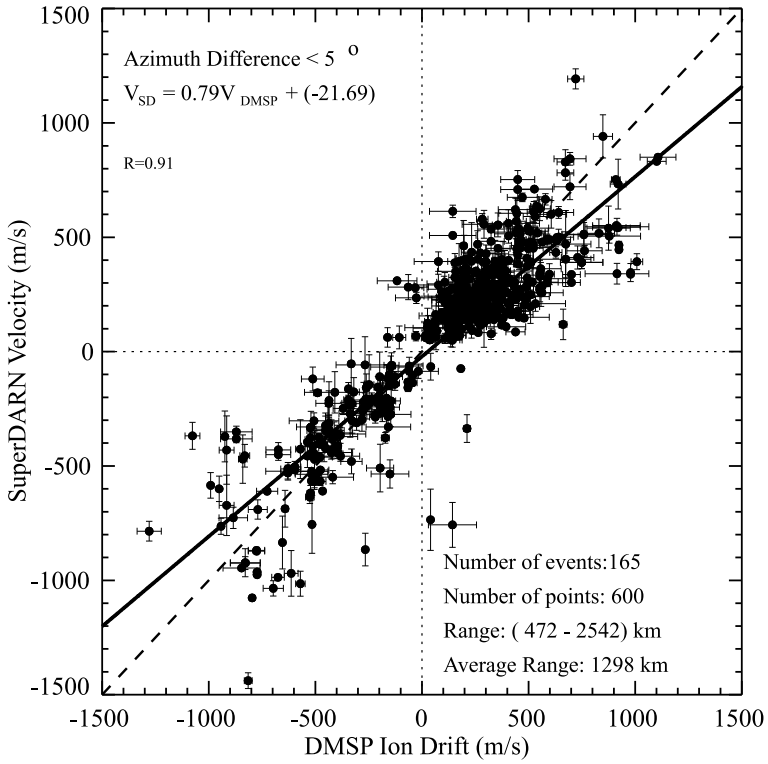

Figure 3.11: The same as in Figure 3.5 but for quality 1 (measurement is reliable) DMSP measurements.

purpose of both the l-o-s comparison and the convection vector comparisons, DMSP points with undetermined quality tags were used to create averaged DMSP cross-track ion drifts to ensure a larger data set provided the DMSP pass was smooth in the area of comparison. To test the effect of the undetermined-quality DMSP points, a second l-o-s comparison was performed which only included those DMSP points having a quality tag of 1 (measurement is reliable). Applying more stringent requirements on the data quality decreased the DMSP data set, so the search area was increased from 45 km to 55 km if fewer than two DMSP points were initially identified. The DMSP vectors were averaged together to obtain the DMSP ion drift, and the standard deviation was taken as its error. Only ion drifts having a standard deviation less than 150 m/s were considered in the comparison.

Figure 3.11 plots the results of the l-o-s comparison when only quality 1 DMSP points were considered. The best-fit line through the data set is given by $V_{SD} = 0.79V_{DMSP} - 21.69$ (m/s) and the correlation coefficient is r=0.91. The data spread

Table 3.2: Percent change of number of events and points, and the slope of the best-fit line for the SuperDARN-DMSP comparison using quality 1 DMSP measurements.

Radar	Events	ΔEvents (%)	Points	ΔPoints (%)	m	Δm (%)
Halley	26	-19	155	-8	0.31	-21
Sanae	14	-26	62	-27	0.59	13
Kodiak(Low)	20	0	55	-11	0.70	-9
Syowa South	18	-18	65	-8	1.03	12
Stokkseyri	10	-44	31	-42	1.12	14
Syowa East	17	-19	70	-20	1.10	-1
Pykkvibaer	16	-24	41	-36	0.46	-27
Saskatoon	18	-18	47	-16	0.52	-4
Hankasalmi	12	-29	31	-39	0.91	17
Kodiak (High)	14	-18	43	-12	0.88	0
All	165	-21	600	-20	0.79	-6

and slope of the best-fit line is very similar to the original comparison presented in Figure 3.5. However, the data set is significantly reduced to 165 events and 600 points. The velocity spread is not affected. Table 3.2 indicates the statistics for each radar's l-o-s comparison against DMSP points having a quality tag of one, and how they changed from the values reported in Table 3.1. The slope of the individual graphs became both closer to, and further from the ideal value of one. There is a significant change of >20% in the slope for Halley and Pykkvibaer, suggesting the statistics for these radars were largely dependent on undetermined quality DMSP points. The agreement became worse for these two radars. Importantly, removing undetermined quality points caused a slight decrease of 6% in the slope from the original graph of all radars, suggesting the presence of undetermined quality data points increased the agreement between SuperDARN and DMSP. In general, the correlation coefficient r did not change significantly, meaning the clustering of points was not highly dependent on questionable DMSP points.

One factor that might be important in understanding the larger SuperDARN-DMSP differences at high DMSP drifts is the degree of the azimuthal difference between the radar and satellite directions of measurements. This is especially important for observations at large angles with respect to the flow, which is typical for

many radars. Perhaps, this notion can be supported by deterioration of the radar-satellite data agreement at larger radar ranges of the comparison. We reported, the data clustering was r=0.86 at ranges <1200 and r=0.91 at range >1200 km. This is generally expected since the radar localization of the echoing region deteriorates at large ranges, especially when the one and a half propagation mode is involved (*Yeoman et al.*, 2000). Such deterioration of range would mean DMSP ion drifts might have been compared to SuperDARN velocities originating from different locations. We eliminated events from our data set that did not show similar convection trends between the radar l-o-s velocities and satellite ion drifts to help reduce this contamination.

To explore the effect further, we attempted to relax the 5^0 misalignment requirement. The results were very similar to those presented in Figures 3.2, 3.3, and 3.5 except the data spread was more significant. For example, for a 10^0 misalignment the number of points of comparison doubles and the line of best linear fit is $V_{SD} = 0.80V_{DMSP} - 9.83$ (m/s). We should note that the error in the alignment could be either positive or negative so that one would not expect a trend of smaller SuperDARN l-o-s velocity as compared to the DMSP ion drift, unless the statistics are too small. We feel that our statistics are large enough and that the observed trends do not originate from errors in the direction calculations.

3.4.3 E region contamination and ground scatter contamination

The good agreement between DMSP ion drifts and SuperDARN F region velocities strongly contrasts with the disagreement of ion drifts and SuperDARN E region velocities (*Koustov et al.*, 2005a). In *Koustov et al.* (2005a) a similar scatterplot comparison was performed between Stokkseyri l-o-s velocities in the E region and DMSP cross-track ion drifts (see their Figure 4) and a slope of m=0.24 was obtained. For the F region comparison performed in this thesis (Figure 3.4b), the slope was m=0.98. For the E region echoes, low velocities were expected from pre-

vious VHF observations since the electrojet irregularities may travel with a velocity significantly different from the cosine component of the $\mathbf{E}\times\mathbf{B}$ drift (e.g., *Nielsen and Schlegel*, 1985). For example, the irregularity velocity along the flow is close to the ion-acoustic speed.

Milan et al. (1997) found signatures of E region contamination at far ranges for the Pykkvibaer radar in the form of a clustering of points at low spectral widths (<200 m/s) and ion-acoustic speeds (see their Figure 10). There is a similar clustering of SuperDARN velocities with spectral widths <200 m/s at l-o-s velocities of 300-400 m/s for the Pykkvibaer radar in this study, which may explain the low slope of m=0.63 reported in Table 3.2.3. However, with such a low data set (64 points), it is not clear if this clustering is significant. *Lacroix and Moorcroft* (2001) performed a statistical study of the Pykkvibaer radar for F region echoes (range>1755 km) and found a similar contamination of E region or ion acoustic echoes propagated through F-E/ or FE/ modes.

One way to asses the significance of E region contamination is to only consider those SuperDARN observations for which the velocity was more than 500 m/s, and therefore not saturated. Such a diagram is presented in Figure 3.12a. In this case the slope of the best-fit line is closer to m=1. This suggests that E region contamination influences the comparison as the agreement is better for large SuperDARN velocities.

Another way to assess the importance of E region contamination is to consider observations where the DMSP cross-track ion drift is >500 m/s to observe the distribution of the SuperDARN l-o-s velocities, Figure 3.12b. We see that a number of points correspond with a SuperDARN velocity close to 400 m/s, which is the nominal ion-acoustic velocity. This diagram also suggests that some points in Figure 3.5 may correspond to E region echoes, rather than F region echoes, as assumed. Further investigation of this effect has been left for future studies, and is currently being investigated by other researchers (*St-Maurice et al.*, 2006).

Another possible cause for the discrepancy is the contamination of SuperDARN ionospheric echoes with ground scattered signals. This effect cannot be identified by looking at the FITACF data used in this study; a completely new approach with

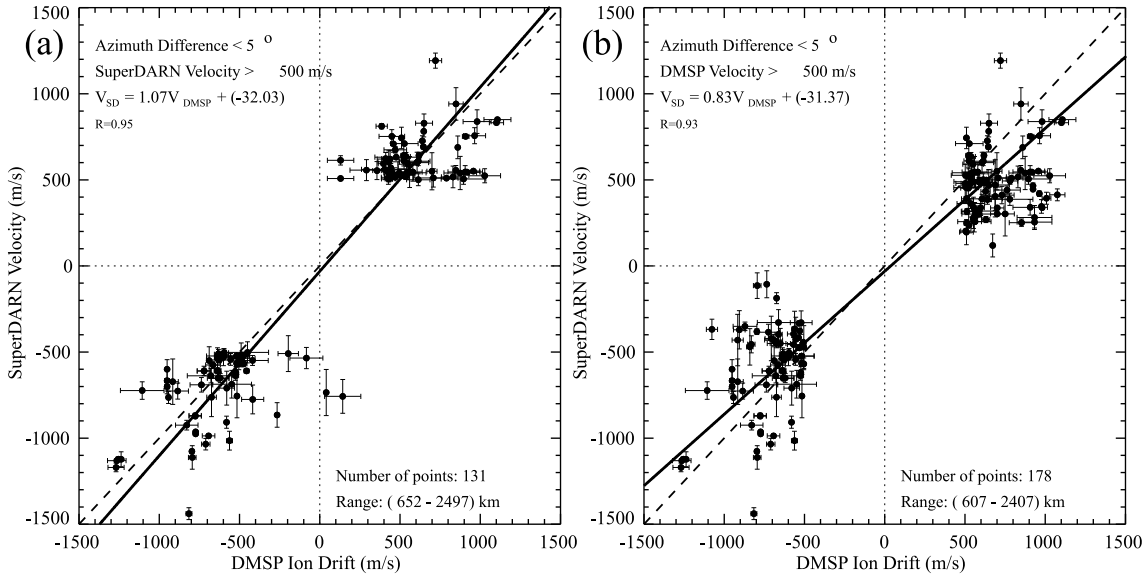

Figure 3.12: The same as in Figure 3.5 but for SuperDARN velocities (a) > 500 m/s, and (b) DMSP velocities > 500 m/s.

data processing of the full spectra is required which is beyond the scope of the present study. We can report that for some events, the SuperDARN autocorrelation functions were not of great quality (for quality of the auto-correlation function see *Villain et al.* (1987)). For several other events, a strong ground scatter component was found; this could have affected the l-o-s velocity.

3.5 Conclusions

In this Chapter we showed that for more than 200 DMSP passes over nine SuperDARN radars' field of view the DMSP cross-track ion drift agrees reasonably well with the line-of-sight velocity of the F region SuperDARN echoes. The slope of the best-fit line relating the SuperDARN and DMSP velocities was of the order of 0.8 with a tendency for SuperDARN velocities to be smaller. More than 30 DMSP passes showing near perfect agreement with SuperDARN l-o-s velocities were compared to SuperDARN convection maps made using multiple radars. The slope of the best-fit line relating the SuperDARN l-o-s and DMSP velocities for these events was 0.99. The slope of this line increased to 1.10 when the SuperDARN l-o-s velocities were processed into convection velocities. The data set was more widespread with sev-

eral points of opposite polarity. The l-o-s comparison was performed for conditions with smooth temporal and spatial variations on the plasma flow according to both instruments; for strong variations, more significant differences were sometimes observed. The results imply that the DMSP ion drift velocities with relatively smooth profiles over the satellite trajectory can be merged with concurrent SuperDARN F region velocities to produce a joint convection map. In addition, SuperDARN F region velocities are comparable with ion drifts independently measured by DMSP, for up to 1500 m/s. Our observations suggest SuperDARN is a reliable instrument of observation. We will now focus our attention on the King Salmon radar.

Chapter 4

Nature of dusk-side SAPS-like flows observed by the King Salmon radar

Recent interest in various mid-latitude phenomena and the coupling of the high- and mid-latitude ionospheres has instigated an investigation of the SuperDARN radar capabilities in studying these processes. Earlier efforts report HF echo occurrence near the sunset and sunrise solar terminator line (*Ruohoniemi et al.*, 1988; *Hosokawa et al.*, 2001). Such echoes occur near the equatorial edge of the oval in the early-dusk and late-dawn sectors. In a series of papers, SuperDARN E region echoes are shown to trace the equatorial edge of proton precipitation located equatorward of the auroral oval in the midnight sector (e.g., *Jayachandran et al.*, 2002). In the past few years, significant interest has been shown in the detection of fast plasma flows at subauroral latitudes. Such flows are categorized as SAPS (see Section 1.7.2). The SuperDARN radars were originally designed to monitor plasma flows in the auroral zone and polar cap areas, at 65^0 to 85^0 MLat. To monitor echoes from the subauroral ionosphere, a series of new mid-latitude radars has been proposed (Section 2.1). Some of these radars have begun operation since the completion of this thesis (*Greenwald et al.*, 2006). In this Chapter we attempt to assess whether existing radars (as of summer 2004) are useful in studying SAPS. We consider observations from the King Salmon SuperDARN radar in Alaska. Materials presented in this Chapter were published in *Koustov et al.* (2006).

4.1 Previous fast-flow studies with SuperDARN

Parkinson et al. (2003, 2005, 2006) were the first authors who used SuperDARN to monitor high-velocity flows near, or even equatorward of, the auroral oval in the late-dusk sector. They realized the TIGER radar in Bruny Island, Tasmania and the King Salmon radar in Alaska are very useful because both are capable of viewing as far equatorward as $\sim 60^0$ MLat.

Parkinson et al. (2003, 2006) concentrated on Bruny Island radar observations and discovered that high-velocity streams of westward flowing plasma are common in the dusk sector. These authors described the flows as auroral westward flow channels (AWFCs), perhaps to distinguish them from SAPS. *Parkinson et al.* (2005) presented joint Bruny Island radar and IMAGE satellite luminosity data (mapped from the Northern Hemisphere) to show AWFCs can be located close to the equatorial edge of the auroral oval. The authors claimed the AWFCs overlap the equatorward edge of the auroral oval and hypothesized that the observed flows can be classified as SAPS (the authors actually used the term "polarization jet", as the concept of SAPS was only introduced in 2002). *Parkinson et al.* (2006) examined one year of Bruny Island radar data for the most L-shell aligned beam 15 (the L-shell angle is about 50^0) and identified AWFC events by locating all westward velocity streams that were large (> 450 m/s) compared to the background flow. They observed AWFCs ~ 150 days of the year and suggested that increased radar coverage would raise this to at least one AWFC every night. Parameters of AWFCs were reported as follows (*Parkinson et al.*, 2003). The duration of the flow is $\sim$70 min with individual streams confined to zonal channels of longitudinal extent $> 20^0$ at a geomagnetic latitude of -65^0 and latitudinal widths of $\sim 2^0 - 3^0$. The maximum velocities are of the order of 1.5 km/s, as inferred from l-o-s velocities scaled up assuming the flow is L-shell aligned.

Another important aspect of AWFCs is their close relationship with substorm occurrences near the radar field of view. For the Bruny Island radar observations, the Macquarie Island (MQI) magnetometer in the Southern Hemisphere, SAMNET magnetometer array (located in the Northern Hemisphere, UK), and Canadian mag-

netometer chains (also in the Northern Hemisphere) were used to identify the onset, and checks are made against LANL satellite observations of energetic particle fluxes. Unfortunately, the MQI magnetometer is the only one close to the Bruny Island radar field of view. All three papers insist that each identified AWFC occurred in association with a substorm. The flow enhancements generally started at substorm onset and decayed near the end of the substorm recovery phase (*Parkinson et al.* 2003, 2005). This is an important distinction of AWFCs from SAPS as the latter are generally observed at some delay from substorm onset, during the substorm recovery phase (*Anderson et al.*, 1993; *Karlsson et al.*, 1998; *Galperin*, 2002).

Parkinson et al. (2005) presented two examples of Bruny Island radar observations of AWFCs and simultaneous data collected by the King Salmon radar in the Northern Hemisphere. King Salmon and Bruny Island have several almost magnetically conjugate beams. For example, beam 14 of Bruny Island corresponds to beam 2 of King Salmon. During one event, November 30, 2002, AWFCs were concurrently observed by both radars. The flow velocities reached $\sim$ 800 m/s approximately 40 min after the substorm onset, near the peak of the expansion phase and decayed by the end of the recovery phase. The general trend of the maximum velocity agreed between radars throughout the event, but the magnitudes were quite different; Bruny Island observed velocities $\sim$ 1.5 larger (see their Fig. 9).

The problem with the studies by *Parkinson et al.* (2003, 2005, 2006) is that the high velocities reported were in fact estimated velocities made under the assumption that flows near the equatorward edge of the auroral oval are L-shell aligned. The geometry of Bruny Island observations is such that beam 4 is oriented almost perpendicular to the magnetic L-shells and the radar boresight is poleward-oriented. In this respect, it is interesting to note that *Ridley and Liemohn* (2002) predicted a departure of SAPS flows from L-shell directions, especially in the 18:00-20:00 MLT sector, where the flow was found to bend away from the L-shell direction by as much as 60^0 and be more poleward-oriented (see their Figure 6).

4.2 Importance of the King Salmon radar within SuperDARN; radar location and field of view

To understand the importance of the King Salmon radar for SAPS studies, we must consider the fields of view of the Northern Hemisphere SuperDARN radars, Figure 2.1. Several radars, such as Hankasalmi, Prince George, Kodiak, and King Salmon, are located at magnetic latitudes low enough to view the sub-auroral region at $\sim 60^0$ MLat. However, with the exception of King Salmon, these radars only observe sub-auroral latitudes at low ranges. The problem with low range observations is that the echoes often originate from the E region where velocity magnitudes are significantly less than F region convection velocities and tend to saturate at the E region ion-acoustic speed (e.g., *Koustov et al.*, 2005a). The King Salmon radar has geomagnetic coordinates of $\sim 57^0$ N and $\sim 100^0$ E, a boresight direction of -20^0, and can monitor high range F region echoes from as low as 60^0 MLat in its lowest beams over a large range of magnetic longitudes. This is possible because beams 0-5 for King Salmon have L-shell angles of $10^0 - 20^0$ (approximately L-shell aligned) which is close to the expected orientation of SAPS flows (*Foster and Vo*, 2002). Two other radars, Stokkseyri and Pykkvibaer, have a similar azimuthal orientation of their beams, but cover $\sim 5^0$ higher latitudes where the detection of SAPS flow is not likely. *Foster and Vo* (2002) reported typical SAPS latitudes to be $< 65^0$ MLat, and the Stokkseyri and Pykkvibaer radars only observe poleward of 65^0 MLat. Therefore, because of its position and orientation, the King Salmon radar is the most useful Northern Hemisphere radar for observing plasma flow in the sub-auroral region.

4.3 General characteristics of King Salmon F region echoes

We begin with a general characterization of King Salmon radar observations. We note that despite having been operational for several years, this is the first con-

centrated effort to assess the radar's performance. We start by considering monthly averages of routine data gathered in the standard mode of operation. We examine echo occurrence rate, power, velocity, and spectral width for various months of observations.

Data were only considered for ionospheric echoes stronger than 3 dB having spectral widths < 500 m/s and velocities > 50 m/s to eliminate untypical echoes and reduce ground scatter contamination. Data were averaged over 10 minutes of observations in bins of 1^0 of magnetic latitude. Magnetic local time was computed by taking into account magnetic longitude and universal time in the echoing region. All available data since the radar began operation at the end of 2001 until the end of 2004 were processed.

4.3.1 Solar cycle and seasonal effects in the King Salmon echo occurrence rates

Typical measured echo occurrence rates are shown in Figure 4.1 in MLT-MLat coordinates for winter conditions, for December of (a) 2001, (b) 2002, (c) 2003, and (d) 2004. The auroral oval location predicted by *Feldstein and Starkov* (1967) for Kp=2, which is the average Kp for December 2001, is overplotted on the first diagram for reference. Occurrence rates were computed as the ratio of the number of ionospheric echoes in an individual radar gate to the total number of observations in that gate over approximately 20 full-day observations each month. The total number of scans was 23400 over 17 days in 2001, 14322 over 21 days in 2002, 29734 over 30 days in 2003, and 11824 over 16 days in 2004. The largest occurrence rates of up to 30% are for December 2001 on the nightside between 65^0 and 70^0 MLat centered about midnight between 18:00 and 05:00 MLT. The occurrence rate in the same region drops down to 10-20% in 2002, and to less than 7% in 2003 and 2004. In 2002 a region of little to no echo occurrence develops in the high latitude dusk region, expands to lower latitudes in 2003, and spreads into the morning and afternoon sectors in 2004. These observations show that with the decrease of solar activity

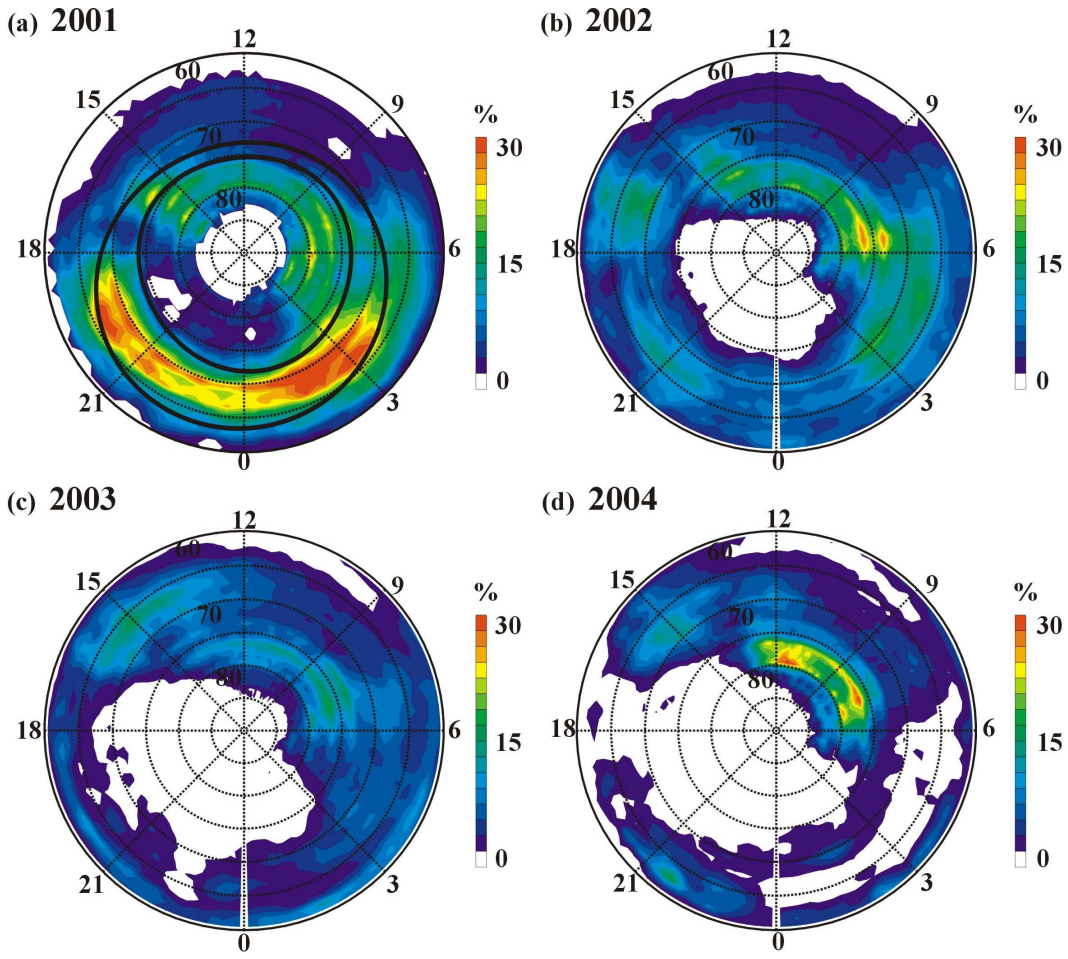

Figure 4.1: King Salmon echo occurrence rate for December (a) 2001, (b) 2002, (c) 2003, and (d) 2004 in magnetic latitude-magnetic local time coordinates.

from 2001 to 2004 (within the 11-year solar cycle), the occurrence rates go down as reported by *Ruohoniemi and Greenwald* (1997) and *Koustov et al.* (2004). For 2004, echoes are more frequently observed in the pre-noon sector at large magnetic latitudes of $\sim 71^0 - 75^0$ MLat. Overall, the echo occurrence rates for each year are somewhat smaller than for other SuperDARN radars. For example, *Koustov et al.* (2004) reported an occurrence rate of $\sim 50\%$ for the Saskatoon radar at $\sim 70^0$ MLat in the midnight sector for December 2001.

To examine the seasonal effects of echo occurrence rate we consider observations for winter (December 2001), equinox (March 2002) and summer (July 2003), Figure 4.2 a-c. The observations are spread out over three years and are subject to solar cycle effects. However, the seasonal effects discussed below occur in addition to solar

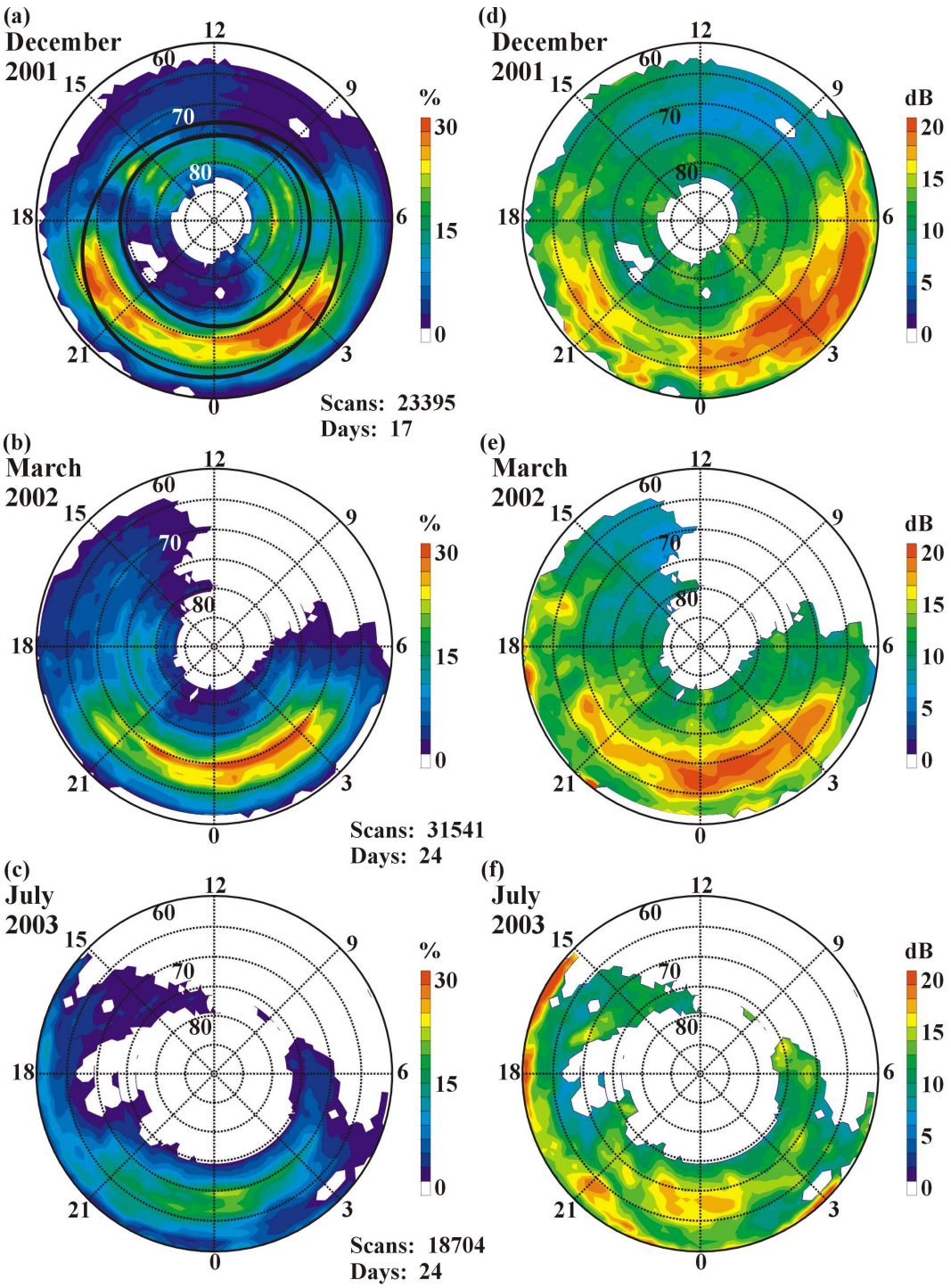

Figure 4.2: King Salmon echo occurrence rate and averaged power for winter (December 2001, panels (a) and (d)), equinox (March 2002, panels (b) and (e)), and summer (July 2003, panels (c) and (f)) in magnetic latitude-magnetic local time coordinates.

cycle effects, and the months chosen for discussion are representative of the seasonal effects observed in the entire data set. The total numbers of scans were 23395 over 17 days in December, 31693 over 24 days in March, and 18809 over 24 days in July. The number of scans for each month is significant. It is important to realize these statistics are considerably larger than those considered by other researchers. For example, *Foster and Vo* (2002) had data for $\sim$ 9800 azimuthal scans in their statistical study of SAPS using the Millstone Hill incoherent scatter radar.

According to Figures 4.2a-c, echoes are more frequent in the nightside sector and during winter, with peaks of up to 30%. Minimum occurrence rates are observed on the dayside near noon. In all three plots there is an enhancement in the echo occurrence rate between 65^0 and 71^0 MLat in the auroral oval region, located about midnight between 18:00 and 05:00 MLT. Occurrence rates sharply drop off at the equatorward edge of the auroral oval, but extend to more equatorward latitudes between 18:00 and 21:00 MLT for winter and equinox, and between 20:00 and 22:00 MLT for summer. The equatorward region of enhancement is strongest and covers the largest area in winter.

4.3.2 Echo parameters

(a) Echo power

Figure 4.2d-f indicates the average echo power measured by the King Salmon radar over the same three months of observation in MLT-MLat coordinates. Data are only presented for those bins that have more than 50 echoes, and echo occurrence rates above 2%. For each diagram the power is largest on the nightside and lowest on the dayside. The highest powers observed are up to 20 dB during winter between 02:00 and 06:00 MLT and during equinox around magnetic midnight. According to the comparative study presented in the previous Chapter, 20 dB agrees well with the average power of $\sim$19 dB observed by various Northern and Southern Hemisphere radars.

The highest powers, Figure 4.2d-f, are also collocated with the auroral zone. In the winter, summer, and equinox (to a lesser extent), these enhanced powers spread equatorward of the auroral oval in the dusk sector. In the winter there is an additional peak of high power located equatorward of the auroral oval on the dawnside. In all three diagrams the regions of enhanced power correspond to the regions of enhanced occurrence rates shown in the previous diagrams. This distribution of power and its correspondence to the echo occurrence rate is maintained for various months and years of observations regardless of season or year and agrees with the results of *Villain et al.* (2002) who considered a collection of radars in the Northern Hemisphere.

(b) Velocity of echoes

Figures 4.3a-c presents statistics of monthly averaged King Salmon l-o-s velocities in MLT-MLat coordinates. Data are only presented for those bins that have more than 50 echoes, and echo occurrence rates above 2%. The same three months of observations are considered. The red (blue) color is used to denote a westward, negative (eastward, positive) velocity of motion. From 65^0 to 70^0 MLat, the diagrams show a general trend of velocity polarity reversal (transitions between red and blue) around magnetic midnight.

The prominent feature of all three diagrams is a region of strongly enhanced velocity close to $\sim 65^0$ MLat between 19:00 and 22:00 MLT in the dusk sector. The magnitude of the maximum average velocity is 425-638 m/s in this region. This is high in comparison with a background velocity of 0-425 m/s at other latitudes and magnetic local times. At equinox there is an additional region of enhanced velocities at ∼17:30 MLT and $\sim 66^0$ MLat. Summer observations also show an additional area of very strong velocities centered on 14:00 MLT and 70^0 MLat. All three diagrams indicate a wide-spread region of enhanced eastward velocity on the dawnside from 00:00 to 09:00 MLT between 65^0 and 77^0 MLat. The magnitude of this flow is 213-425 m/s compared to the flow of 0-213 m/s at other latitudes. The equatorward extension of enhanced occurrence rates shown in Figure 4.2a-c corresponds with the

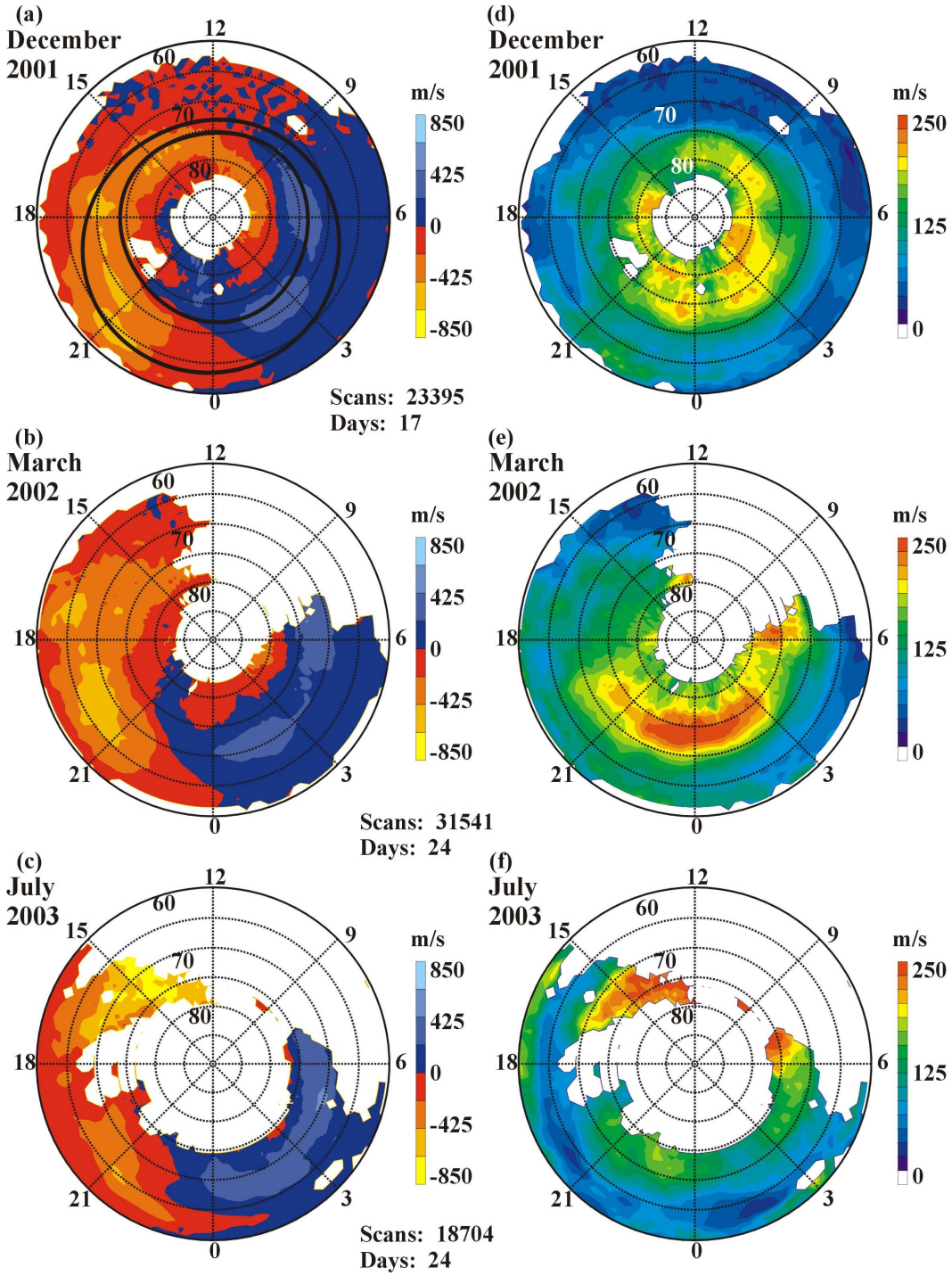

Figure 4.3: King Salmon averaged line-of-sight velocity and averaged spectral width for winter (December 2001, panels (a) and (d)), equinox (March 2002, panels (b) and (e)), and summer (July 2003, panels (c) and (f)) in magnetic latitude-magnetic local time coordinates.

location of the high velocity flows. Power over the enhancement is a few decibels larger than in the region immediately surrounding the enhancement (Figures 4.2d-f).

The regions of high duskside velocity are comparable in the equinox and winter months and relatively small in the summer months. In December there appear to be two separate enhancements located at ∼21:00 MLT centered at 64^0 and 69^0 MLat. The poleward enhancement is located almost entirely within the auroral oval, and the equatorward enhancement overlaps the equatorward edge of the auroral oval. During equinox and summer the duskside velocity enhancements also overlap with the equatorward edge of the auroral oval. There seems to be a seasonal trend; enhanced velocities occur in a broader region of MLT at lower latitudes in the winter months, and over smaller regions at equinox, and much smaller over the summer. This morphology seems to reflect a change in the ionospheric conductance; in the winter, solar luminosity, and therefore ionospheric conductivity, is decreased, and a larger $\mathbf{E}\times\mathbf{B}$ drift can be established, provided about the same field-aligned current is established between the ionosphere and the magnetosphere.

We investigated the possibility of a solar cycle effect in the velocity but did not find anything consistent. For all periods (December 2001, 2003, and 2004) high velocity echoes were found to be located in the low latitude duskside region (diagrams not shown). For 2002 the high velocity distribution seems to be rotated eastward and shifted poleward of observations for all other years.

(c) Width of echoes

The spectral widths of the King Salmon echoes are plotted in Figures 4.3 d-f. Data are only presented for those bins that have more than 50 echoes, and echo occurrence rates above 2%. Unlike the distribution for echo power, the location of enhanced spectral width does not correspond to the region of enhanced occurrence rate. Instead, for winter and equinox, enhanced spectral widths are confined to latitudes greater than 70^0 MLat and poleward of the auroral oval, in agreement with *Villain et al.* (2002). In summer the enhanced spectral widths on the dawnside are located poleward, within, and equatorward of the auroral oval. Widths appear to

be as high as 250 m/s on the nightside during equinox and on the dayside during summer. Values are not as large during the winter. The transition between high and low spectral widths is sharp for the summer. For winter and equinox, larger spectral widths appear on the duskside, compared to the dawnside at low latitudes. In examining the spectral widths for December 2001-2004, one may notice that as the solar activity decreases, the high latitude spectral width increases by as much as 100 m/s.

4.3.3 Comparison of King Salmon observations with Stokkseyri and Unwin measurements

(a) Stokkseyri versus King Salmon

The King Salmon radar observations are not typical of other Northern Hemisphere SuperDARN radars. The most important difference is that other radars do not see westward velocity enhancements in the dusk sector. For example, see sample velocity distributions for the Saskatoon and Stokkseyri radars presented by *Hamza et al.* (2000), their Figure 2. For radars that scan perpendicular to the magnetic L-shells, like Hankasalmi or Kapuskasing, this is not surprising as the evening sector flow is often elongated with the L-shells. Other radars, like the Stokkseyri radar, have azimuthal orientations similar to the King Salmon radar.

For comparison with King Salmon, Stokkseyri observations were processed. The appropriate data are presented in Figure 4.4a,c for December 2001. The Stokkseyri occurrence rates, Figure 4.4a, are typical of other Northern Hemisphere radars (*Koustov et al.*, 2004). In the winter months, the occurrence rates have a similar distribution about midnight as King Salmon, but the rates are 2-3 times larger. In terms of velocity, Figure 4.4c, Stokkseyri observations do not indicate fast flow streams in the dusk sector where the flow magnitude is consistently less than 425 m/s. In addition, a small localized westward flow enhancement is observed centered at 15:00 MLT and $\sim 73^0$ MLat. This enhancement ranges from 425 to 638 m/s. The velocity magnitude gradually decreases toward midnight at all magnetic

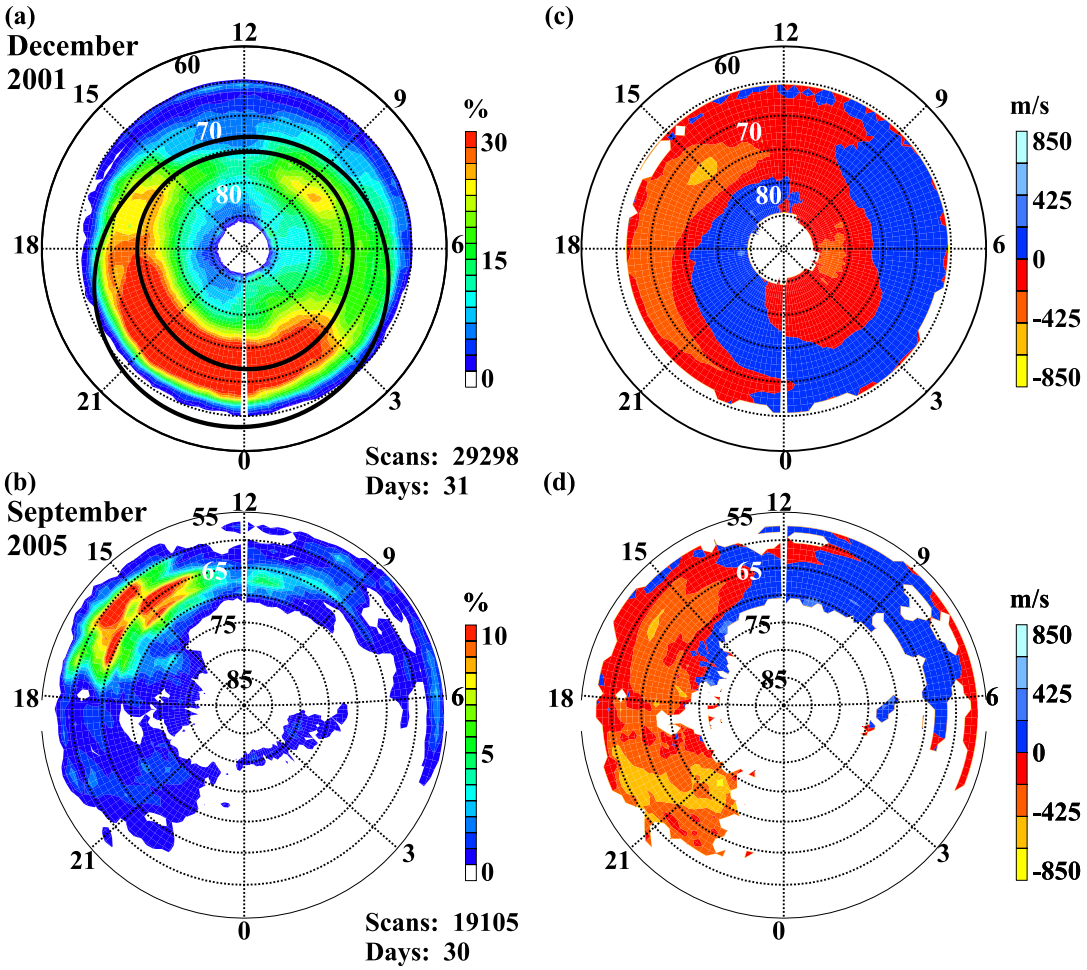

Figure 4.4: Echo occurrence rate and averaged line-of-sight velocity for Stokkseyri (December 2001, panels (a) and (c)) and Unwin (September 2005, panels (b) and (d)) in magnetic latitude-magnetic local time coordinates. Note that the magnetic latitudes for Stokkseyri and Unwin are slightly different.

latitudes. Both the westward and eastward enhancements agree with the velocity profiles presented by *Hamza et al.* (2000), their Figure 2.

The power and spectral width distributions for the Stokkseyri radar (not shown) share similarities with the King Salmon radar. Regions of enhanced power of up to 20 dB overlap with the largest occurrence rates. The overall average power is higher than for King Salmon. This is consistent with the overall increased occurrence rate. Like King Salmon, the highest spectral widths for Stokkseyri are located poleward of the auroral oval. Overall, the spectral widths are lower for Stokkseyri,

reaching a maximum of $\sim$ 200 m/s. Unlike King Salmon, there is an additional band of high spectral width between 65^0 and 70^0 MLat in the afternoon and dusk sectors.

It is likely that differences between the King Salmon and Stokkseyri echoes are due to the different magnetic latitudes of the radars. The Stokkseyri radar observational area is 5^0 poleward of the King Salmon radar's field of view and at typical auroral oval latitudes. One can hypothesize that the echoes observed by the King Salmon radar at lower latitudes can be associated with additional flows originated from sources that are not operational at auroral oval latitudes.

(b) Unwin versus King Salmon

The TIGER-Unwin SuperDARN radar field of view is magnetically conjugate to the King Salmon radar's field of view. Unwin has a similar azimuthal alignment and can view magnetic latitudes as equatorward as $\sim 57^0$. This radar started operation in late 2004 (while work with the King Salmon data was under way). We took a quick look at Unwin radar data to see if there are similarities with the King Salmon observations. Figure 4.4b shows the occurrence rates for September 2005 in MLat-MLT coordinates. Like King Salmon, Unwin has a lower than average occurrence rate. There is an enhancement up to $\sim$10% on the duskside from 13:00 to 17:00 MLT. Figure 4.4d shows the average velocities observed by Unwin in September 2005. Due to a lack of echoes all data were presented provided there where more than 20 echoes in a MLT-MLat bin. The radar observes a velocity enhancement of 425-638 m/s spreading from 59^0 to 75^0 MLat between 18:00 and 22:00 MLT. The fast flows are mostly located within the auroral oval, but also extend equatorward. There is an additional enhancement at 16:00 MLT and $\sim 63^0$ MLat. The velocity observations are similar to those shown for King Salmon in Figure 4.3e during equinox. Clearly, King Salmon and Unwin data are similar, but a more focused investigation is required in the future.

4.4 King Salmon high-velocity flows in the dusk sector and their possible origin

The velocity statistics presented in Figure 4.3a-c suggest the appearance of localized velocity enhancements at low latitudes in the late-duskside sector is a persistent feature of King Salmon radar observations. We now investigate various properties of the flow intensifications and attempt to identify possible mechanisms responsible for their occurrence through a detailed analysis of several individual fast flow events.

4.4.1 Examples of high-velocity King Salmon flows

Fast flow events are easy to identify by examining King Salmon SuperDARN velocity-time quick-look plots in beam 1. We consider data in this beam because it is the most L-shell aligned, and can therefore best look along the expected direction of SAPS flows. As an example, consider the l-o-s velocity plotted in MLat-UT coordinates for an event on December 05, 2001 between 08:00 and 10:30 UT, Figure 4.5. There is a "blob" of echoes with velocity exceeding 1600 m/s centered at $\sim 63^0$ MLat lasting from 09:22 to 09:56 UT. Neither the power nor the spectral width during this period suggest the high-velocity echoes are untypical, but the velocities are exceptionally high for any SuperDARN observation (e.g., *Lacroix and Moorcroft*, 2001). Initially, the velocity enhancement is located just below 63^0 MLat. It quickly expands both poleward and equatorward. The equatorward expansion stops when the velocity peaks at approximately 09:40 UT. Lower velocity echoes (<800 m/s) exist prior to, during, and after the duration of the high-velocity blob, at more equatorward latitudes. One can notice that the velocity of the more poleward low-velocity echoes increased to 1200 m/s at approximately 09:00 UT and then returned to values <800 m/s after 10:00 UT, about 30 minutes after the high-velocity blob disappeared.

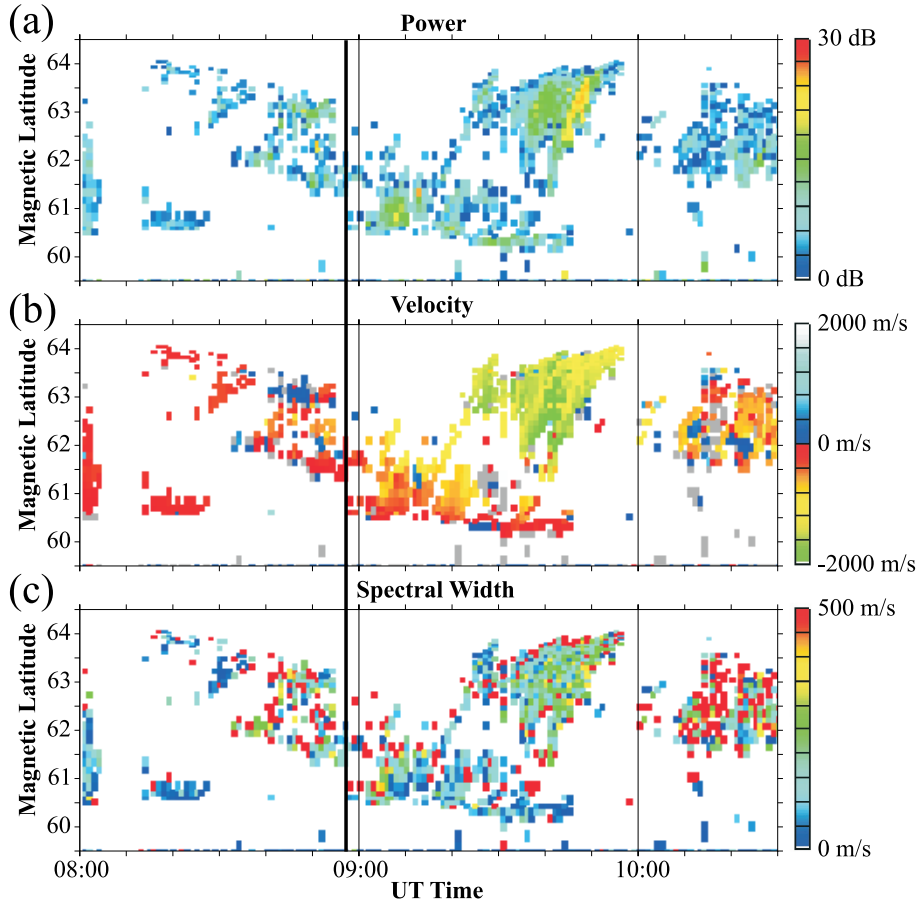

Figure 4.5: Echo (a) power, (b) Doppler velocity, and (c) spectral width in beam 1 of the King Salmon radar for December 5, 2001 in AACGM magnetic latitude - universal time coordinates.

Large velocities were not only observed in azimuthally oriented beams, such as beam 1, but also in more meridionally oriented beams, such as beams 5-10. The velocity in more meridional beams was not as high (maximum of 1300 m/s) as in the azimuthal beams, but the radar started their detection earlier, at approximately 08:30 UT. The exceptionally high velocity observed in the azimuthal beams is very localized in both space and time. We note that the velocity enhancement was observed with some delay from a substorm that started near the radar's field of view at ∼08:57 UT. We will discuss this issue later, but indicate the onset by a vertical line in Figure 4.5.

Figure 4.6 illustrates another fast flow event on December 15, 2001 between 08:30 and 11:00 UT. One immediately notices a band of high velocities (> 600

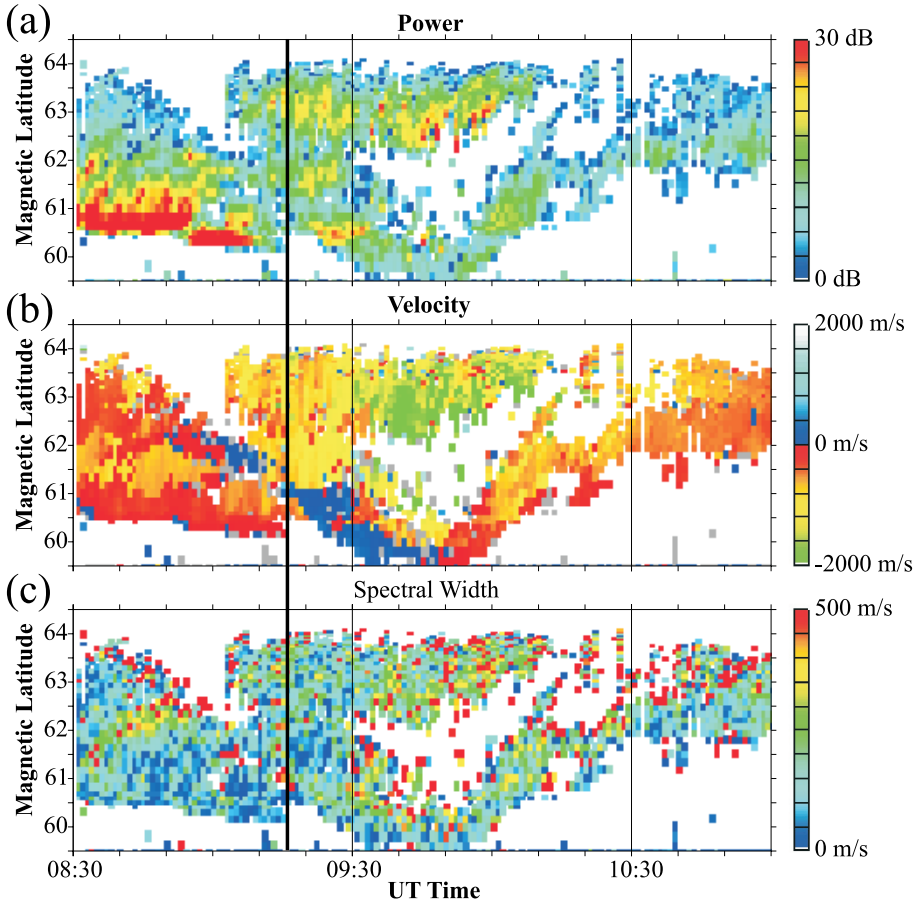

Figure 4.6: Echo (a) power, (b) Doppler velocity, and (c) spectral width in beam 1 of the King Salmon radar for December 15, 2001 in AACGM magnetic latitude - universal time coordinates.

m/s) from 09:00 to 10:30 UT between 62^0 and 64^0 MLat. The enhancement reaches velocities of at least 1600 m/s between 09:30 and 10:10 UT. The flows peak from ∼09:35 to 09:48 UT and then recede poleward and decay in magnitude. There are additional enhancements of up to ∼1000 m/s equatorward of the main enhancement between 61^0 and 62^0 MLat from 09:00 until 09:30 UT and between 60^0 and 61^0 MLat from 09:30 until 09:50 UT. Velocity is generally <600 m/s prior to and after the enhancement. The fast flows in both events are short lived (<1 hour) and the velocities are large compared to the background flow in nearby areas. We note that similar to the previous event, a substorm occurred near the area of King Salmon observations. The substorm onset time of ∼09:15 UT is indicated in the diagram.

4.4.2 High-velocity flow onset as a part of substorm-related auroral oval electrodynamics: December 15, 2001

We consider a fast flow event on December 15, 2001 in more detail to determine conditions in the Earth's magnetosphere and ionosphere corresponding to the velocity enhancement. We also examine the temporal and spatial location of the fast flows with respect to auroral luminosity observed using the IMAGE satellite.

(a) Geophysical conditions

The December 15, 2001 fast flow event (Figure 4.6) progresses in relation to the development of a substorm whose onset was identified by IMAGE at ∼09:15 UT. The Kp index was 2o prior to 09:00 UT and then 2+ for the next three hours. Figure 4.7 summarizes the geophysical parameters during the event, from 08:30 UT until 11:00 UT. The vertical solid line in all panels indicates the substorm onset time. Figure 4.7a shows the maximum westward velocity (averaged across three adjacent cells) detected in beam 1 of the King Salmon radar (for any possible range) plotted against UT and smoothed using a box car average of width three. The shaded bar indicates the temporal location of the velocity enhancement identified in Figure 4.6. The westward velocity begins to increase approximately ten minutes prior to the substorm onset and peaks with a magnitude of ∼2400 m/s at 09:52 and 10:04 UT.

Data presented in Figures 4.7b and 4.7c document the substorm development. Figure 4.7b shows observations of three magnetometers at Kaktovik (MLat=70.7^0) Gakona (MLat=63.5^0) and Dawson (MLat=66.0^0), located in Alaska, slightly eastward of the high-velocity blob. The exact locations of these magnetometers are shown later in Figure 4.15a.

Kaktovik (thick line) indicates the H-component of the Earth's magnetic field sharply decreases at 09:15 UT and reaches a minimum at 09:21 UT and at 09:32 UT. The Gakona magnetometer (thin line) shows similar trends. The lower portion of this panel shows the Pi2 magnetic pulsations (magnified 10 times) observed at Dawson, located slightly eastward of Kaktovik and Gakona. The pulsations intensify at 09:15

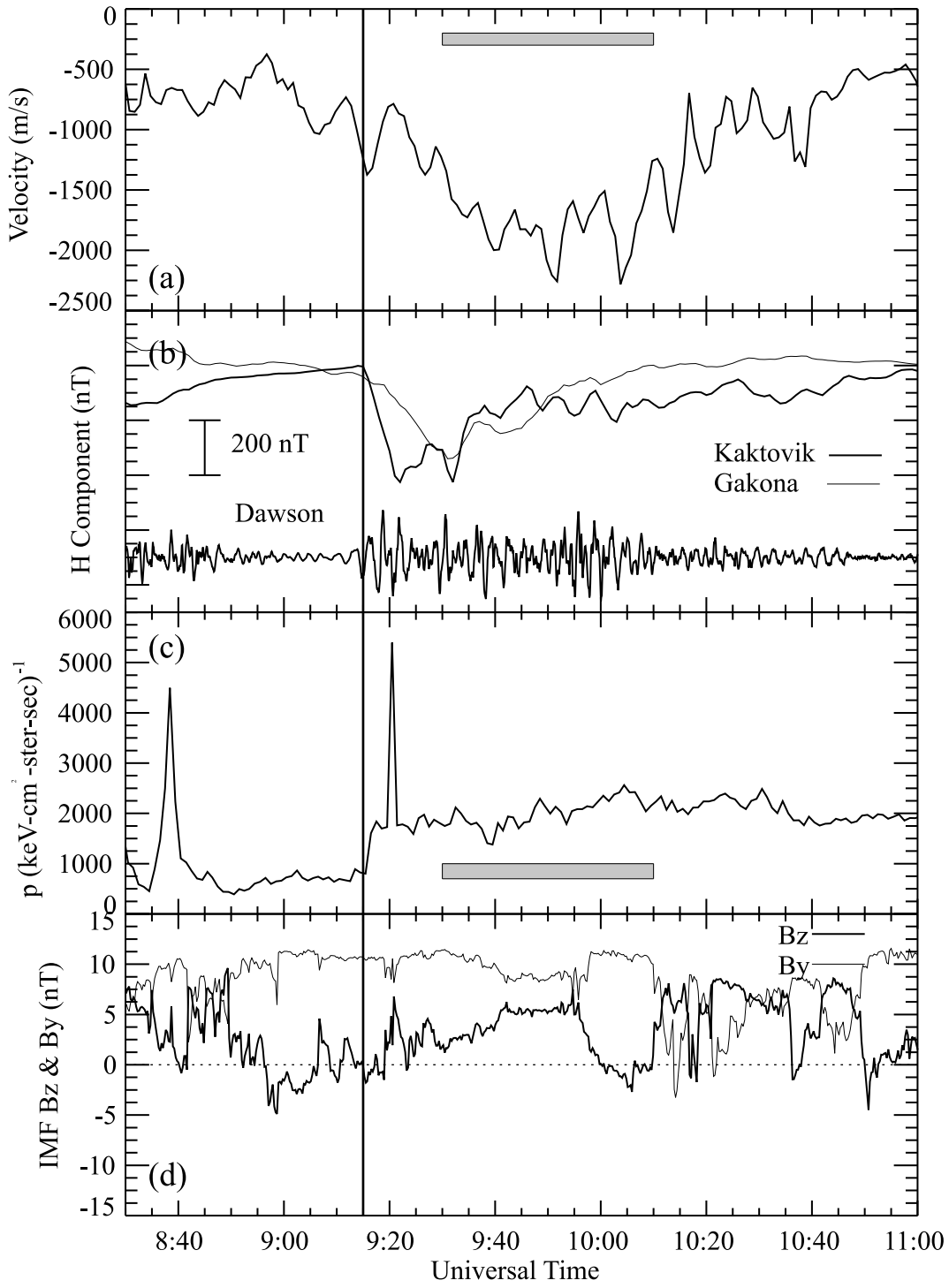

Figure 4.7: Summary of the data for the December 15, 2001 event: (a) maximum velocity along beam 1 of the King Salmon HF radar, (b) H-component of magnetic perturbations at Kaktovik and Gakona and Pi2 magnetic pulsations at Dawson, (c) flux of energetic protons according to measurements by the geostationary satellite LANL 1994_080 and (d) IMF B_z and B_y components. Vertical line indicates the time of the substorm onset.

UT, confirming the time of the substorm onset. Magnetometer observations suggest the peak velocity flow at 09:52 UT was observed during the recovery phase of the substorm.

Figure 4.7c shows the flux of energetic protons (50-400 keV range) as observed by the Synchronous Orbit Particle Analyzer (SOPA) instrument onboard the geostationary LANL satellite 1991_080. During the high-velocity event, the satellite was located in the pre-midnight sector of the magnetosphere over the area of interest. The data indicates that the background flux of energetic protons doubles at substorm onset as identified by magnetometers.

The final panel, Figure 4.7d, indicates the magnitudes of the IMF B_y (thin line) and B_z (thick line) components as measured by the ACE satellite throughout the duration of the substorm. The IMF data were shifted by 81 minutes to account for disturbance propagation from the satellite position to the magnetosphere. B_y is primarily positive throughout the event with two brief dips between 10:10 UT and 10:50 UT. B_z fluctuates around zero from 09:05 UT until 09:20 UT where it remains positive until 10:35 UT, with a brief exception from 10:00 to 10:10 UT.

(b) Substorm development and high-velocity flow onset

The substorm development is clearly seen by the optical data collected by the IMAGE satellite. Figures 4.8a and 4.8b illustrate 6 frames of the nightside IMAGE WIC observations at 09:00 UT, 09:13 UT, and 09:15 UT in Figure 4.8a and 09:27 UT, 09:43 UT, and 09:50 UT in Figure 4.8b. SuperDARN convection maps (matched as closely as possible in time) are overplotted. Data from all Northern Hemisphere SuperDARN radars, including the King Salmon radar, were used to create the convection maps using the standard map potential technique described in Section 2.1.3. The top panel in Figure 4.8a corresponds to a quiet auroral oval 15 minutes prior to the substorm onset. The duskside return flow velocity is approximately 400 m/s. Several minutes later at 09:13 UT, middle panel, the westward flow begins to increase to 500-600 m/s in a band from 64^0 to 67^0 MLat, equatorward of the duskside convection vortex.

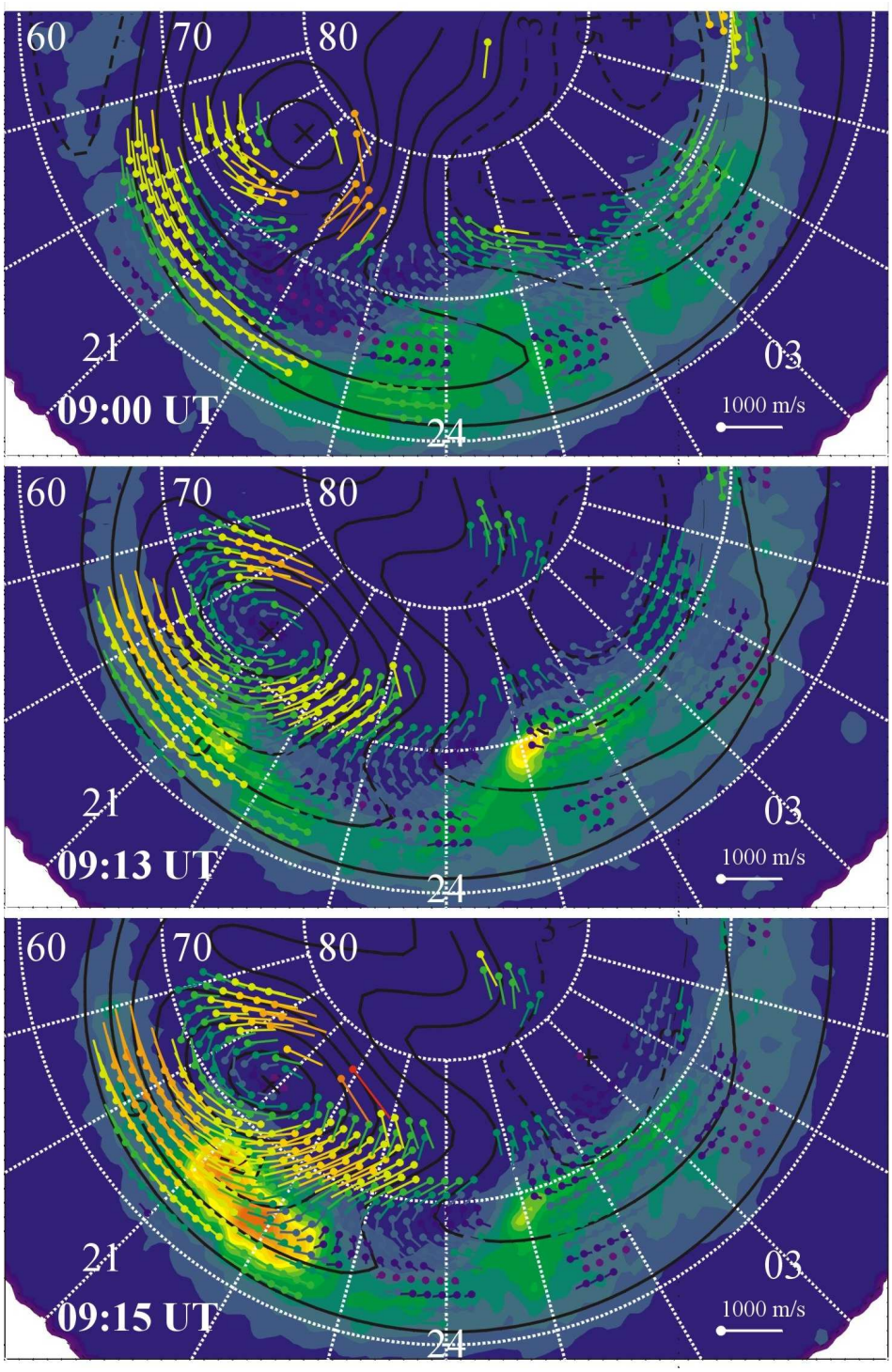

Figure 4.8a: Three global images of the auroral luminosity according to IMAGE observations and matched SuperDARN maps of plasma convection for the growth phase and onset of a substorm on December 15, 2001 at 09:00 UT, 09:13 UT, and 09:15 UT. Red (blue) color corresponds to the strongest (weakest) luminosity or convection.

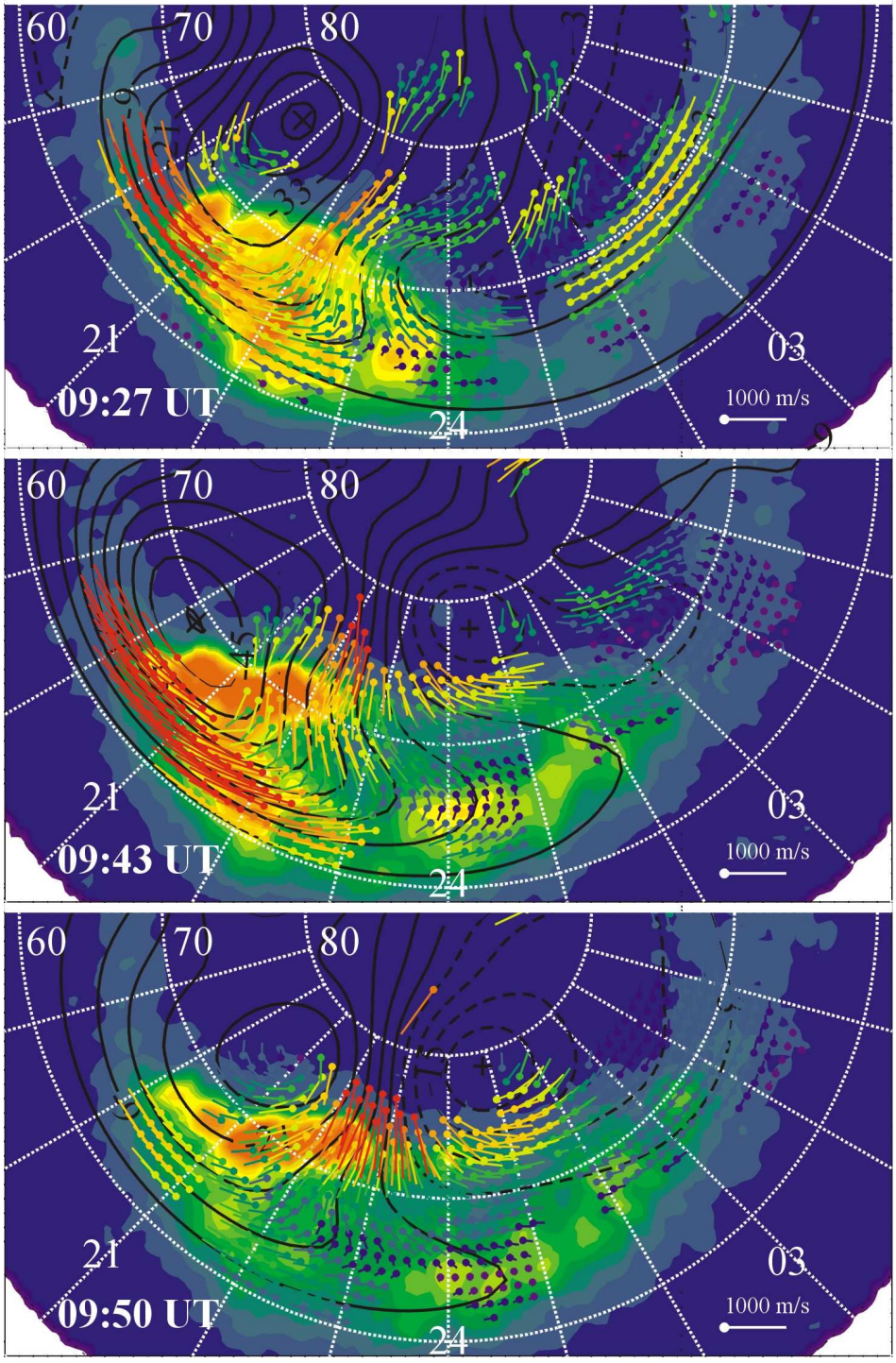

Figure 4.8b: Three global images of the auroral luminosity according to IMAGE observations and matched SuperDARN maps of plasma convection for the expansion and recovery phases of a substorm on December 15, 2001 at 09:27 UT, 09:43 UT, and 09:50 UT. Red (blue) color corresponds to the strongest (weakest) luminosity or convection.

At substorm onset, bottom panel of Figure 4.8a, a blob of enhanced luminosity due to increased particle precipitation appears at 21:30 MLT and 65^0 MLat. The duskside return flow increases to as much as 800 m/s. It is important to realize that the high-velocity band is located at auroral oval latitudes, westward of the enhanced luminosity. During the expansion phase of the substorm the luminosity spreads as far westward as 20:00 MLT and expands poleward. Near the end of the expansion phase, top panel of Figure 4.8b, the fast flow band has increased in width, expanding both poleward and equatorward, and the westward flow velocity ranges from 800 to 1000 m/s. The maximum convection velocity is observed during the recovery phase of the substorm at 09:43 UT, middle panel. At this time, the luminosity is enhanced significantly poleward of its onset location; the luminosity has decayed in the most equatorward part of the auroral oval. Correspondingly, the peak velocity band has shifted equatorward to 61^0-66^0 MLat and eastward of its original location. Velocities in this band range from 1000 to 1200 m/s; they are concentrated equatorward of the maximum luminosity band. Visual comparison of the optical and convection data suggests the high-velocity westward flow overlaps with the equatorward edge of the auroral oval. By 09:50 UT, bottom panel of Figure 4.8b, the auroral luminosity has decayed significantly and the flow velocity has dropped to $\sim$600 m/s.

To obtain a more quantitative account of changes in the average convection velocity with respect to changes in the auroral luminosity, we consider the average convection magnitude and luminosity in specific regions of the duskside ionosphere, as illustrated in Figure 4.9. We consider an equatorward (61^0-67^0 MLat, blue lines) and a poleward (67^0-73^0 MLat, red lines) band of luminosity between 20:00 and 23:00 MLT. Velocity is considered between 60^0 and 67^0 MLat in the 19:00-22:00 MLT sector (green lines).

Figure 4.10 presents the resultant averages using the same color scheme. Luminosities in both latitudinal ranges increase near the substorm onset at 09:15 UT. The equatorward luminosity band reaches a peak within 5 min of the onset, peaks again at 09:37 UT and then drops. The poleward luminosity peaks once at 09:37 UT (22 min after the onset) and again 15 min later (37 min after the onset). Both

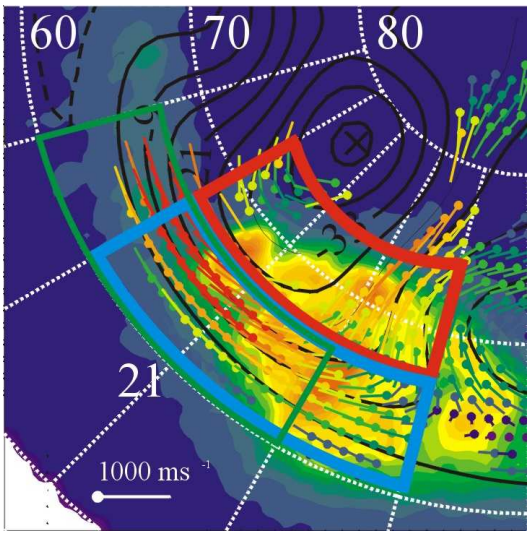

Figure 4.9: IMAGE auroral luminosity and overplotted SuperDARN convection measurements. Averaging region for high latitude luminosity (red), low latitude luminosity (blue) and convection velocity (green) are overplotted.

luminosities are decreasing steadily after ∼09:40 UT. The average convection velocity increases from ∼350 m/s to 500 m/s 15 minutes prior to the substorm onset and continues to increase, peaking at ∼09:44 UT, and again at 10:06 UT. This plot indicates the enhanced luminosity begins in the equatorward region and then spreads poleward. The velocity does not peak at equatorward locations until the luminosity has shifted poleward.

(c) Summary

For the December 15, 2001 event, a high-velocity stream began to form prior to the substorm onset and continued to increase during the expansion phase. The fast flow region coincided with the auroral oval luminosity being westward of the bulge (enhanced luminosity) region. During the substorm recovery phase, the luminosity receded poleward, and the enhanced convection moved eastward and equatorward. The fast flows identified are very similar to SAPS in their magnitude, temporal, and spatial extent, but they are located within and overlapping with the equatorward edge of the auroral oval.

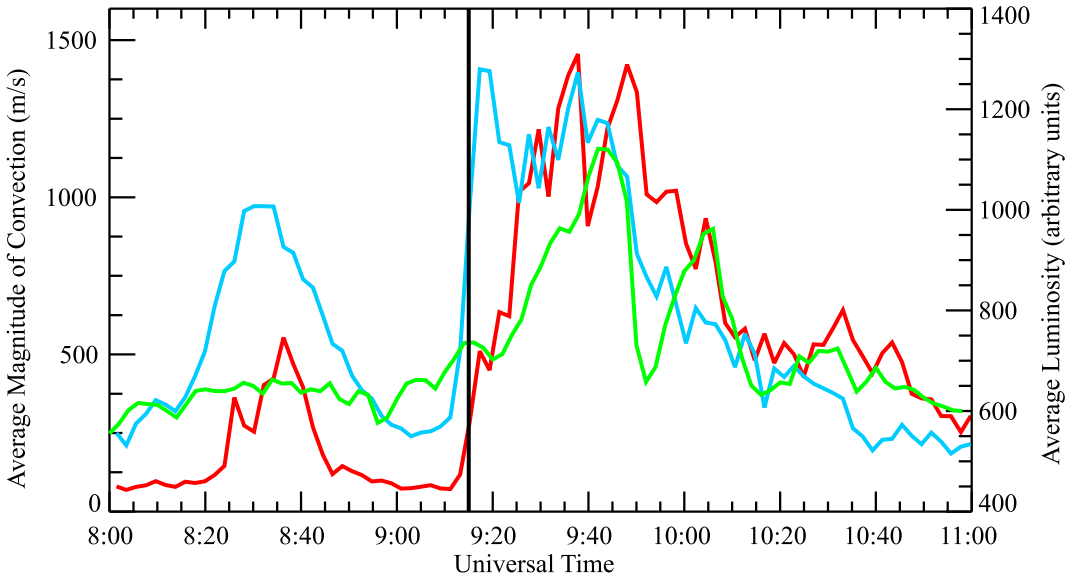

Figure 4.10: Luminosity and convection data for a December 15, 2001 substorm. IMAGE luminosity for high latitudes (red line) averaged across 20:00 to 23:00 MLT and 66^0 to 76^0 MLat and low latitudes (blue line) in the same MLT sector and 60^0 to 66^0 MLat. Convection velocity (green line) averaged across 19:00 to 22:00 MLT and 60^0 to 66^0 MLat. Vertical line indicates the substorm onset.

4.4.3 Onset of exceptionally strong flows at the equatorial edge of the auroral oval: December 5, 2001

Although the December 15, 2001 event is an excellent example of high convection velocities, another event would better illustrate the development of exceptionally strong flows at the equatorial edge of the auroral oval; flows that can be classified as SAPS. We note that for the December 15, 2001 event the fastest flows occurred when the luminosity faded at the equatorial edge of the auroral oval. We now consider another fast flow event on December 5, 2001. This event is similar to the December 15, 2001 event, but the onset of extremely fast flows at the equatorward edge of the auroral oval is more evident.

(a) Geophysical conditions

The December 05, 2001 fast flow was also observed during only slightly disturbed conditions, the Kp index was 2+. The event occurred during the recovery

phase of a weak storm; the Dst was -30 nT for several hours around the interval of interest. Figure 4.11 presents the geophysical conditions throughout the event from 08:00 to 10:30 UT in the same format as for Figure 4.7. The velocity began to increase just before 09:00 UT and peaked at approximately 1900 m/s, 40 min later, 4.11a. The beginning of the velocity enhancement corresponds to a substorm onset at 08:57 UT, as identified by IMAGE satellite optical data. Magnetometers confirm the substorm onset time. Kaktovik indicates the H-component of the Earth's magnetic field sharply decreased at 08:57 UT, and the peak of the expansion phase of the substorm was at $\sim$ 09:25 UT, Figure 4.11b. This suggests the peak velocity flow was also observed during the recovery phase of the substorm. Gakona does not show a strong magnetic decrease near the onset time as the substorm is confined to higher latitudes. The Pi2 magnetic pulsations observed by Dawson (magnified 6 times) intensify at 08:57 UT, confirming the time of the substorm onset. The LANL satellite data indicates a rapid, strong proton flux enhancement at 09:00 UT, just after the substorm onset, and a separate enhancement approximately 20 minutes later, Figure 4.11c. It is likely that these correspond to two separate particle injections into the plasmasphere boundary layer.

According to Figure 4.11d, the IMF B_y is primarily negative during the 2.5 hour interval with a brief positive excursion at 10:20 UT. B_z fluctuates near zero for at least 15 minutes prior to the substorm onset and becomes positive approximately 5 minutes after onset, while the velocity is intensifying, until about 09:30 UT when it changes polarity. It should be noted that the fastest flows were observed during an interval where the IMF B_z component had changed polarity from positive to negatives values. It is possible that this polarity reversal activated merging processes in the tail, providing strong convection at the edge of the auroral oval through a magnetospheric electric field increase and strong field penetration. However, we note that the velocity in beam 1, Figure 4.11a, was increasing in magnitude before the change in B_z occurred. In fact, the smooth shape of the velocity plot suggests the B_z transition did not even change the trend of the velocity.

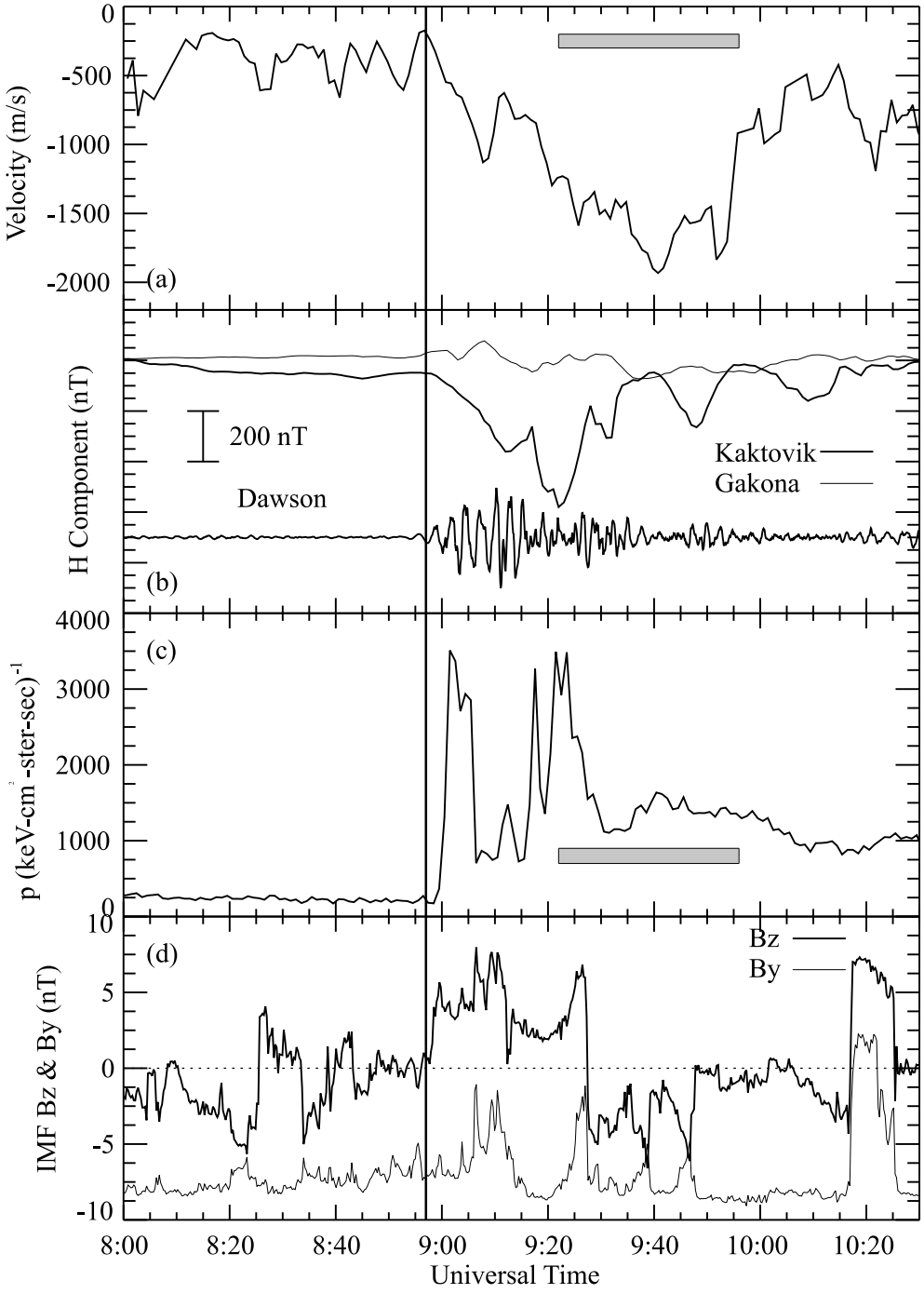

Figure 4.11: Summary of the data for the December 5, 2001 event: (a) maximum velocity along beam 1 of the King Salmon HF radar, (b) H-component of magnetic perturbations at Kaktovik and Gakona and Pi2 magnetic pulsations at Dawson, (c) flux of energetic protons according to measurements by the geostationary satellite LANL 1994_080 and (d) IMF B_z and B_y components. Vertical line indicates the time of the substorm onset.

(b) Substorm development, auroral oval and high-velocity flow at its equatorward edge

The substorm development is clearly seen in the optical data collected by the IMAGE satellite. Figure 4.12a,b shows 4 frames of the IMAGE WIC observations at 08:51 UT and 09:02 UT in Figure 4.12a, and 09:18 UT and 09:34 UT in Figure 4.12b, with SuperDARN convection maps (matched as closely as possible in time) overplotted. The top panel of Figure 4.12a corresponds to a quiet auroral oval, approximately 7 min prior to the substorm onset. The convection pattern consisted of two cells with a dominating morning cell, which is consistent with the strongly negative B_y component of the IMF.

Five minutes after the substorm onset, bottom panel of Figure 4.12a, a significant area of enhanced luminosity is visible from 21:00 to 24:00 MLT, centered on 66^0 MLat. The convection pattern clearly shows that right after the substorm onset, vortical flows of opposite directions are visible in the dusk and dawn sectors. The vortices are centered at 70^0 MLat and 21:00 MLT on the duskside, which is significantly equatorward of its location in the top panel, and 03:00 MLT on the dawnside. These vortices are very similar to those reported by *Grocott et al.* (2002) for the substorm onset time. The flow within the duskside vortex is particularly strong on the west-side, in agreement with the King Salmon l-o-s velocity measurements. In general, the flow shifted equatorward and intensified in both the meridional and azimuthal directions. The intense auroral luminosity is located southeast of the focus of the large-scale convection focus. The fastest flow is westward, located west of the bulge. Slower westward flow is observed both within and equatorward of the auroral bulge. The enhanced flow correlates with the weaker precipitation and lower conductance west of the auroral bulge.

The top panel of Figure 4.12b corresponds to a time ∼21 min after the substorm onset, near the end of the expansion phase of the substorm. The area of enhanced luminosity is shifted westward and spans from 19:00 to 01:00 MLT. The luminosity is also shifted poleward to 70^0 MLat leaving areas of low conductance

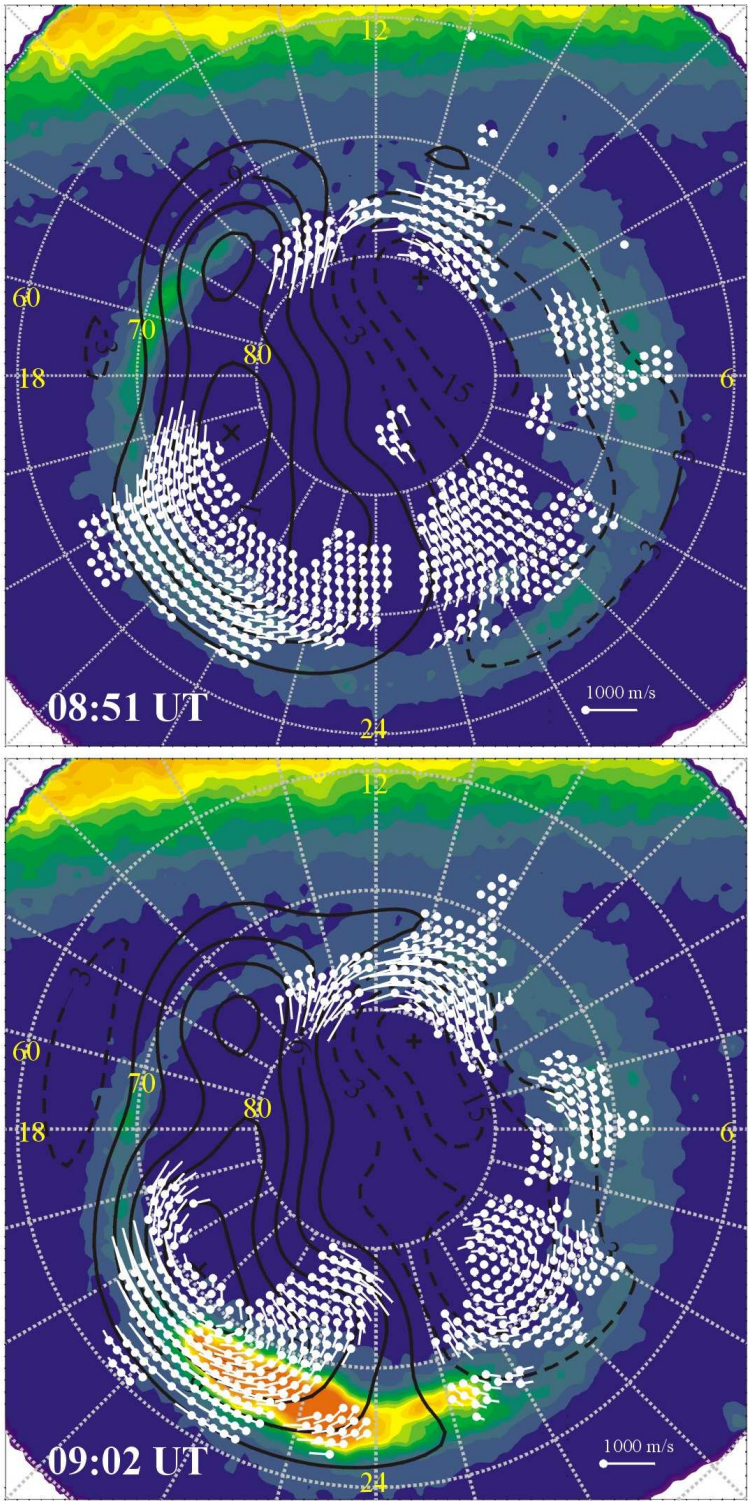

Figure 4.12a: Auroral luminosity according to IMAGE observations and matched SuperDARN maps of plasma convection for a substorm on December 5, 2001 at 08:51 UT and 09:02 UT. Red (blue) color corresponds to the strongest (weakest) luminosity.

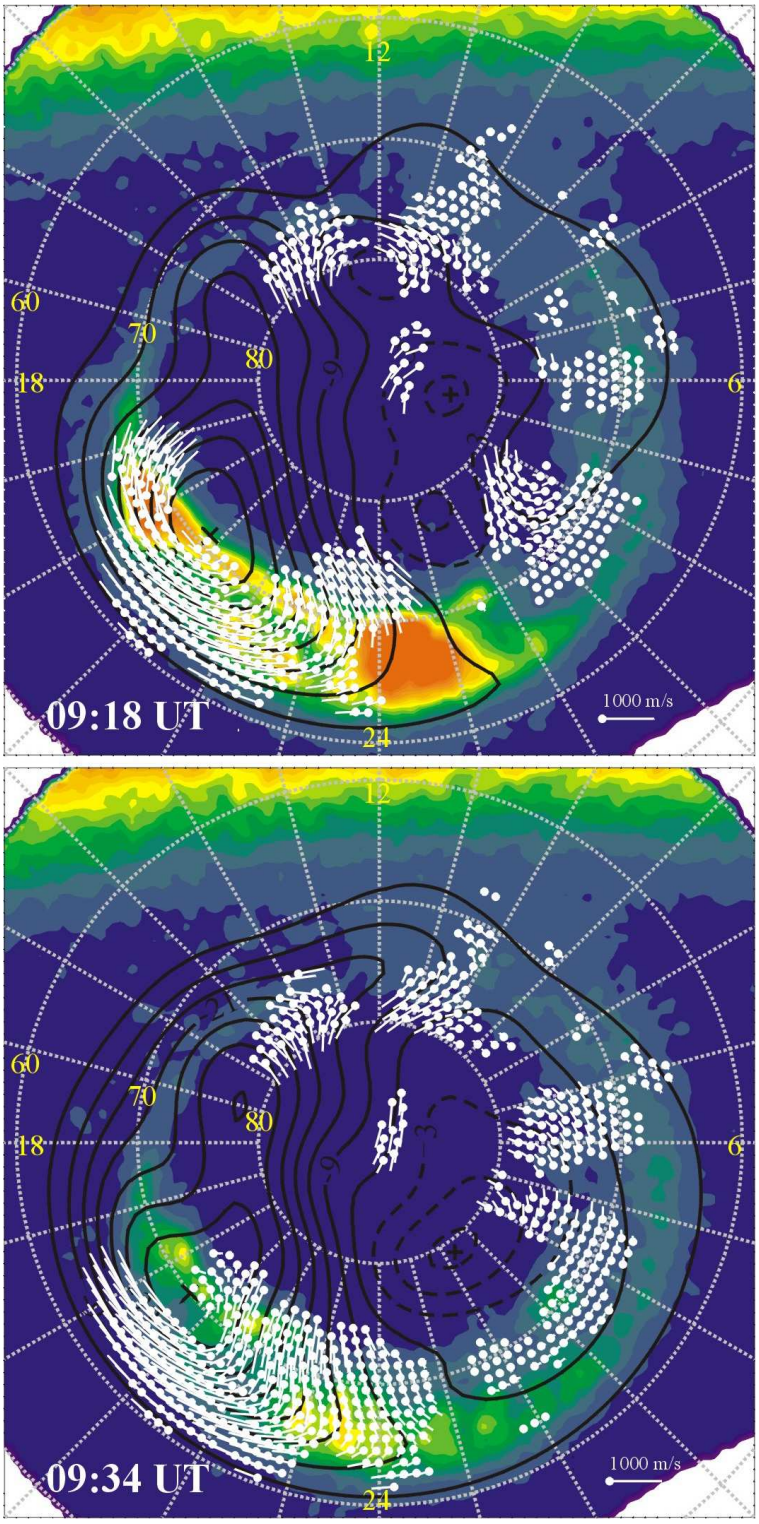

Figure 4.12b: Auroral luminosity according to IMAGE observations and matched SuperDARN maps of plasma convection for a substorm on December 5, 2001 at 09:18 UT and 09:34 UT. Red (blue) color corresponds to the strongest (weakest) luminosity.

in the equatorward region, where high luminosities were observed in the previous frame. This poleward shift in the luminosity is first observed at ∼09:06 UT, and ends a few minutes after this frame. The overall velocity magnitude is larger and the most enhanced velocities are located equatorward of the auroral zone in areas where the auroral luminosity and therefore the conductance has decreased.

The final panel corresponds to a time when the largest westward velocities are observed. Only remnants of the enhanced luminosity remain; they are located poleward of 70^0 MLat and at 23:00 MLT. The strong westward flow at the equatorward edge of the original duskside vortex has expanded to its most equatorward location of nearly 60^0 MLat. Visual comparison of the optical and convection data in both panels of Figure 4.12b suggest the high-velocity westward flow overlaps the equatorward edge of the auroral oval.

Figure 4.13 provides a quantitative account of changes in the average convection velocities measured by SuperDARN and the luminosity in the evening sector from 19:00-23:00 MLT for 2 latitudinal regions of 60^0-67^0 (blue line) and 67^0-74^0 (red line). Velocity is considered in the 19:00-23:00 MLT sector from 60^0 to 66^0 MLat (green line). The poleward band of luminosity begins to increase at substorm onset and then sharply increases about 10 min later and reaches almost double its original value at approximately 09:23 UT and then slowly decreases to its pre-substorm intensity. The equatorward luminosity sharply intensifies at the onset, peaking less than five minutes later and decaying to its pre-substorm level by 10:00 UT. Prior to onset the convection velocity is ∼300 m/s. Convection slows approximately 10 minutes before onset as the equatorward portion of the luminosity begins to increase. The velocity quickly increases at substorm onset, with another quick enhancement starting about 15 minutes later, just after the more poleward luminosity increases. The velocity continues to increase to a maximum at 09:45 UT, and steadily drops off until 10:15 UT when it returns to its pre-substorm level. It is important to note that during the period of maximum velocity, the equatorward luminosity has decayed from its peak value.

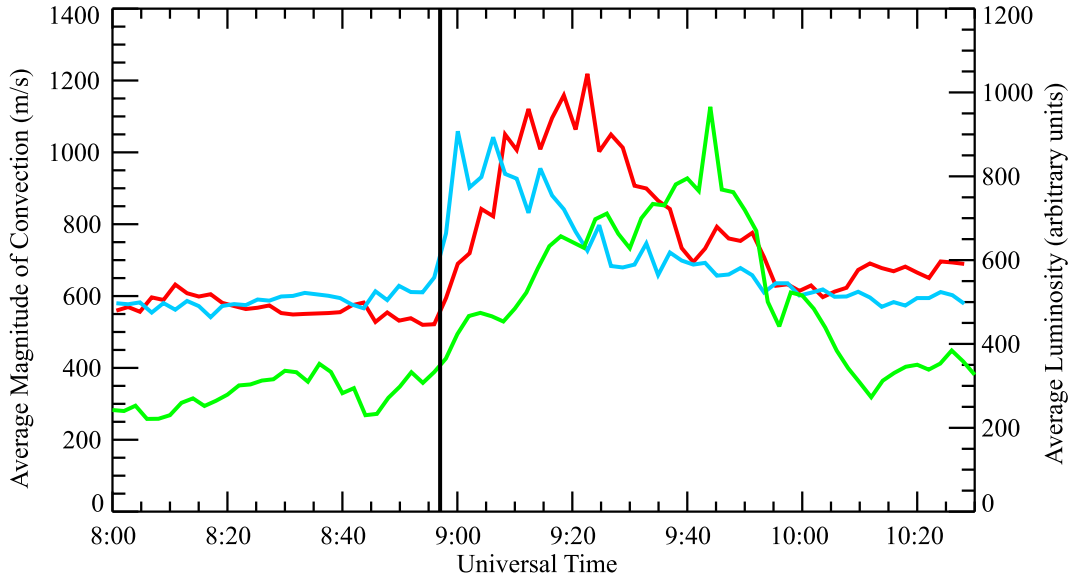

Figure 4.13: Luminosity and convection data for a December 05, 2001 substorm. IMAGE luminosity for high latitudes (red line) averaged across 19:00 to 23:00 MLT and 67^0 to 74^0 MLat and low latitudes (blue line) in the same MLT sector and 60^0 to 67^0 MLat. Convection velocity (green line) averaged across 19:00 to 23:00 MLT and 60^0 to 67^0 MLat. Vertical line indicates the substorm onset.

In addition to examining the relative activity of the SuperDARN l-o-s velocity and the luminosity measured by IMAGE, the relative location of their maximums should be examined. Figure 4.14 plots the location of the maximum SuperDARN convection velocity (vertical dashes) obtained from the standard global convection mapping software (*Ruohoniemi and Baker*, 1998) and maximum IMAGE luminosity (filled circles) in terms of MLT (Figure 4.14a) and MLat (Figure 4.14b) against UT from 08:00 to 10:30 UT. The area considered is the 19:00 to 24:00 MLT sector from 60^0 to 74^0 MLat. The vertical line indicates the substorm onset. Each velocity measurement has an error of 1/30 MLT and $1/30^0$ MLat and each luminosity measurement has an error of 1/12 MLT and $1/2^0$ MLat.

The maximum luminosity enhancement is located at ~22:30 MLT at the substorm onset, expands westward to a maximum location of 19:00 MLT at 09:25 UT, and finally returns eastward toward midnight, Figure 4.14a. Just after substorm onset the location of the velocity maximum jumps from 19:30 to 21:30 MLT and moves eastward with time. The maximum convection velocity occurs at 09:40 UT

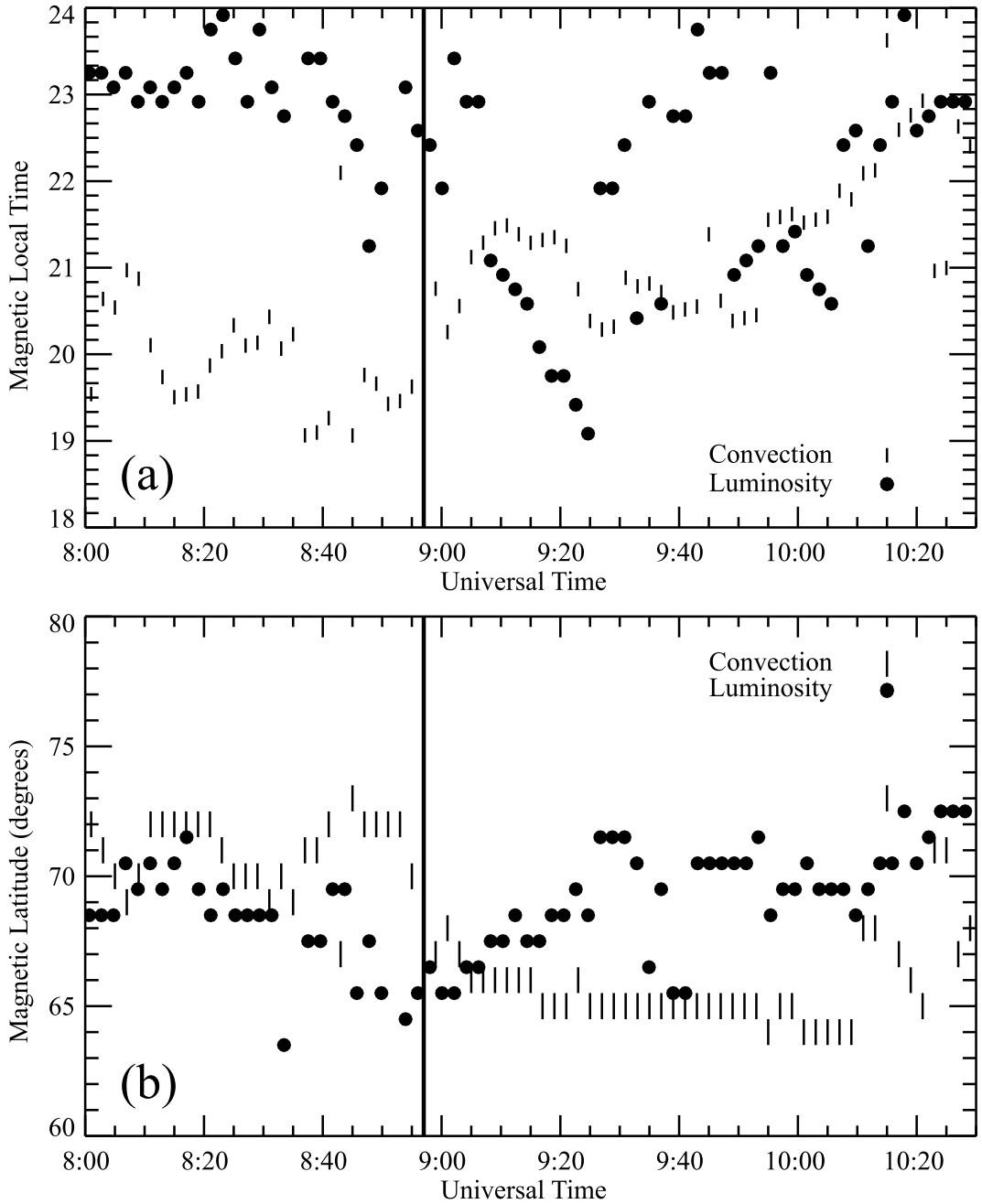

Figure 4.14: Location of the maximum luminosity measured by IMAGE and convection velocity according to SuperDARN from 19:00 to 24:00 MLT and 60^0 to 74^0 MLat in (a) MLT-UT and (b) MLat-UT coordinates. Filled circles denote luminosity data and vertical dashes denote velocity data. Vertical line indicates the substorm onset.

and 20:30 MLT. Now consider the latitudinal location of the convection and luminosity maximums plotted in Figure 4.14b. Prior to the substorm onset the convection maximums are located poleward of the luminosity maximums. About 20 minutes prior to the substorm onset, the luminosity maximum begins to shift equatorward from 69^0 to 66^0 MLat and then moves poleward from onset until 09:25 UT where it fluctuates between 72^0 and 68^0 MLat until 10:20 UT. At approximately 3 minutes prior to onset the location of the convection maximum drops equatorward to 65^0 MLat at 09:15 UT where it remains until 10:00 UT when it shifts to 64^0 MLat for 10 minutes. Essentially, the convection maximum moves equatorward and the luminosity maximum moves poleward after the substorm onset causing a separation in location of approximately 5^0 of magnetic latitude when the velocity peaks at 09:40 UT. It should be noted that the maximum westward and poleward expansions reached at 09:25 UT corresponds to the end of the recovery phase as identified by the Kaktovik magnetometer, Figure 4.11b.

(c) Comparison with DMSP measurements

We now present DMSP observations to confirm the location and magnitude of the high-velocity westward flows for comparison with the location of the equatorward edge of the auroral oval. Figure 4.15a maps the cross-track ion drifts measured by DMSP satellite F15 over the field of view of the King Salmon radar at approximately 09:18 UT. During this satellite pass, the radar and satellite make observations in approximately the same direction. According to the King Salmon radar there is a patch of westward flow of >1200 m/s spanning from 62^0 to 66^0 MLat located at a radar range of ∼1530 km. There is a more confined enhancement at about 1900 km. According to DMSP measurements, there is a region of enhanced velocities of >1000 m/s located from 64^0 to 67^0 MLat. Both the location and magnitude of the enhanced velocities agree between the DMSP and SuperDARN observations. The DMSP measurements indicate the enhancement is doubled peaked, but this cannot be confirmed in the radar observations, as there is significant spatial variation in the velocity, and a more elaborate analysis is required to detect the peaks.

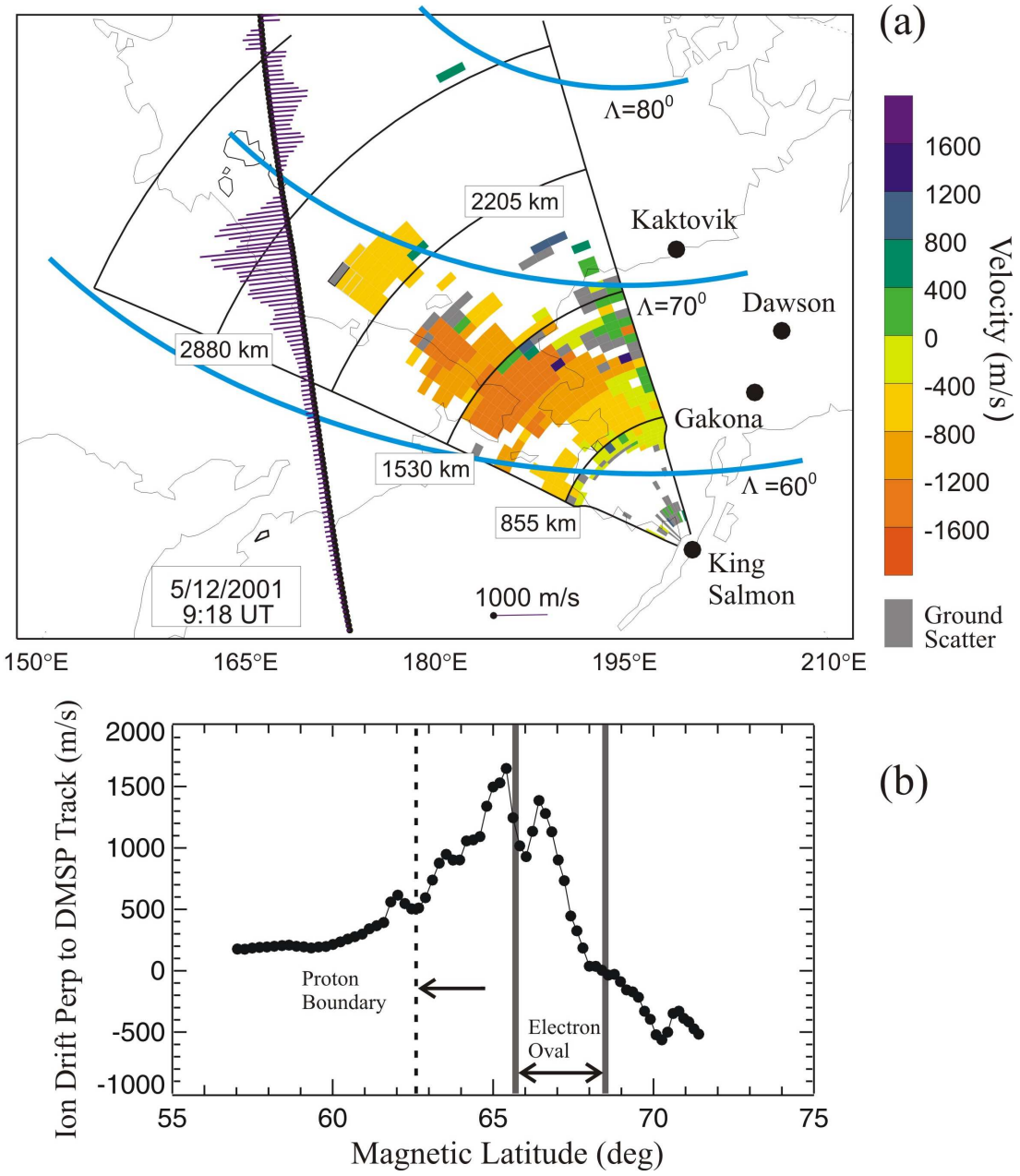

Figure 4.15: (a) King Salmon velocity map for December 5, 2001 at 09:18 UT with overlaid DMSP cross-track ion drifts for a DMSP F15 pass near the time of radar measurements. (b) A line plot of the ion drift data shown in panel (a) with the location of the auroral electron precipitation boundary (solid lines) and the equatorward boundary of the proton precipitation (dotted line) overplotted. DMSP particle data were considered for boundary identification.

Figure 4.15b graphs the DMSP cross-track ion drift against magnetic latitude. In addition, two solid vertical lines indicate the auroral oval location as identified by the electron precipitation detector onboard the satellite. A vertical dashed line indicates the equatorward edge of the proton precipitation. The DMSP velocity maximum is located slightly equatorward of the auroral oval boundary with an additional velocity peak located within the oval. Figure 4.15 indicates that the fast flows observed by the King Salmon radar are mostly outside the oval and can be classified as subauroral.

(d) Summary

Examination of the December 5, 2001 event shows that exceptionally fast flow streams can develop at the equatorward edge of the auroral oval. This happens when the luminosity in the equatorial portion of the auroral oval decreases during the recovery phase of a substorm as the region of strong precipitation shifts to the poleward edge of the auroral oval. The equatorward location of the velocity enhancements means the flows are very similar to SAPS, unlike the majority of the enhanced flows within the auroral oval presented for the December 15, 2001 event.

4.4.4 Other cases of SAPS-like flows

We have located several other events for which very high-velocity echoes were observed by the King Salmon radar in the duskside MLT sector and information on luminosity from IMAGE was available. A common feature of these events is that as the oval luminosity decays at the recovery phase of the substorm, a strong westward flow is established at the equatorward edge of the auroral oval in the area of weak precipitation (luminosity) and low ionospheric conductance. This was explicitly demonstrated for the December 5 and 15, 2001 events. The time delays between the substorm onset and the establishment of the strong westward flow varied between 20 and 50 minutes. It is important to note that the flows were not always channels extended over many hours of MLT; instead, they often appeared to be confined to the MLT sector in which the luminosity was decreased.

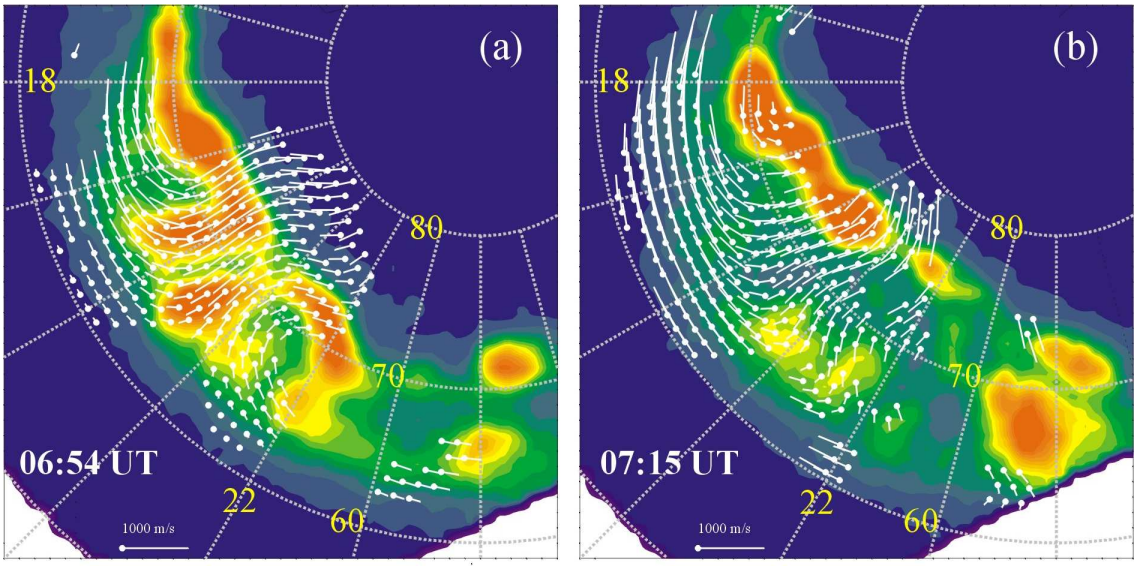

Figure 4.16: Auroral luminosity according to IMAGE observations and matched SuperDARN maps of plasma convection for a substorm on December 17, 2001 at (a) 06:54 UT, (b) 07:15 UT in the dusk sector. Red (blue) color corresponds to the strongest (weakest) luminosity.

On December 17, 2001 a fast flow was identified in beam 1 of the King Salmon radar at around 07:15 UT. The velocity began to enhance at the onset of a substorm identified by IMAGE at 06:24 UT, and began a more rapid increase ∼35 min later. Both the Kaktovik and Dawson magnetometers confirm the time of the substorm onset. According to the ACE IMF observations, the B_y component was relatively stable and positive, and the B_z component was fairly stable and mostly negative throughout the time interval. The Kp index for the event was 4-.

Figure 4.16 shows the duskside IMAGE luminosity and SuperDARN convection vectors for two different time frames. In Figure 4.16a, corresponding to 06:54 UT, IMAGE shows a clear double oval with streams of luminosity connecting the ovals. The convection velocities are comparable in both the meridional and azimuthal direction, with smaller velocities located in more equatorward locations. In the next frame, at 07:15 UT, Figure 4.16b, the luminosity has decayed in the equatorward portion of the auroral oval and the convection has responded by increasing, creating a stream of high-velocity flow equatorward of the intense auroral luminosity. There is a latitudinal separation of eight degrees between the maximum luminosity and the

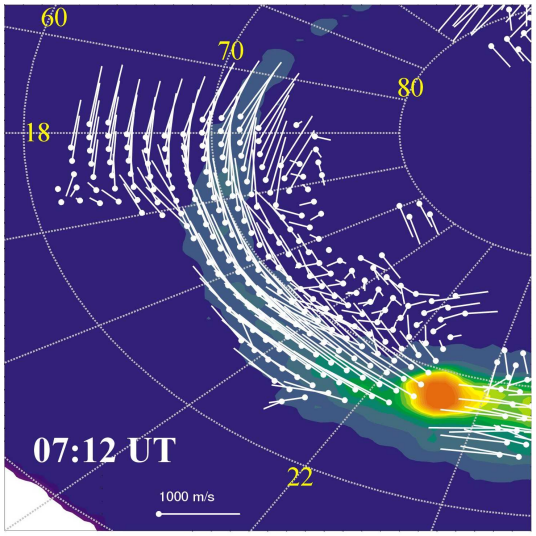

Figure 4.17: Auroral luminosity according to IMAGE observations and matched SuperDARN map of plasma convection at 07:12 UT. Red (blue) color corresponds to the strongest (weakest) luminosity.

maximum convection velocity. This is the largest separation observed in this thesis, which may be related to the relatively large Kp index observed.

On several occasions, the SuperDARN convection patterns were extended well equatorward of the auroral oval and we were able to observe the flow intensity in these areas. One such example is given in Figure 4.17 for December 1, 2001 at 07:12 UT. The substorm associated with this event had an onset at 06:39 UT, and the Kp index was 2- throughout the event. Here fast flow is seen in the dusk sector close to 18:00 MLT and extends well equatorward of the auroral oval. The magnitude of the flow outside the oval ranges from 600-800 m/s and is comparable to the flow within the oval. Unfortunately, vectors are not available for even lower latitudes, and it is impossible to investigate how the convection behaves equatorward of the radar's field of view.

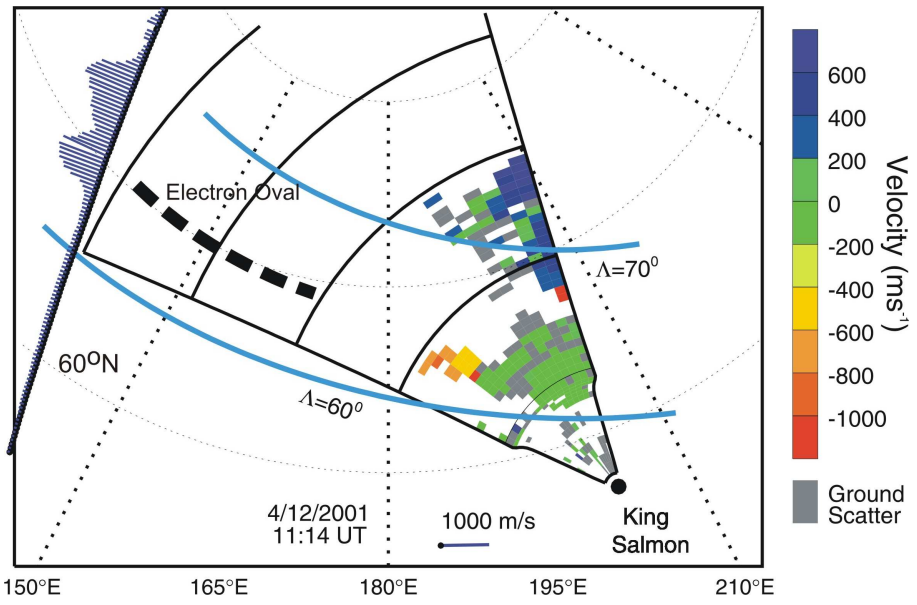

Figure 4.18: King Salmon velocity map for December 4, 2001 at 11:14 UT with overlaid DMSP cross-track ion drifts for a DMSP F15 pass near the time of radar measurements. Range labels are the same as in Figure 4.15.

4.4.5 Can the high-velocity King Salmon flow be "detached" from the auroral oval?

Previous studies using the Millstone Hill incoherent radar at mid-latitudes suggest strong flow channels exist completely separated from auroral oval flows. Each of the events discussed here show fast flows overlapping with, rather than detached from, the auroral oval. Attempts to locate detached flow streams with the King Salmon radar were unsuccessful. For many of the high-velocity events echoes were confined to the lowest numbered beams, possibly due to strong HF radio wave absorption in other beams, and it was not possible to identify latitudinal trends in the velocity. For example, consider Figure 4.18, which shows a DMSP F15 satellite pass over a map of the King Salmon l-o-s velocities on December 4, 2001 at 11:14 UT. DMSP indicates two peaks in the flow, one located within the auroral oval and another a few degrees less than the equatorward edge of the auroral oval. The King Salmon radar observes a localized velocity enhancement of >400 m/s in beams 3-6, compared to velocities of <200 m/s in the remainder of the observational area.

These echoes are located at the same magnetic latitudes as the equatorward fast flows observed by DMSP. Because there are no echoes immediately adjacent to this enhancement it is difficult to determine if King Salmon observes this flow as detached from, or equatorward of, the auroral oval. As this example shows, it is often difficult to determine the exact latitudinal characteristics of the King Salmon radar velocities because of data gaps.

Anderson et al. (2001) used limited examples from DMSP satellite measurements to suggest SAIDs overlap the equatorward edge of the auroral oval near midnight and become completely separated from the auroral oval at dusk. Observations shown in Figure 4.17 for December 1, 2001 seem to contradict this statement, as the duskside enhanced velocities are not strictly detached from the auroral oval. It is possible that faster flows exist equatorward of the detected flow outside of the SuperDARN field of view. However, this is not likely, considering the low magnetic activity indicated by a Kp index of 2- during the event. *Foster and Vo* (2002) only reported detached channel formation for magnetically active periods with Kp>5. For such conditions, observations of high-velocity SAPS-like flows are only expected equatorward of the King Salmon radar's field of view. Clearly, the recently built low-latitude SuperDARN radars will be in a better position to address this issue.

4.5 Discussion

According to the data presented, the King Salmon radar observes high-velocity echoes (>500 m/s) in its most equatorward and L-shell aligned beams. Such echoes are limited to the dusk sector from 18:00 to 23:00 MLT. The largest velocities occur near 21:00 MLT at 65^0 MLat. The maximum l-o-s velocities were observed in beam 1 and were of the order of 2 km/s (Figures 4.7 and 4.11). Determining the exact latitudinal width or longitudinal extent of the flow channels within the King Salmon observations is difficult due to the lack of echoes in some, and often most, beams. Estimates for the December 5 and 15, 2001 events suggest the flow channel spreads across $\sim 6^0$ MLat and 3 hours of MLT (Figures 4.8b and 4.12b). The temporal

duration of the fast flows, or the time during which the velocity was greater than its background value of 500 m/s ranges from 70 (December 5, 2001) to 90 (December 15, 2001) minutes (Figures 4.10 and 4.13).

4.5.1 Comparison with Millstone Hill observations of SAPS

The King Salmon observations are reminiscent of the SAPS flows determined from the Millstone Hill incoherent radar observations at low magnetic activity (Foster and Vo, 2002). High velocities are observed by both systems in the dusk sector. The Millstone Hill radar observes SAPS up to 50% of the time between 20:00-22:00 MLT and at Kp values of 2 to 4 (see Figure 8 in Foster and Vo, 2002), while detection of the high-velocity echoes by the King Salmon radar is very infrequent. We showed in Figure 4.2a that the echo occurrence rate for King Salmon is less than 20% in the dusk sector equatorward of 65^0 MLat (where SAPS detection is likely) for December 2001. Such a low occurrence rate makes SAPS detection more difficult, especially since the echo occurrence rates significantly decreased in subsequent years due to a general decay of solar activity (Figure 4.1). We counted the number of high-velocity events observed in beam 1 for the three months considered in Figure 4.2 and 4.3, as well as for June 2002, due to a reduced number of events in the summer. The threshold velocity was set to 450 m/s (similar to *Parkinson et al.* (2006)). We found that high-velocity events were observed in 46% (winter), 28% (equinox) and 26% (summer) of the days where echoes were detected in the SAPS-region.

We should mention that *Parkinson et al.* (2006) reported high-velocity echo occurrence rates of 40-50% using the Bruny Island radar. These authors considered data in beam 15, which has a flow angle of 50^0 (versus 10^0-20^0 for the low-latitude King Salmon beams). Bruny Island occurrence rates are in agreement with King Salmon statistics for winter. For equinox and summer, the King Salmon radar detects fewer high-velocity events than the Bruny Island radar.

The lower rate of fast flow detection at King Salmon as compared to the Millstone Hill observations likely originates from the difference in the radars' observational capabilities. The Millstone Hill radar provides velocity measurements most of

the time wherever its beam is pointed. In contrast, the King Salmon HF radar is very sensitive to the electron density distribution in the ionosphere and echoes may not always be detected even if irregularities and fast flows are present in the ionosphere. In addition, the King Salmon radar can only reliably observe azimuthal flows from 62^0-65^0 MLat in a very narrow range of MLT sectors, for individual scans. Equatorward portions of the ionosphere are often inaccessible for echo detection because of low electron density leading to insufficient radio wave refraction. For observations deeper into the oval, radio wave absorption is too strong for the echoes to be detected or strong E region density can over-refract radio waves and blanket echoes from the F region. This means that a significant portion of the high-latitude ionosphere is simply not accessible for HF measurements.

King Salmon and Millstone Hill observations agree on the location but not the magnitude of the velocity enhancements. At 21:00 MLT, the King Salmon radar measures enhancements of up to 638 m/s at $\sim 65^0$ MLat (see Figures 4.3a,b,c). The average Kp values for December 2001, March 2002, and July 2003 are 2-, 2-, and 3-. *Foster and Vo* (2002) reported velocities of <250 m/s at the same location for a stronger magnetic activity of Kp=6 (see their Figure 6). Higher velocities are observed at lower latitudes or at more westward locations. According to *Foster and Vo* (2002) the peak velocities are located at 62^0 MLat for Kp=4 at 21:00 MLT (their Figure 3). The trend of the diagram suggests that for Kp<4, the peak velocities would have a more poleward location. This also suggests that velocities >250 m/s would be observed at 65^0 MLat and 21:00 MLT for Kp<6. This means that the latitudinal location of the SAPS peak for Millstone Hill and the high-velocity observations at King Salmon agree. According to Figure 5 of *Foster and Vo* (2002), the magnitude of the peak SAPS velocity decreases with Kp. The peak velocity changes from >1050 m/s at Kp=6 to >450 m/s at Kp between 2 and 3. Although the velocity magnitudes reported by *Foster and Vo* (2002) only represent a lower bound to the peak velocity, this suggests that King Salmon velocities are larger than the SAPS velocities reported by *Foster and Vo* (2002).

The Millstone Hill and King Salmon velocities also differ with respect to the MLT sector in which their maximum is observed. For Kp=4 the peak Millstone Hill velocities are located at ∼16:00-18:00 MLT (see Figure 5 of *Foster and Vo* (2002)). In general, for all Kp the highest King Salmon velocities are located more eastward than the peak Millstone Hill velocities. For King Salmon, the maximum flow is observed centered at 21:00 MLT in the winter, 20:00 MLT at equinox, and 21:00 MLT in the summer with an additional enhancement from 16:00-17:00 MLT (see Figure 4.3a,b,c). The reason for this difference is unclear. Recall that in this study King Salmon measures l-o-s velocities roughly along the L-shells in the most equatorward beams. The velocities reported by *Foster and Vo* (2002) included observations at all Millstone Hill radar azimuths regardless of orientation, and the flow is assumed to be L-shell aligned. Such an assumption may affect the accuracy of the Millstone Hill velocity maximum for large flow angles. For example, *Ridley and Liemohn* (2002) predict a significant departure of up to 60^0 of SAPS flows from the L-shell directions at ∼18:00 MLT (see their Figure 6).

4.5.2 Relationship of high-velocity echoes detected by King Salmon with substorms

Each of the SAPS-like events identified by the King Salmon radar occurred during the recovery phase of a substorm. The strength of the substorms for the three events we presented in this thesis varied from Kp values of 2+ to 4-. The morphology and evolution of the substorm, as viewed by the IMAGE satellite was similar for the events studied. Prior to the substorm onset the auroral luminosity was quiet, with the exception of the pseudosubstorm on December 17, 2001. At substorm onset a bulge of enhanced luminosity appeared close to 22:00 MLT and 65^0 MLat. The luminosity quickly expanded both westward and poleward. Examination of both H-component magnetometer data and IMAGE luminosity plots indicate the substorm expansion phase lasted 15-25 minutes. In all cases, the poleward region of luminosity reached a strong peak after the equatorward region peaked. After maximum auroral

expansion was reached the luminosity faded, first in the most equatorward regions, until the pre-substorm luminosity was reached 50-90 minutes later.

In each event, the azimuthal flow in the King Salmon beams began to increase around the time of the substorm onset, when the auroral luminosity became enhanced. These flows may be similar to those observed by *Parkinson et al.* (2003, 2005, 2006). For the December 17, 2001 event the velocity enhancement was more obvious when the poleward portion of the luminosity strongly enhanced. During the expansion phase, the maximum luminosity moved poleward and the maximum convection velocity shifted equatorward and narrowed into a fast flowing westward stream located $4^0 - 8^0$ equatorward of the peak auroral luminosity. In each case the peak velocities occurred in subauroral regions during the recovery phase of the substorm after the equatorward luminosity had decayed.

Our results indicate the largest velocity enhancements occurred at a 20-50 minute delay from the substorm onset, which agrees with satellite observations by *Anderson et al.* (1993) who reported the detection of strong SAIDs about 30 minutes after the substorm onset. In this respect, an interesting result was published by *Provan et al.* (2004). These authors statistically studied the convection pattern evolution in the course of a substorm. By searching through their Figure 8, we discovered an enhancement of the azimuthal flow approximately 14 minutes after the substorm onset. Upon request, the first author of the study (G. Provan) performed a more detailed estimate of the time when the velocity was a maximum, as in their paper, only convection patterns at 4, 14, 20, and 28 minutes after onset were presented. It was found that maximum velocities are achieved 16 minutes after the substorm onset. Although the study by *Provan et al.* (2004) did not include data from the King Salmon radar, the delay time of fast flow formation from substorm onset is similar to the minimum delay of 10 min found in the King Salmon data.

4.5.3 On the possible mechanism for the formation of substorm related fast flows

On the basis of the data presented above we conclude that King Salmon high-velocity echoes occur according to two scenarios.

The first scenario involves a general convection enhancement in the course of a substorm. We observed that almost simultaneously with the substorm onset, convection was enhanced westward of the expanding auroral bulge. This was particularly noticeable in the December 15, 2001 event. The flow enhancement occurred in a broad region of the return convection flow at all latitudes of the auroral oval. The enhanced flows were observed at the equatorial edge of the oval as well. In principle, these can be identified as SAPS, though we believe that a more appropriate term for such flows would be AWFCs, as introduced by *Parkinson et al.* (2003). We think the flows these authors reported and our observations in both events are part of the substorm-related electrodynamics; it is not a surprise that these flows rise and decay in accord with general substorm enhancement and recovery. It is important to realize that the flow enhancement developed under conditions of positive B_z implying it should be associated with internal processes within the magnetosphere other than driven by the solar wind IMF conditions. *Koustov et al.* (2005b) presented more examples of similar enhancements of the return flow within the auroral oval during the active phase of a substorm.

We are not aware of other reports of this kind except in the paper by *Provan et al.* (2004) who presented convection measurements during a substorm but did not actually concentrate their attention on enhanced return flows in the duskside auroral region. Recently, somewhat similar observations were reported by *Bristow and Parris* (2006) who considered 10 isolated substorms and found average convection patterns using the superimposed epoch method. Their data agree with our first scenario, but the IMF conditions need to be analyzed.

The second scenario identified is the excitation of exceptionally fast flows at the equatorial edge of the auroral oval when precipitation shifts to the poleward edge

of the auroral oval leaving the equatorial portion free of significant precipitation. This happens during the later phase of a substorm with delays of 20-50 minutes from onset. Morphologically, this situation is similar to the one identified for SAPS as described by *Galperin* (2002) and reviewed in Section 1.7.2. For this reason we believe that these exceptionally fast flows at the equatorial edge of the auroral oval can be classified as SAPS.

This similarity can be even more obvious if one considers another aspect of the SAPS excitation morphology. *Anderson et al.* (1993) reported that during substorms the equatorward boundary of R2 currents in the dusk sector are located at the equatorward edge of ion precipitation. The R2 currents close with R1 currents located at the poleward boundary of the auroral oval via a poleward flowing Pedersen current. Conductivity is high in the auroral oval region due to electron precipitation and comparatively low in the subauroral region where only ions precipitate. Therefore, the R2 currents flow into a region of low conductivity and the poleward directed polarization electric field associated with the Pedersen current must be large for current continuity (*Anderson et al.*, 1993; *Foster and Burke*, 2002). This in turn drives fast flowing plasma streams westward. The dynamics of exceptionally fast flow development presented in this thesis support this scenario of fast flow formation.

In both scenarios one of the key questions to understand is the reason for a delay between the beginning of a substorm and the onset of high-velocity flows. *Galperin* (2002) insisted that it takes time for energetic protons and ions to propagate from the substorm breakup area to the dusk sector inner magnetosphere. Since substorms may have various locations in the tail, the time delay may vary. Although this explanation sounds reasonable, it does not fully explain our observations. The electrodynamics at the equatorial edge of the auroral oval are strongly dominated by substorm-related processes, and the polarization electric field effect due to energetic particle penetration into the inner magnetosphere and plasmasphere is not clearly isolated in our observations. It is only when the auroral precipitation, and therefore conductance, fades away, that we see the particle source of enhanced flows.

The physics of the conductance and the electric field changes within the fast flow region is complicated and has been discussed in a number of papers (e.g., *Schunk et al.*, 1975; *Banks and Yasuhara*, 1978; *Anderson et al.*, 1993; *Galperin*, 2002). Our observations are consistent with a notion that it is the combination of the substorm current system, particle penetration into the inner magnetosphere, auroral precipitation, and atmospheric chemistry that causes the formation of strong SAPS-like flows at the equatorial edge of the auroral oval in the duskside sector.

Chapter 5

Conclusions and suggestions for future research

This thesis covers two distinct areas of research. First, a comparison of SuperDARN line-of-sight velocities and then total convection velocities was performed against DMSP cross-track ion drifts to validate the quality of SuperDARN measurements. Second, the nature of high-velocity echoes in the King Salmon SuperDARN radar observations was investigated. The fast flows were identified as SAPS based on their characteristics, such as their subauroral location as determined by DMSP and IMAGE satellites. Next, the statistical characteristics of the echoes were studied. Two events of extremely fast flows were investigated in detail to determine the relationship of the observed flows with substorms.

5.1 Conclusions

Conclusions are made on each of the objectives of this thesis separately.

5.1.1 Comparison of SuperDARN line-of-sight velocities and convection vectors with DMSP cross-track ion drifts

1. SuperDARN line-of-sight velocities of F region echoes agree reasonably well with DMSP cross-track ion drifts. This conclusion is based on observations of 9 SuperDARN radars and 4 DMSP satellites for about 200 events. The slope of the best-fit line relating SuperDARN and DMSP velocities was m=0.84. There is a slight tendency for SuperDARN velocities to be less than DMSP ion drifts. This tendency

is less obvious for high velocity (>500 m/s) SuperDARN observations. Although there was some variation in results, each of the nine radars analyzed showed good agreement with DMSP observations. This result confirms the validity of merging the data from various SuperDARN radars (built on the same principle, but with some technical differences) into one database and producing global scale convection maps.

2. The quality of the agreement between SuperDARN and DMSP measurements seems to depend on the radar range of a comparison. Of the nine SuperDARN radars, Halley and Sanae velocities showed the worst agreement with DMSP satellite ion drifts. For these radars, the comparisons were performed for ranges of <1200 km. The splitting of the data for all radars into observations for ranges <1200 km and >1200 km showed that SuperDARN velocities had a tendency of being less than DMSP ion drifts at lower ranges. We suggest the observations at short ranges might be partially contaminated by E region scatter.

3. For a subset of events from the l-o-s comparison having almost ideal agreement, global convection maps were produced and the velocity vectors obtained were compared with DMSP observations. The agreement of the data deteriorated by ∼10% and, importantly, points of opposite polarity appeared in the data set. This result implies the SuperDARN post-processing technique introduces some errors in generating global convection maps. Caution should be practiced when small-scale processes are being studied with SuperDARN convection maps.

4. Reasonable overall agreement of SuperDARN F region velocities and DMSP ion drifts implies the data independently obtained by these instruments may be merged into a common database to produce joint convection maps. This conclusion is valid for a range of SuperDARN F region velocities up to 1500 m/s provided both instruments indicate smooth temporal and spatial variations. If the raw measurements show quick variations and strong spatial non-uniformity, merging of the SuperDARN and DMSP data may not be justifiable and additional analysis of the measurements and geophysical conditions is required.

5.1.2 Nature of dusk-side SAPS-like flows observed by the King Salmon radar

1. A statistical study of the King Salmon radar data revealed the regular detection of high-velocity (>500 m/s) flows oriented along the magnetic L-shells at 60^0-65^0 MLat in the 16:00-23:00 MLT sector. The largest velocities occurred for winter conditions near 21:00 MLT at 65^0 MLat. The velocity enhancements were the smallest for summer conditions. The enhanced flows were seen ∼30% of echo detection time at relatively low magnetic activity (Kp<4).

2. Observations from the Stokkseyri radar indicate velocity enhancements, but only in the auroral zone and at ∼15:00 MLT. These enhancements are of a smaller magnitude than those observed at King Salmon. The Stokkseyri radar field of view is $\sim 5^0$ poleward of the King Salmon radar observational area. Observations from the Unwin radar, which is a low latitude radar capable of viewing as far equatorward as $\sim 57^0$ MLat, also indicated velocity enhancements in the dusk sector at latitudes $< 65^0$ MLat. The strongest velocity echoes are observed at lower latitudes. This suggests the most equatorward radars in the SuperDARN network, King Salmon and Unwin, are very useful for studies of sub-auroral high-speed flows (SAPS).

3. For individual fast flow events, the line-of-sight velocity observed in the most equatorward beams of the King Salmon radar was as high as 2 km/s. The temporal duration of the fast flows ranged from 70 to 90 minutes, and the flows spread across up to $\sim 6^0$ MLat and up to 3 hours of MLT. The power and spectral widths of the high velocity echoes at the equatorward edge of the auroral oval were similar to the power and spectral widths of echoes at other latitudes even though the echo velocities were distinctly different.

4. Examination of SuperDARN convection maps indicates the velocity enhancements are regions of enhanced return flow in the two cell convection pattern in the evening sector and are not separate streams of flow.

5. For a number of the fast flow events identified, the maximum velocity coincided with the equatorward edge of the auroral oval as inferred from the DMSP

particle and IMAGE optical data. Exceptionally high velocities were observed in areas of low local electron precipitation.

6. A search to locate high-velocity channels detached from the auroral oval, similar to those observed at low latitudes by the Millstone Hill incoherent scatter radar, showed that although there were events for which the channel seemed to be equatorward of and detached from the auroral oval there were no observations as convincing as those presented for the Millstone Hill observations. Fast flow events were more commonly seen overlapping with the equatorward edge of the electron auroral oval.

7. For two events examined in detail, the velocity of the flow began to enhance during periods of positive B_z. This suggests the intensifications are not due to enhanced reconnection in the magnetotail.

8. The fastest flows observed by the King Salmon radar occurred approximately 20-50 minutes after onset, during the recovery phase of a substorm developing in the area of observations. The fastest velocities were located in the regions of low precipitation and therefore low conductivity, which were formed when the auroral luminosity decayed during the substorm recovery phase.

9. King Salmon high-velocity echoes occur according to two scenarios.

(a) The first scenario involves a convection enhancement that coincides with the onset of a substorm. The enhancement is located westward of the auroral bulge and spans across all auroral latitudes. During the substorm expansion phase the enhanced convection moves eastward and equatorward coherently with the respective expansion of auroral precipitations. Fast flows are also seen at the equatorial edge of the auroral oval. Although these flows can be classified as SAPS, they would be better classified as auroral westward flow channels (AWFCs) as they are located within and overlapping with the equatorward edge of the auroral oval.

(b) The second scenario involves the development of fast flows at the equatorial edge of the auroral oval during the substorm recovery phase when auroral precipitation shifts poleward, leaving regions of low conductivity in the low latitude auroral and subauroral regions. The equatorward location of the velocity enhancements

allows one to classify them as sub-auroral polarization streams (SAPS).

5.2 Suggestions for future research

Further work into each of the two objectives of this thesis would provide a more comprehensive study of each topic. Below we suggest potential areas for expansion.

5.2.1 Comparison of SuperDARN and DMSP observations

(a) Although we considered significant amounts of data for each of the nine radars, an exhaustive analysis is hardly complete. Even though we are confident in the conclusions of our line-of-sight comparison, a larger data set would better substantiate our conclusions. It would also be worthwhile to perform a more comprehensive comparison between SuperDARN convection maps and DMSP velocities. In this thesis we showed that processing SuperDARN l-o-s velocities into convection vectors introduces discrepancies between the raw data and the final convection velocities. It would be interesting to perform a comparative analysis by setting rigid criteria on the degree of agreement between the data sets, similar to a comparison between DMSP and AMIE observations performed by *Bekerat et al.* (2005). One can also try to include RPA data along the DMSP satellite trajectory to determine how well SuperDARN and DMSP observations compare.

(b) Our analysis indicates the data sets from both instruments are of reasonable quality; yet differences were still observed. It would be interesting to determine the reasons behind these discrepancies. Work in this direction has been started (*St-Maurice et al.*, 2006). In this respect, it is interesting to note that recent Wallops Island radar observations suggest this radar often detects F region echoes originating from the temperature-gradient instability. Waves generated by this instability may propagate at a velocity different from the $\mathbf{E}\times\mathbf{B}$ plasma drift.

(c) A more complete analysis should be made using radars whose field of view is crossed by DMSP satellites at multiple ranges (e.g., Kodiak). At far ranges, one would expect a comparison between SuperDARN and DMSP to be degraded due to the potential role of propagation conditions for HF radio waves. Although we did not notice this effect for Kodiak, our data set is limited, and a targeted investigation would be beneficial. One purpose of such a study would be to show that F region data could be contaminated by E region echoes through one and a half hop propagation.

(d) In the present analysis we discarded events indicating significant variability of the convection in the area of comparison. A more thorough investigation may allow one to determine the reason for velocity discrepancies.

5.2.2 King Salmon observations and possible expansion to other radars

(a) In the present study we identified large velocities in King Salmon radar data from October 2001 until July 2004. We did not examine individual events unless both IMAGE and DMSP data were available. Examining events where information on the auroral oval is not available may reveal additional information on the nature of high velocity flows.

(b) *Parkinson et al.* (2005) presented observations of high velocity echoes simultaneously observed in the Northern and Southern Hemispheres by the King Salmon and Bruny Island radars. Although the temporal variations in the velocities were comparable, the velocity magnitudes were somewhat different. These discrepancies may be partly explained by the fact that the radars are not perfectly conjugate. Fortunately, the newly built Unwin radar in the Southern Hemisphere is a better match to King Salmon. A comparative study between King Salmon and Unwin observations would be able to determine whether or not SAPS-like flows are conjugately located in the Northern and Southern Hemispheres.

(c) The plot of the averaged Unwin velocities for September 2005, Figure 4.4, indicates the presence of a velocity enhancement in the dusk sector as far equator-

ward as 59^0 MLat. Further investigation of SAPS-like flows with the Unwin radar would be beneficial. In this thesis we used observations from the IMAGE satellite to identify whether the observed velocity enhancements were at the equatorial edge of the auroral oval. In 2004-2005 (the last year of IMAGE operation), the satellite trajectory was more convenient for viewing activity in the Southern Hemisphere. There are numerous occasions of joint Unwin/IMAGE observations during high velocity events. A study should be performed determining the characteristics and number of high velocity events occurring in the Southern Hemisphere.

(d) The Unwin radar has been shown to occasionally detect fast flows that are detached from the auroral oval (*Makarevitch and Dyson*, 2006). We were not able to identify similar events with the King Salmon radar. An investigation into detached events would be beneficial in determining how the detached flow forms with respect to activity within the oval.

References

Akasofu, S.-I. (1964), The development of the auroral substorm, *Planet. Space Sci.*, *12*, 273–282.

Anderson, P. C., R. A. Heelis, and W. B. Hanson (1991), The ionospheric signatures of rapid subauroral ion drifts, *Geophys. Res. Lett.*, *96*(A4), 5785–5792.

Anderson, P. C., W. B. Hanson, R. A. Heelis, J. D. Craven, D. N. Baker, and L. A. Frank (1993), A proposed production model of rapid subauroral ion drifts and their relationship to substorm evolution, *J. Geophys. Res.*, *98*(A4), 6069–6078.

Anderson, P. C., D. L. Carpenter, K. Tsurude, T. Mukai, and F. J. Rich (2001), Multisatellite observations of rapid subauroral ion drifts (SAID), *J. Geophys. Res.*, *106*(A12), 29,585–29,599.

Baker, K. B., R. A. Greenwald, J. M. Ruohoniemi, J. R. Dudeney, M. Pinnock, P. T. Newell, M. E. Greenspan, and C.-I. Meng (1990), Simultaneous HF-radar and DMSP observations of the CUSP, *Geophys. Res. Lett.*, *17*(11), 1869–1872.

Banks, P. M., and F. Yasuhara (1978), Electric fields and conductivity in the nighttime E-region: A new magnetosphere-ionosphere-atmosphere coupling effect, *Geophys. Res. Lett.*, *5*(12), 1047–1050.

Baumjohann, W., and R. A. Treumann (1997), *Basic Space Plasma Physics*, Imperial College Press.

Bekerat, H. A., R. W. Schunk, L. Scherliess, and A. Ridley (2005), Comparison of satellite ion drift velocities with AMIE deduced convection patterns, *J. Atmos. Terr. Phys.*, *67*, 1463–1479.

Bristow, B., and T. Parris (2006), Substorm convection patterns observed by the SuperDARN, 2006 SuperDARN workshop, Chincoteague, USA.

Bristow, W. A., A. Otto, and D. Lummerzheim (2001), Substorm convection patterns observed by the super dual auroral radar network, *J. Geophys. Res.*, *106*(A11), 24,593–24,609.

Bristow, W. A., G. J. Sofko, H. C. Stenbaek-Nielsen, S. Wei, D. Lummerzheim, and A. Otto (2003), Detailed analysis of substorm observations using SuperDARN, UVI, ground-based magnetometers, and all-sky imagers, *J. Geophys. Res.*, *108*(A3), doi:10.1029/2002JA009242.

Burch, J. L. (2000), IMAGE mission overview, *Space Science Reviews*, *91*, 1–14.

Cravens, T. E. (1997), *Physics of Solar System Plasmas*, Cambridge University Press, New York.

Danskin, D. W. (2003), HF auroral backscatter from the E and F regions, Ph.D Thesis, University of Saskatchewan.

Davies, J. A., M. Lester, S. E. Milan, and T. K. Yeoman (1999), A comparison of velocity measurements from the CUTLASS Finland radar and the EISCAT UHF system, *Ann. Geophys.*, *17*(7), 892–902.

Davies, J. A., T. K. Yeoman, M. Lester, and S. E. Milan (2000), A comparison of F-region ion velocity observations from the EISCAT Svalbard and VHF radars with irregularity drift velocity measurements from the CUTLASS Finland HF radar, *Ann. Geophys.*, *18*(5), 589–594.

Drayton, R. A., A. V. Koustov, M. R. Hairston, and J.-P. Villain (2005), Comparison of DMSP cross-track ion drifts and SuperDARN line-of-sight velocities, *Ann. Geophys.*, *23*(7), 2479–2486.

Fejer, B. G., and M. C. Kelley (1980), Ionospheric irregularities, *Reviews of Geophysics*, *18*, 401–454.

Feldstein, Y., and G. V. Starkov (1967), Dynamics of auroral belt and polar geomagnetic disturbances, *Planet. Space Sci.*, *15*(2), 209–230.

Foster, J. C., and W. J. Burke (2002), SAPS: A new categorization for sub-auroral electric fields, *Eos AGU Transcripts*, *83*(36), 393–394.

Foster, J. C., and H. B. Vo (2002), Average characteristics and activity dependence of the subauroral polarization stream, *J. Geophys. Res.*, *107*(A12), 1475, doi: 10.1029/2002JA009409.

Galperin, Y. I. (2002), Polarization jet: characteristics and a model, *Ann. Geophys.*, *20*(3), 391–404.

Galperin, Y. I., V. N. Ponomarev, and A. G. Zosimova (1974), Plasma convection in polar ionosphere, *Ann. Geophys.*, *30*(1), 1–7.

Gonzalez, W. D., J. A. Joselyn, Y. Kamide, H. W. Kroehl, G. Rostoker, B. T. Tsurutani, and V. M. Vasyliunas (1994), What is a geomagnetic storm, *J. Geophys. Res.*, *99*(A4), 5771–5792.

Greenspan, M. E., P. B. Anderson, and J. M. Pelagatti (1986), Characteristics of the thermal plasma monitor (SSIES) for the Defense Meteorological Satellite Program (DMSP spacecraft S8 through F10), *Tech. Rep. AFGL-TR-86-0227*, Hanscom AFB, Mass.

Greenwald, R. A. (2004), New science with a mid-latitude SuperDARN radar, 2004 SuperDARN workshop, Saskatoon, Canada.

Greenwald, R. A., K. B. Baker, J. R. Dudeney, M. Pinnock, T. B. Jones, E. C. Thomas, J.-P. Villain, J.-C. Cerisier, C. Senior, C. Hanuise, R. D. Hunsuker, G. Sofko, J. Koehler, E. Nielsen, R. Pellinen, A. D. M. Walker, N. Sato, and H. Yamagishi (1995), DARN/SuperDARN: A global view of the dynamics of high-latitude convection, *Space Sci. Rev.*, *71*, 763–796.

Greenwald, R. A., K. Oksavik, R. J. Barnes, J. M. Ruohoniemi, J. B. H. Baker, and J. W. Gjerloev (2006), First anniversary evaluation of the performance of the Wallops SuperDARN radar, 2006 SuperDARN workshop, Chincoteague, USA.

Grocott, A., S. W. H. Cowley, J. B. Sigwarth, J. F. Watermann, and T. K. Yeoman (2002), Excitation of twin-vortex flow in the nightside high-latitude ionosphere during an isolated substorm, *Ann. Geophys.*, *20*(10), 1577–1601.

Guzdar, P. N., N. A. Gondarenko, and P. K. Chaturvedi (1998), Three-dimensional nonlinear simulation of the gradient drift instability in the high-latitude ionosphere, *Radio Science*, *33*, 1901–1913.

Hamza, A. M., M. Huber, W. Lyatsky, A. V. Kustov, D. André, and G. Sofko (2000), Eastward convection jet at the poleward boundary of the nightside auroral oval, *Geophys. Res. Lett.*, *27*(17), 2809–2812.

Hargreaves, J. K. (1992), *The Solar-Terrestrial Environment*, Cambridge University Press, Cambridge UK.

Heppner, J. P. (1977), Empirical models of the high-latitude electric fields, *J. Geophys. Res.*, *82*, 1115–1125.

Hosokawa, K., T. Iyemori, A. S. Yukimatu, and N. Sato (2001), Source of field-aligned irregularities in the subauroral F region as observed by the SuperDARN radars, *J. Geophys. Res.*, *106*(A11), 24,713–24,731.

Hsu, T.-S., and R. L. McPherron (2003), Occurrence frequencies of IMF triggered and nontriggered substorms, *J. Geophys. Res.*, *108*(A7), doi:10.1029/2002JA009442.

Hughes, J. M., and W. A. Bristow (2003), SuperDARN observations of the Harang discontinuity during steady magnetospheric convection, *J. Geophys. Res.*, *108*(A5), doi:10.1029/2002JA009681.

Iijima, T., and T. A. Potemra (1978), Large-scale characteristics of field-aligned currents associated with substorms, *J. Geophys. Res.*, *83*(A2), 599–615.

Jayachandran, P. T., E. F. Donovan, J. W. MacDougall, D. R. Moorcroft, J.-P. S. Maurice, and P. Prikryl (2002), SuperDARN E-region backscatter boundary in the dusk-midnight sector - tracer of equatorward boundary of the auroral oval, *Ann. Geophys.*, *20*(12), 1899–1904.

Jayachandran, P. T., J. W. MacDougall, E. F. Donovan, J. M. Ruohoniemi, K. Liou, D. R. Moorcroft, and J.-P. St-Maurice (2003), Substorm associated changes in the high-latitude ionospheric convection, *Geophys. Res. Lett.*, *30*(20), doi: 10.1029/2003GL017497.

Kamide, Y., and S. Kokubun (1996), Two-component auroral electrojet: Importance for substorm studies, *J. Geophys. Res.*, *101*(A6), 13,027–13,046.

Karlsson, T., G. T. Marklund, and L. G. Blomberg (1998), Subauroral electric fields observed by the Freja satellite: A statistical study, *J. Geophys. Res.*, *103*(A3), 4327–4341.

Kelley, M. C. (1989), *The Earth's Ionosphere: Plasma Physics and Electrodynamics*, Academic Press, San Diego California.

Kivelson, M. G., and C. T. Russell (1995), *Introduction to Space Physics*, Cambridge University Press, Cambridge UK.

Koustov, A. V., G. J. Sofko, D. André, D. W. Danskin, and L. V. Benkevitch (2004), Seasonal variation of HF radar F region echo occurrence in the midnight sector, *J. Geophys. Res.*, *109*(A6), doi:10.1029/2003JA010337.

Koustov, A. V., D. W. Danskin, R. A. Makarevitch, and J. D. Gorin (2005a), On the relationship between the velocity of E-region HF echoes and E×B plasma drift, *Ann. Geophys.*, *23*(2), 1–9.

Koustov, A. V., R. A. Drayton, K. A. McWilliams, and H. U. Frey (2005b), Restructuring of nightside convection during substorm, *Eos AGU Transcripts*, *86*(52), Fall Meet. Suppl. Abstract SM31A–0392.

Koustov, A. V., R. A. Drayton, R. A. Makarevich, K. A. McWilliams, J.-P. St-Maurice, T. Kikuchi, and H. U. Frey (2006), Observations of high-velocity SAPS-like flows with the King Salmon SuperDARN radar, *Ann. Geophys.*, *24*(6), 1591–1608.

Lacroix, P. J., and D. R. Moorcroft (2001), Ion acoustic HF radar echoes at high latitudes and far ranges, *J. Geophys. Res.*, *106*(A12), 29,091–29,103.

Lewis, R. V., M. P. Freeman, A. S. Rodger, G. D. Reeves, and D. K. Milling (1997), The electric field response to the growth phase and expansion phase onset of a small isolated substorm, *Ann. Geophys.*, *15*(3), 289–299.

Liang, J. (2004), Multi-instrument studies of ionospheric and magnetospheric processes, Ph.D Thesis, University of Saskatchewan.

Liang, J., G. J. Sofko, and E. F. Donovan (2004), On the spatial and temporal resolution between auroral intensification and flow enhancement in a pseudosubstorm event, *J. Geophys. Res.*, *109*(A6), doi:10.1029/2003JA010200.

Liang, J., G. J. Sofko, and H. U. Frey (2006), Postmidnight convection dynamics during substorm expansion phase, *J. Geophys. Res.*, *111*(A4), doi: 10.1029/2005JA011483.

Liou, K., and J. M. Ruohoniemi (2006), A case study of relationship between substorm expansion and global plasma convection, *Geophys. Res. Lett.*, *33*(2), doi: 10.1029/2005GL024736.

Lyons, L. R., S. Liu, J. M. Ruohoniemi, S. I. Solovyev, and J. C. Samson (2003), Observations of dayside convection reduction leading to substorm onset, *J. Geophys. Res.*, *108*(A3), 1119, doi:10.1029/2002JA009670.

Makarevitch, R. A., and P. L. Dyson (2006), Detached westward flow channels observed during moderately disturbed conditions (Kp=3), 2006 SuperDARN workshop, Chincoteague, USA.

Mende, S. B., H. Heetderks, H. U. Frey, M. Lampton, S. P. Geller, S. Habraken, E. Renotte, C. Jamar, P. Rochus, J. Spann, S. A. Fuselier, J.-C. Gerard, R. Gladstone, S. Murphree, and L. Cogger (2000), Far ultraviolet imaging from the IMAGE spacecraft. 1. System design, *Space Science Reviews*, *91*, 243–270.

Milan, S. E., T. K. Yeoman, M. Lester, E. C. Thomas, and T. B. Jones (1997), Initial backscatter occurrence statistics from the CUTLASS HF radars, *Ann. Geophys.*, *15*(6), 703–718.

Milan, S. E., J. A. Davies, and M. Lester (1999), Coherent HF radar backscatter characteristics associated with auroral forms identified by incoherent radar techniques: A comparison of CUTLASS and EISCAT observations, *J. Geophys. Res.*, *104*(A10), 22,591–22,064.

Morelli, J. P., R. J. Bunting, S. W. H. Cowley, C. J. Farrugia, M. P. Freeman, E. Friis-Christense, G. O. L. Jones, M. Lester, R. V. Lewis, H. Luhr, D. Orr, M. Pinnock, G. D. Reeves, P. J. S. Williams, and T. K. Yeoman (1995), Radar observations of auroral zone flows during the multiple-onset substorm, *Ann. Geophys.*, *13*, 1144–1163.

Nagle, R. K., E. B. Saff, and A. D. Snider (2000), *Fundamentals of differential equations and boundary value problems*, 3 ed., Addison Wesley Longman, Inc.

Nielsen, E., and K. Schlegel (1985), Coherent radar Doppler measurements and their relationship to the ionospheric electron drift velocity, *J. Geophys. Res.*, *90*, 3498–3504.

Parkinson, M. L., M. Pinnock, H. Ye, M. R. Hairston, J. C. Devlin, P. L. Dyson, R. J. Morris, and P. Ponomarenko (2003), On the lifetime and extent of an auroral westward flow channel (AWFC) observed during a magnetospheric substorm, *Ann. Geophys.*, *21*(4), 893–913.

Parkinson, M. L., M. Pinnock, J. A. Wild, M. Lester, T. K. Yeoman, S. E. Milan, H. Ye, J. C. Devlin, H. U. Frey, and T. Kikuchi (2005), Interhemispheric asymmetries in the occurrence of magnetically conjugate sub-auroral polarisation streams, *Ann. Geophys.*, *23*(4), 1371–1390.

Parkinson, M. L., P. L. Dyson, and M. Pinnock (2006), The importance of auroral westward flow channels in substorm evolution, *Advances in Space Research*, in press.

Provan, G., M. Lester, S. B. Mende, and S. E. Milan (2004), Statistical study of high-latitude plasma flow during magnetospheric substorms, *Ann. Geophys.*, *22*(10), 3607–3624.

Reiff, P. H., and J. L. Burch (1985), IMF B_y-dependent plasma flow and Birkeland currents in the dayside magnetosphere 2. A global model for northward and southward IMF, *J. Geophys. Res.*, *90*, 1595–1609.

Rich, F. J., and M. Hairston (1994), Large-scale convection patterns observed by DMSP, *J. Geophys. Res.*, *99*(A3), 3827–3844.

Ridley, A. J., and M. W. Liemohn (2002), A model-derived storm time asymmetric ring current driven electric field description, *J. Geophys. Res.*, *107*(A8), 1151, doi:10.1029/2001JA000051.

Ruohoniemi, J. M., and R. A. Greenwald (1996), Statistical patterns of high-latitude convection obtained from Goose Bay HF radar observations, *J. Geophys. Res.*, *101*, 21,743–21,763.

Ruohoniemi, J. M., and R. A. Greenwald (1997), Rates of scattering occurrence in routine HF radar observations during solar cycle maximum, *Radio Science*, *32*(3), 1051–1070.

Ruohoniemi, J. M., R. A. Greenwald, K. B. Baker, J.-P. Villain, and M. A. McCready (1987), Drift motions of small-scale irregularities in the high-latitude F region: An experimental comparison with plasma drift motions, *J. Geophys. Res.*, *92*, 4553–4564.

Ruohoniemi, J. M., R. A. Greenwald, J.-P. Villain, K. B. Baker, P. T. Newell, and C.-I. Meng (1988), Coherent HF radar backscatter from small-scale irregularities in the dusk sector of the subauroral ionosphere, *J. Geophys. Res.*, *93*(A11), 12,871–12,882.

Ruohoniemi, M., and K. B. Baker (1998), Large-scale imaging of high-latitude convection with Super Dual Auroral Radar Network HF radar observations, *J. Geophys. Res.*, *103*, 20,797–20,811.

Saka, O., T. Kitamura, H. Tachihara, M. Shinohara, N. B. Trivedi, N. Sato, J. M. Ruohoniemi, and R. A. Greenwald (2001), A substorm onset signature at the auroral zone as observed with SuperDARN and equatorial magnetometers, *J. Geophys. Res.*, *106*(A12), 29,037–29,050.

Schunk, R. W., W. J. Raitt, and P. M. Banks (1975), Effect of electric fields on the daytime high-latitude E and F regions, *J. Geophys. Res.*, *80*(22), 3121–3130.

Sofko, G. J., and A. Walker (2006), Electric field mapping in a dipole field - a tutorial overview, 2006 Annual SuperDARN workshop, Chincoteague, USA.

Spiro, R. W., R. A. Heelis, and W. B. Hanson (1979), Rapid subauroral ion drifts observed by Atmosphere Explorer C, *Geophys. Res. Lett.*, *6*(8), 657–660.

St-Maurice, J.-P., R. Drayton, R. Choudhary, A. Koustov, and S. Basal (2006), Comparing SuperDARN Doppler shifts with DMSP velocities under ideal situations: Is there a problem?, 2006 Annual SuperDARN workshop, Chincoteague, USA.

Stone, E. C., A. M. Frandsen, R. A. Mewaldt, E. R. Christian, D. Margolies, J. F. Ormes, and F. Snow (1998), The advanced composition explorer, *Space Science Reviews*, *86*, 1–22.

Taylor, J. R. (1997), *An introduction to error analysis: The study of uncertainties in physical measurements*, 2 ed., University Science Books.

Tsunoda, R. T. (1988), High latitude irregularities: A review and synthesis, *Rev. Geophys.*, *26*(N4), 719–760.

Villain, J.-P., G. Caudal, and C. Hanuise (1985), A SAFARI-EISCAT comparison of F region small-scale irregularities and the ion drift, *Ann. Geophys.*, *90*, 8433–8443.

Villain, J. P., R. A. Greenwald, K. B. Baker, and J. M. Ruohoniemi (1987), HF radar observations of E region plasma irregularities produced by oblique electron streaming, *J. Geophys. Res.*, *92*(A11), 12,327–12,342.

Villain, J.-P., R. André, M. Pinnock, R. A. Greenwald, and C. Hanuise (2002), A statistical study of the Doppler spectral width of high-latitude ionospheric F-region echoes recorded with SuperDARN coherent HF radars, *Ann. Geophys.*, *20*(11), 1769–1781.

Voronkov, I., E. Friedrich, and J. C. Samson (1999), Dynamics of the substorm growth phase as observed using CANOPUS and SuperDARN instruments, *J. Geophys. Res.*, *104*(A12), 28,491–28,504.

Walt, M. (1994), *Introduction to Geomagnetically Trapped Radiation*, Cambridge University Press.

Watanabe, M., M. Pinnock, A. S. Rodger, N. Sato, H. Yamagishi, A. S. Yukimatu, R. A. Greenwald, J.-P. Villain, and M. R. Hairston (1998), Localized activation of the distant tail neutral line just prior to substorm onsets, *J. Geophys. Res.*, *103*(A8), 17,651–17,669.

Xu, L. (2003), SuperDARN-derived plasma convection: comparison with other data and application to field-aligned current measurements, Ph.D. Thesis, University of Saskatchewan.

Xu, L., A. V. Koustov, J. Thayer, and M. A. McCready (2001), SuperDARN convection and Sondrestrom plasma drift, *Ann. Geophys.*, *19*(7), 749–759.

Yeh, H.-C., J. C. Foster, F. J. Rich, and W. Swider (1991), Storm time electric field penetration observed at mid-latitude, *J. Geophys. Res.*, *96*(A4), 5707–5721.

Yeoman, T. K., J. A. Davies, N. M. Wade, G. Provan, and S. E. Milan (2000), Combined CUTLASS, EISCAT and ESR observations of ionospheric plasma flows at the onset of an isolated substorm, *Ann. Geophys.*, *18*, 1073–1087.

Appendix A

Weighted least-squares fitting to a polynomial function

The constants relating two variables satisfying a polynomial relationship may be determined according to Taylor (1997). Consider a data set of N data points (x_i, y_i) with *i=1 . . N* where x and y satisfy the polynomial relationship given by *Taylor* (1997),

$$y = A + Bx + Cx^2 + \cdots + Hx^N. \tag{A.1}$$

Assume the uncertainty in x is negligible and the uncertainty in y varies with each data point and is given by σ_{y_i}.

A measured value y_i can be described by a Gaussian or normal distribution centered at its true value y_{t_i}, given by

$$y_{t_i} = A + Bx_i + Cx_i^2 + \cdots + Hx_i^N \tag{A.2}$$

(where $A, B, C, \cdots, H$ are unknown constants), with a width equal to it's uncertainty σ_{y_i}. The normal distribution function for a given point is simply

$$G_{y_{t_i},\sigma_{y_i}}(y_i) = \frac{1}{\sigma_{y_i}\sqrt{2\pi}} \cdot e^{\frac{-\left(y_i - y_{t_i}\right)^2}{2\sigma_{y_i}^2}}, \tag{A.3}$$

see Figure A.1. The probability of measuring the point y_i within a width σ_{y_i} about y_{t_i} is given by the Gaussian probability function

$$P_{y_{t_i},\sigma_{y_i}}(y_i) = \int_{y_{t_i}-\sigma_{y_i}}^{y_{t_i}+\sigma_{y_i}} G_{y_{t_i},\sigma_{y_i}}(y_i)\, dy_i = \int_{y_{t_i}-\sigma_{y_i}}^{y_{t_i}+\sigma_{y_i}} \frac{1}{\sigma_{y_i}\sqrt{2\pi}} \cdot e^{\frac{-\left(y_i - y_{t_i}\right)^2}{2\sigma_{y_i}^2}} dy_i. \tag{A.4}$$

The nature of the exponential function yields the following proportionality:

$$P_{y_{t_i},\sigma_{y_i}}(y_i) \propto \frac{1}{\sigma_{y_i}} e^{\frac{-\left(y_i - y_{t_i}\right)^2}{2\sigma_{y_i}^2}}. \tag{A.5}$$

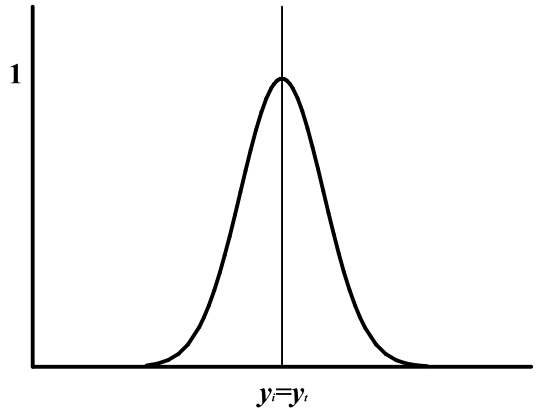

Figure A.1: Gaussian distribution function centered about $y_i = y_t$.

The probability $P(y)$ of measuring the entire data set of N points is then the product of the probabilities to measure each individual point:

$$\begin{aligned} P(y) &= P_{y_{t_1},\sigma_{y_1}}(y_1) \times \cdots \times P_{y_{t_N},\sigma_{y_N}}(y_N) \\ &\propto \frac{1}{\sigma_{y_1}} \cdot e^{\frac{-\left(y_1 - y_{t_1}\right)^2}{2\sigma_{y_1}^2}} \times \cdots \times \frac{1}{\sigma_{y_N}} \cdot e^{\frac{-\left(y_N - y_{t_N}\right)^2}{2\sigma_{y_N}^2}} \\ &= \frac{1}{\prod_i \sigma_{y_i}} \cdot exp\left(-\sum_i \frac{\left(y_i - y_{t_i}\right)^2}{2\sigma_{y_i}^2}\right) \\ &= \frac{1}{\prod_i \sigma_{y_i}} \cdot e^{\frac{\chi^2}{2}}, \end{aligned} \tag{A.6}$$

where proportionality (A.5) has been substituted and

$$\chi^2 = \sum_i \frac{\left(y_i - y_{t_i}\right)^2}{\sigma_{t_i}} = \sum_i \left(w_i \left(y_i - y_{t_i}\right)^2\right), \tag{A.7}$$

where use has been made of equation (A.9). To determine the best results for the unknown constants in equation (A.1) we will need to maximize the probability of obtaining the entire data set (x_i, y_i) equation (A.6), which means minimizing the term in the exponential, χ^2. This is done by differentiating equation (A.7) with respect to the unknown constants. The resulting equations are set to zero, and simultaneously solved for the unknown constants. For example, consider the first order polynomial function which indicates a linear relationship between the variables x, and y

$$y = A + Bx. \tag{A.8}$$

Define the weight w_i of a measurement i to be it's significance in determining the line of best fit based upon it's uncertainty

$$w_i = \frac{1}{\sigma_{y_i}^2}. \tag{A.9}$$

Equation (A.7) then becomes

$$\chi^2 = \sum_i w_i \left(y_i - A - Bx_i\right)^2, \tag{A.10}$$

which can be differentiated as follows:

$$\frac{\delta\chi^2}{\delta A} = -2\sum_i w_i \left(y_i - A - Bx_i\right) = 0, \tag{A.11}$$

$$\frac{\delta\chi^2}{\delta B} = -2\sum_i w_i x_i \left(y_i - A - Bx_i\right) = 0. \tag{A.12}$$

These two equations can be re-arranged to obtain

$$A\sum_i w_i + B\sum_i w_i x_i = \sum_i w_i y_i, \tag{A.13}$$

and

$$A\sum_i w_i x_i + B\sum_i w_i x_i^2 = \sum_i w_i x_i y_i. \tag{A.14}$$

Equations (A.13) and (A.14) can be simultaneously solved for the constants A and B:

$$A = \frac{\sum\limits_i w_i w_i^2 \sum\limits_i w_i y_i - \sum\limits_i w_i x_i \sum\limits_i w_i x_i y_i}{\sum\limits_i w_i \sum\limits_i w_i x_i^2 - \left(\sum\limits_i w_i x_i\right)^2}, \tag{A.15}$$

$$B = \frac{\sum\limits_i w_i \sum\limits_i w_i x_i y_i - \sum\limits_i w_i x_i \sum\limits_i w_i x_i \sum\limits_i w_i y_i}{\sum\limits_i w_i \sum\limits_i w_i x_i^2 - \left(\sum\limits_i w_i x_i\right)^2}. \tag{A.16}$$

The error in any of the constants in equation (A.1) can be determined using error propagation by solving the equation

$$\sigma_Z = \sqrt{\left(\frac{\delta Z}{\delta x}\sigma_x\right)^2 + \left(\frac{\delta Z}{\delta y}\sigma_y\right)^2}, \tag{A.17}$$

where Z represents the constant having error σ_Z

Let us again consider the first order polynomial in equation (A.8) and determine the errors in A and B. Because we are considering a system where σ_x is negligible, and σ_{y_i} varies for each data point, equation (A.17) can be re-written as

$$\sigma_Z = \sqrt{\sum_i \left(\frac{\delta Z}{\delta y}\sigma_y\right)^2}. \tag{A.18}$$

Substitution of (A.16) into (A.18) determines σ_B as follows:

$$\begin{aligned}\sigma_B &= \sqrt{\sum_i \left(\frac{\delta B}{\delta y_i}\sigma_{y_i}\right)^2} \\ &= \sqrt{\frac{\sum_i w_i}{\sum_i w_i \sum_i w_i x_i^2 - \left(\sum_i w_i x_i\right)^2}}.\end{aligned} \tag{A.19}$$

Note that $i = 1 \ldots N, j = 1 \ldots N$, and use has been made of equation (A.9). Similarly it can be shown that for the first order polynomial function that

$$\sigma_A = \sqrt{\frac{\sum_i w_i x_i^2}{\sum_i w_i \sum_i w_i x_i^2 - (\sum_i w_i x_i)^2}}. \tag{A.20}$$

Using the method of weighted averages helps to insure more significance is given to data points with a smaller uncertainty. A problem arises, as these equations are only valid if σ_{xi} is negligible. However, we can use equations (A.15), (A.16), and (A.9) if we replace σ_{xi} and σ_{yi} with equivalent values $\sigma_{xi\,eq}$ and $\sigma_{yi\,eq}$, where $\sigma_{xi\,eq} = 0$, and $\sigma_{yi\,eq}$ is a function of both σ_{xi} and σ_{yi}.

Consider a data point (x_i, y_i) with an associated error in the x-measurement, σ_{xi}, and a negligible uncertainty in the y-measurement, taken from a data set where x and y are linearly related. Let the best-fit line to the data set be given by $y = mx+b$, where m and b are non-zero constants, see Figure A.2. The point (x_i, y_i) will be offset from the line along the x-axis by an amount equal to σ_{xi}. However, any displacement in x is equal to a corresponding displacement in y (σ_{yi}). The slope ($m = dy/dx$) can be written as $m = \sigma_{yi}/\sigma_{xi}$. Therefore, if we have a data set with negligible uncertainty in y and a variable uncertainty in x, it can be replaced with a data set with negligible uncertainty in x and a variable equivalent uncertainty in y given by $\sigma_{yi} = m\sigma_{xi}$.

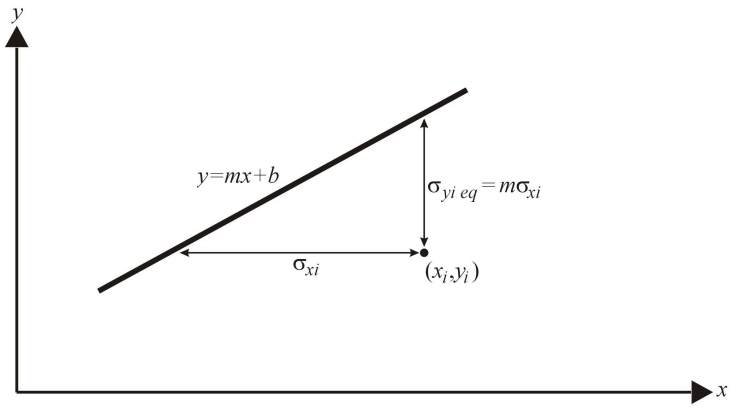

Figure A.2: For an observed point (x, y) deviating from a line $y = mx + b$, the deviation in the x-direction can be described by an equivalent deviation in the y-direction (*Taylor*, 1997).

This can be expanded to the more general case where there are variable uncertainties in both x and y. The uncertainties in x can be replaced by an equivalent uncertainty in y given by $m\sigma_{xi}$ and combined in quadrature with the uncertainties in y. The result is a data set with a negligible uncertainty in x and an equivalent uncertainty in y given by (*Taylor*, 1997)

$$\sigma_{yi\,eq} = \sqrt{\sigma_{yi}^2 + (m\sigma_{xi})^2}. \tag{A.21}$$

By using equation (A.21) in place of σ_{yi}, equation (A.9) may be re-written as

$$w_i = \frac{1}{\sigma_{yi}^2 + (B\sigma_{xi})^2}, \tag{A.22}$$

and substituted into equation (A.11) and (A.12) so that A and B may be solved numerically.